Applied Computational Electromagnetics Society

Journal

August 2012

Vol. 27 No. 8

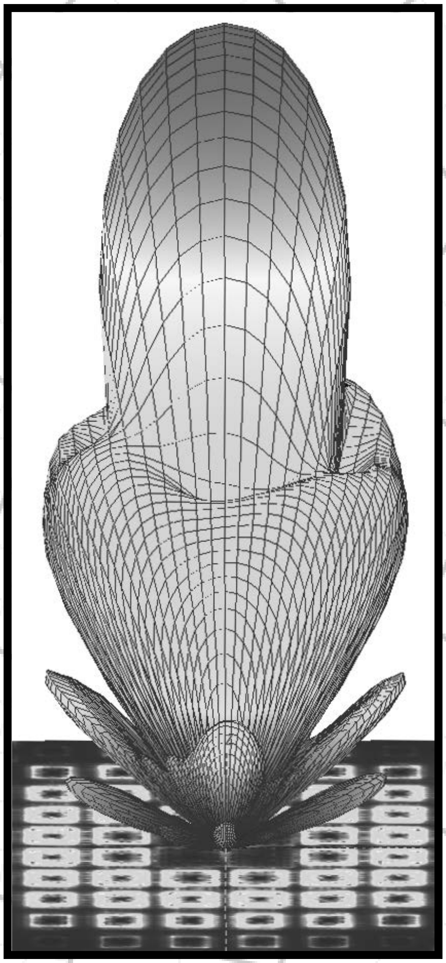

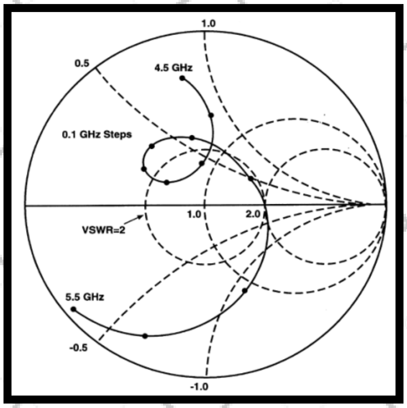

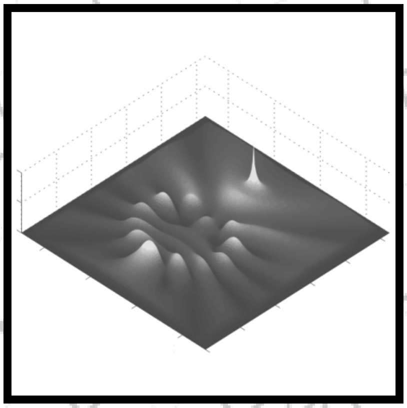

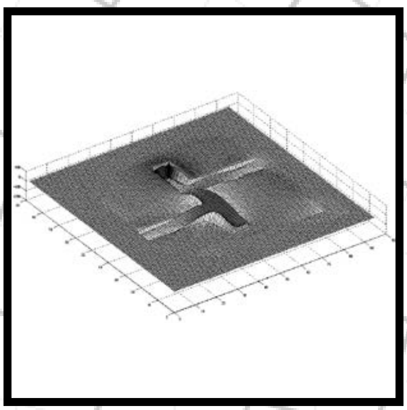

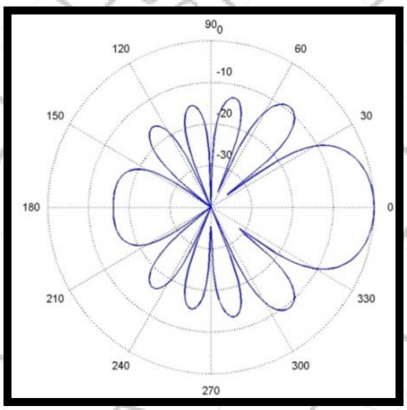

ISSN 1054-4887

GENERAL PURPOSE AND SCOPE: The Applied Computational Electromagnetics Society ***(ACES)*** Journal hereinafter known as the ***ACES Journal*** is devoted to the exchange of information in computational electromagnetics, to the advancement of the state-of-the art, and the promotion of related technical activities. The primary objective of the information exchange is to inform the scientific community on the developments of new computational electromagnetics tools and their use in electrical engineering, physics, or related areas. The technical activities promoted by this publication include code validation, performance analysis, and input/output standardization; code or technique optimization and error minimization; innovations in solution technique or in data input/output; identification of new applications for electromagnetics modeling codes and techniques; integration of computational electromagnetics techniques with new computer architectures; and correlation of computational parameters with physical mechanisms.

SUBMISSIONS: The ***ACES Journal*** welcomes original, previously unpublished papers, relating to applied computational electromagnetics. Typical papers will represent the computational electromagnetics aspects of research in electrical engineering, physics, or related disciplines. However, papers which represent research in applied computational electromagnetics itself are equally acceptable.

Manuscripts are to be submitted through the upload system of ***ACES*** web site http://aces.ee.olemiss.edu See "Information for Authors" on inside of back cover and at ***ACES*** web site. For additional information contact the Editor-in-Chief:

Dr. Atef Elsherbeni
Department of Electrical Engineering
The University of Mississippi
University, MS 386377 USA
Phone: 662-915-5382
Email: atef@olemiss.edu

SUBSCRIPTIONS: All members of the Applied Computational Electromagnetics Society are entitled to access and download the ***ACES Journal*** any published journal article available at http://aces.ee.olemiss.edu. Printed issues of the ***ACES Journal*** are delivered to institutional members. Each author of published papers receives a printed issue of the ***ACES Journal*** in which the paper is published.

Back issues, when available, are $50 each. Subscription to ***ACES*** is through the web site. Orders for back issues of the ***ACES Journal*** and change of address requests should be sent directly to ***ACES*** office at:

Department of Electrical Engineering
The University of Mississippi
University, MS 386377 USA
Phone: 662-915-7231
Email: aglisson@olemiss.edu

Allow four weeks advance notice for change of address. Claims for missing issues will not be honored because of insufficient notice, or address change, or loss in the mail unless the ***ACES*** office is notified within 60 days for USA and Canadian subscribers, or 90 days for subscribers in other countries, from the last day of the month of publication. For information regarding reprints of individual papers or other materials, see "Information for Authors".

APPLIED COMPUTATIONAL ELECTROMAGNETICS SOCIETY JOURNAL

August 2012
Vol. 27 No. 8
ISSN 1054-4887

The ACES Journal is abstracted in INSPEC, in Engineering Index, DTIC, Science Citation Index Expanded, the Research Alert, and to Current Contents/Engineering, Computing & Technology.

The illustrations on the front cover have been obtained from the research groups at the Department of Electrical Engineering, The University of Mississippi.

AUGUST 2012 REVIEWERS

Ahmed Abdelrahman
Manuel Arrebola
Adalbert Beyer
Jerdvisanop Chakarothai
Deb Chatterjee
Ming Chen
Ali Farahbakhsh
Mohammed Hadi
Mohammad Tariqul Islam
Dimitra Kaklamani
Rakhesh Kshetrimayum
David Lautru
Mun Soo Lee
Ricardo Matias
Antonino Musolino
Lionel Pichon
Lorena Lozano Plata
Hassan Ragheb
Behrooz Rezaeealam
Alain Reineix
Fernando Teixeira
Hossein Torkaman
Rui Wang
Joshua Wilson
Xiaoling Yang

THE APPLIED COMPUTATIONAL ELECTROMAGNETICS SOCIETY

JOURNAL

Vol. 27 No. 8 August 2012

TABLE OF CONTENTS

A Comparison of the Element Free Galerkin Method and the Meshless Local Petrov-Galerkin Method for Solving Electromagnetic Problems

Wei He [1], Zehui Liu [1], Richard K. Gordon[2], W. Elliott Hutchcraft[2], Fan Yang[1] and Afei Chang[3]

[1] School of Electrical Engineering
Chongqing University, Chongqing, 400044, China
hewei@cqu.edu.cn, lzhking2000@gmail.com, yangfancqu@gmail.com

[2] Department of Electrical Engineering
University of Mississippi, University, MS 38677, USA
eegordon@olemiss.edu, eeweh@olemiss.edu

[3]State Nuclear Electric Power Planning Design & Research Institute
Beijing, 100095, China
yafei0205@126.com

Abstract **─** In this paper, the element free Galerkin (EFG) method and the local Petrov-Galerkin (MLPG) method are compared for solving the electromagnetic problems. The EFG method and MLPG method are introduced at first. Both of the EFG and the MLPG methods are formulated in detail with Poisson's equation. Based on basic electromagnetic problems, the numerical results from the EFG method and MLPG method are given in this paper. The numerical results show that the EFG method and MLPG method both work well for the solution of electromagnetic problems. The EFG method, based on global weak form, needs background meshes for integration, and it needs more nodes to get an accurate result but it requires less cost in computational time. The MLPG method as a true meshless method doesn't needs any meshes in the implementation and can obtain an accurate result using fewer nodes than EFG. However, because the MLPG Method needs more integration nodes and has asymmetric matrices, it needs more CPU time than the EFG method with the condition that the same number of nodes is used in the problem domain.

Index Terms **─** electromagnetic problems, meshless method, the element free Galerkin method, the local Petrov-Galerkin method.

I. INTRODUCTION

With the development of the computational technologies, the modeling and simulation of engineering problems can be solved by the numerical methods. For decades, people have been using the finite-element method (FEM), boundary-element method (BEM) and finite-difference method (FDM) to solve the partial differential equation of the engineering systems [1]. Among those methods, the finite-element method is mostly widely used to solve the more-challenging problems as they require increasing demands on flexibility, effectiveness and accuracy for challenging problems with complex geometry [2]. However, the FEM requires the solution domain to be meshed, and the accuracy of the FEM depends on the quality of the mesh [1], and the mesh generation is more time consuming and a more expensive task than the solution of the finite element equations [3]. A lot of efforts have made to improve the design mesh, but it is still a challenge for some engineering analyses such as

Submitted On: Feb. 29, 2012
Accepted On: June 24, 2012

the dimensionally very small air gaps and the remaining electromagnetic structures.

To avoid these problems, recently a class of new methods called meshless or meshfree methods have been developed. The meshless methods do not require the generation of a mesh of the solution domain. The only necessary information are sets of nodes scattered in the solution domain as well as sets of nodes scattered on the boundaries, which means no mesh generation at the beginning of the calculation is needed.

There are many different types of meshless methods [4-8], some important examples of these methods include the smooth particle hydrodynamics (SPH) method, the diffuse-element method (DEM), the reproducing kernel particle method (RKPM), the element-free Galerkin (EFG) method, the meshless local Petrov-Galerkin (MLPG) method, the local boundary integral equation (LBIE) method, the hp-cloud method, the finite point method (FPM), and so on.

In those methods, the element free Galerkin (EFG) method (Belytschko et al., 1992) is one of the most viable methods and has become an inspiration source for the latter meshless methods. EFG method is based on the global weak-forms, so it requires background cells for evaluation of the integrals of the weak-forms. The meshless local Petrov-Galerkin (MLPG) method (Atluri and Zhu et al, 1998) is based on the local symmetric weak form (LSWF). The MLPG Method does not need elements or meshes either for interpolation purposes or for integration purposes. All integrals in the MLPG Method are carried out only on spheres (in 3-D or circles in 2-D) centered at each point in question [3,9,10]. Based on different type combinations of trial and test functions, there are six different schemes of the MLPG method [11].

Both the EFG method and the MLPG1 method are based on the moving least squares (MLS) approximation for the construction of the meshless shape functions. There are two differences between the EFG method and the MLPG method [12]. In the first place, the trial and test function in EFG are taken from the same functional spaces while they can be different for the MLPG method. Second, the main difference of them is the weak form used. The EFG method uses the global weak form and needs the background cells for the integration, but the MLPG method is based on the local symmetric weak form, so it does not need the background cells and thus is a truly meshless method.

In this paper, the EFG method and the MLPG method are formulated in detail and a comparison is made in their solution of an electromagnetic problem. The numerical results show that EFG method and MLPG method both work well for the electromagnetic problem. The EFG method needs more nodes to get an accurate result but has the advantage that the computation time is lower. The MLPG method doesn't need any background meshes in its implementation and can obtain an accurate result using fewer nodes than EFG, but the MLPG method requires more CPU time.

The following discussion begins with the brief description of the moving least squares (MLS) approximation which is used to construct the shape function for both the EFG method and the MLPG method in Section Ⅱ.The basic numerical implementation of EFG method and MLPG method are given in Section Ⅲ. The numerical examples are given in Section Ⅳ. The paper ends with conclusions and discussions in Section Ⅴ.

II.THE MOVING LEAST SQUARES APPROXIMATION

The MLS method was first introduced by Lancaster and Salkauskas [13]. The MLS has main two major features: (1) the approximated field function is continuous and smooth in the entire problem domain; (2) the MLS method can produce an approximation with the desired order of consistency [2]. Those two features make the MLS method the most widely used method for the construction of the meshless shape functions.

A. The MLS approximation scheme

Consider $u(x)$ to be the function of the field variable defined in the problem domain Ω. The approximation of $u(x)$ is denoted $u^h(\mathbf{x})$:

$$u^h(\mathbf{x}) = \sum_{j}^{m} p_j(\mathbf{x}) a_j(\mathbf{x}) \equiv \mathbf{p}^T(\mathbf{x})\mathbf{a}(\mathbf{x}), \quad (1)$$

where m is the number of terms of monomials (polynomial basis), and $\mathbf{a(x)}$ is a vector of coefficients given by

$$\mathbf{a}^T(x) = \{a_0(x)\ a_1(x)\ ...\ a_m(x)\}, \quad (2)$$

which are functions of x.

In equation (1), $\mathbf{p(x)}$ is a vector of complete monomial basis; m is the number of the terms in the basis. In this paper, the linear basis is used for 1D and 2D:

$$\mathbf{p}^T(\mathbf{x}) = [1 \;\; x], \quad in \;\; 1D, \tag{3}$$

$$\mathbf{p}^T(\mathbf{x}) = [1 \;\; x \;\; y], \quad in \;\; 2D. \tag{4}$$

The linear basis assures the MLS approximation has the linear completeness and can reproduce any smooth function and its first derivative with arbitrary accuracy [11]. The coefficients $a_j(\boldsymbol{x})$ can be obtained at the point $\mathbf{x}$ by minimizing a weighted discrete L_2 norm as follows:

$$J = \sum_{I=1}^{n} w(\mathbf{x}-\mathbf{x}_I)[\mathbf{p}^T(\mathbf{x}_I)\mathbf{a}(\mathbf{x}) - u_I]^2, \tag{5}$$

where n is the number of nodes in the neighborhood of $\mathbf{x}$ which weight function $w(\mathbf{x}-\mathbf{x}^I) \geq 0$. The u_I is the value of u at $\mathbf{x}=\mathbf{x}_I$. The neighborhood of $\mathbf{x}$ size is called the domain of influence of $\mathbf{x}$.

To obtain $\boldsymbol{a}(\boldsymbol{x})$ at an arbitrary point $\mathbf{x}$, the minimization condition is required:

$$\frac{\partial J}{\partial \mathbf{a}} = 0, \tag{6}$$

which leads to the following linear equation system:

$$\mathbf{A}(\mathbf{x})\mathbf{a}(\mathbf{x}) = \mathbf{B}(\mathbf{x})\mathbf{U}_s, \tag{7}$$

where the matrices $\mathbf{A}(\mathbf{x})$, $\mathbf{B}(\mathbf{x})$ and $\mathbf{U}_s$ are defined by

$$\mathbf{A}(\mathbf{x}) = \sum_{I}^{n} w(\mathbf{x}-\mathbf{x}_I)\mathbf{p}^T(\mathbf{x}_I)\mathbf{p}(\mathbf{x}_I), \tag{8}$$

$$\begin{aligned}\mathbf{B}(\mathbf{x}) = [&w_1(\mathbf{x}-\mathbf{x}_1)\mathbf{p}(\mathbf{x}_1), \;\; w_2(\mathbf{x}-\mathbf{x}_2)\mathbf{p}(\mathbf{x}_2), \ldots , \\ &w_n(\mathbf{x}-\mathbf{x}_n)\mathbf{p}(\mathbf{x}_n)],\end{aligned} \tag{9}$$

$$\mathbf{U}_s = [U_1, \;\; U_2, \ldots \;\; ,U_n]. \tag{10}$$

Solving the equation (7) for $\mathbf{a}(\mathbf{x})$ we obtain:

$$\mathbf{a}(\mathbf{x}) = \mathbf{A}^{-1}(\mathbf{x})\mathbf{B}(\mathbf{x})\mathbf{U}_s. \tag{11}$$

Hence, we have:

$$\begin{aligned}u^h(\mathbf{x}) &= \sum_{I}^{n}\sum_{j}^{m} p_j(\mathbf{x})(\mathbf{A}^{-1}(\mathbf{x})\mathbf{B}(\mathbf{x}))_{jI}u_I \\ &\equiv \sum_{I}^{n}\Phi_I(\mathbf{x})u_I,\end{aligned} \tag{12}$$

where the shape function is defined by:

$$\Phi_I(\mathbf{x}) = \sum_{j}^{m} p_j(\mathbf{x})(\mathbf{A}^{-1}(\mathbf{x})\mathbf{B}(\mathbf{x}))_{jI}. \tag{13}$$

The partial derivatives of $\Phi_I(\mathbf{x})$ can be obtained [3]:

$$\Phi_{I,i} = \sum_{j}^{m}\left\{p_{j,i}(\mathbf{A}^{-1}\mathbf{B})_{jI} + p_j(\mathbf{A}_{,i}{}^{-1}\mathbf{B} + \mathbf{A}^{-1}\mathbf{B}_{,i})_{jI}\right\}, \tag{14}$$

where: $\mathbf{A}_{,i}{}^{-1} = -\mathbf{A}^{-1}\mathbf{A}_{,i}\mathbf{A}^{-1}$ and $(\;\;)_{,i}$ denotes $\partial(\;\;)/\partial x^i$.

B. Choice of weight function

There are many types of weight functions that can be chosen [2]. The following weight function is adopted in this paper [14]:

$$w(\mathbf{x}-\mathbf{x}_I) \equiv w(r) = \begin{cases} \frac{2}{3} - 4r^2 + 4r^3 & for \;\; r \leq \frac{1}{2} \\ \frac{4}{3} - 4r + 4r^2 - \frac{4}{3}r^3 & for \;\; \frac{1}{2} < r \leq 1 \\ 0 & for \;\; r > 1 \end{cases}, \tag{15}$$

where $r = d_I / d_{mI}$, $d_I = \|\mathbf{x}-\mathbf{x}_I\|$ and d_{mI} is the size of the domain of influence of the I^{th} node.

III. IMPLEMENTATION OF THE EFG METHOD AND THE MLPG METHOD

In this section, a basic domain obeying Poisson's equation function and boundary conditions is considered to demonstrate the formulation of the EFG method and the MLPG method. The governing equation and boundary conditions are expressed as:

$$\nabla^2 u(\mathbf{x}) = -\frac{\rho(\mathbf{x})}{\varepsilon} \quad \mathbf{x} \in \Omega. \tag{16}$$

The essential and the natural boundary conditions are respectively given by:

$$u(\mathbf{x}) = u_0 \quad on \;\; \Gamma_u, \tag{17a}$$

$$\frac{\partial u(\mathbf{x})}{\partial \mathbf{n}} \equiv q = \bar{q} \quad on \;\; \Gamma_q, \tag{17b}$$

where the domain is enclosed by $\partial\Omega = \Gamma_u \cup \Gamma_q$ and $\mathbf{n}$ is the outward normal direction to the boundary.

A. The EFG method formulation

The EFG method is based on the globe weak form on the global problem domain Ω and the essential boundary conditions can be imposed by the penalty method by penalty parameter. The equivalent weak form of Poisson's function is:

$$\int_{\Omega}\left(\nabla^2 u + \frac{\rho(\mathbf{x})}{\varepsilon}\right)v d\Omega - \alpha\int_{\Gamma_u}(u-u_0)v d\Gamma = 0, \tag{18}$$

where u is the trial function approximated by the MLS method, v is the test function, and $\alpha >> 1$ is a penalty parameter used to impose the essential boundary conditions.

Using the formula $(\nabla^2 u)v = u_{,ii}v = (u_{,i}v)_{,i} - u_{,i}v_{,i}$, the divergence theorem and $u_{,i}ni = \partial u / \partial n \equiv q$, we can derive the local weak form as:

$$\int_{\Omega}\left(\nabla v \cdot \nabla u - \frac{\rho(\mathbf{x})}{\varepsilon}v\right)d\Omega - \int_{\partial\Omega} qvd\Gamma + \alpha\int_{\Gamma_u}(u-u_0)vd\Gamma = 0. \tag{19}$$

Imposing the natural boundary (17b), we can obtain:

$$\int_{\Omega}(\nabla v \cdot \nabla u)d\Omega + \alpha\int_{\Gamma_u} uvd\Gamma - \int_{\Gamma_u} qvd\Gamma = \int_{\Gamma_q} \bar{q}vd\Gamma + \alpha\int_{\Gamma_u} u_0 vd\Gamma + \int_{\Omega}\frac{\rho(\mathbf{x})}{\varepsilon}vd\Omega. \tag{20}$$

When the trial functions and test functions are taken from the same function space and produced by Eq. (12) [3], we can discretize Eq. (20) as:

$$\mathbf{Ku} = \mathbf{f}, \tag{21}$$

where the matrix $\mathbf{K}$ and the vector $\mathbf{f}$ are define by:

$$K_{ij} = \int_{\Omega}\nabla\Phi_i \cdot \nabla\Phi_j d\Omega + \alpha\int_{\Gamma_u}\Phi_i\Phi_j d\Gamma - \int_{\Gamma_u}\Phi_i\frac{\partial\Phi_j}{\partial\mathbf{n}}d\Gamma. \tag{22}$$

$$f_i = \int_{\Gamma_q}\bar{q}\Phi_i d\Gamma + \alpha\int_{\Gamma_u}\bar{u}\Phi_i d\Gamma + \int_{\Omega_s}\frac{\rho(\mathbf{x})}{\varepsilon}\Phi_i d\Omega. \tag{23}$$

B. The MLPG method formulation

The MLPG method is based on the local symmetric weak form over a local sub-domain Ω_s, the local sub-domain Ω_s is entirely inside the global problem domain Ω. A local weak form of the governing equation (16) and the boundary conditions (17) can be written as:

$$\int_{\Omega_s}\left(\nabla^2 u + \frac{\rho(\mathbf{x})}{\varepsilon}\right)vd\Omega - \alpha\int_{\Gamma_{su}}(u-u_0)vd\Gamma = 0, \tag{24}$$

where u, v and $\alpha >> 1$ are the trial functions, test functions and penalty parameter respectively. Γ_{su} is a part of the essential boundary Γ_u. If the sub-domain has no intersection with the global essential boundary Γ_u, the second part of equation (24) vanishes [11].

Corresponding to the EFG formulation, the local weak form can be written as:

$$\int_{\Omega_s}\left(\nabla v \cdot \nabla u - \frac{\rho(\mathbf{x})}{\varepsilon}v\right)d\Omega - \int_{\partial\Omega_s} qvd\Gamma + \alpha\int_{\Gamma_{su}}(u-u_0)vd\Gamma = 0. \tag{25}$$

Using the natural boundary condition (17b) we can obtain:

$$\int_{\Omega_s}\left(\nabla v \cdot \nabla u - \frac{\rho(\mathbf{x})}{\varepsilon}\right)vd\Omega - \int_{L_s} qvd\Gamma - \int_{\Gamma_{su}} qvd\Gamma - \int_{\Gamma_{sq}}\bar{q}vd\Gamma + \alpha\int_{\Gamma_{su}}(u-u_0)vd\Gamma = 0. \tag{26}$$

where Γ_{sq} is a part of the natural boundary of Γ_q, if a sub-domain is totally inside the globe domain and has no intersection between Ω_s, the $L_s = \partial\Omega_s$ and the integrals over Γ_{su} and Γ_{sq} vanish [11].

The weight function used in the MLS approximation is chosen as the test function in the MLPG method. So the test function will vanish on the boundary of the local domain Ω_s and the boundary L_s. Using this function, the function (26) can be rewritten as:

$$\int_{\Omega_s}\nabla w_s \cdot \nabla u d\Omega + \alpha\int_{\Gamma_{su}} w_s u d\Gamma - \int_{\Gamma_{su}} w_s q d\Gamma = \int_{\Gamma_{sq}} w_s\bar{q}d\Gamma + \alpha\int_{\Gamma_{su}} w_s\bar{u}d\Gamma + \int_{\Omega_s} w_s\frac{\rho(\mathbf{x})}{\varepsilon}d\Omega. \tag{27}$$

To obtain the discrete equations, substitution of (12) into (27), we can discretize Eq. (27) as:

$$\mathbf{Ku} = \mathbf{f}, \tag{28}$$

where

$$K_{ij} = \int_{\Omega_s}\nabla w_s \cdot \nabla\Phi_j d\Omega + \alpha\int_{\Gamma_{su}} w_s\Phi_j d\Gamma - \int_{\Gamma_{su}} w_s\frac{\partial\Phi_j}{\partial\mathbf{n}}d\Gamma, \tag{29a}$$

and

$$f_i = \int_{\Gamma_{sq}} w_s\bar{q}d\Gamma + \alpha\int_{\Gamma_{su}} w_s\bar{u}d\Gamma + \int_{\Omega_s} w_s\frac{\rho(\mathbf{x})}{\varepsilon}d\Omega. \tag{29b}$$

IV. NUMERICAL EXPERIMENTS

In this paper, the essential boundary conditions in the EFG and MLPG methods are both imposed by the penalty method with the penalty parameter α being chosen as 10^6 [2,12]. The number of integration points is chosen to be three times the total number of nodes in EFG, the local quadrature domain Ω_s with four subdivision cells and 4×4 integration points in each cell is used in the local quadrature domain in MLPG method [3].

In order to investigate the accuracy of the EFG and MLPG methods, a relative error is calculated as follows [12]:

$$Error = \frac{\max_{1\le i\le N}\left\| u_i^{num} - u_i^{ana}\right\|}{\max_{1\le i\le N} u_i^{ana}}, \quad (30)$$

where u_i^{num} denotes the numerical solution of the ith node and the u_i^{ana} denotes the analytic solution of the ith node.

A. Solution of Poisson's equation

We first consider Poisson's equation with the problem domain illustrated in Fig. 1. As shown in Fig. 1, the size of the problem domain is $\Omega \equiv (0,10)\times(0,10)$ with dielectric constant ε_0. The governing equation and boundary condition are as follows:

$$\nabla^2 u(\mathbf{x}) = -\pi^2\left(\frac{1}{a_1^{\,2}}+\frac{1}{a_2^{\,2}}\right)\sin\left(\frac{y}{a_1}\pi\right)\cos\left(\frac{x}{a_2}\pi\right)\frac{\rho_0}{\varepsilon_0}, \quad (31)$$

$$u(\mathbf{x}) = 0 \quad on \ \Gamma_u, \quad (32a)$$

$$\frac{\partial u(\mathbf{x})}{\partial \mathbf{n}} = 0 \quad on \ \Gamma_q. \quad (32b)$$

where ρ_0 is the distribution density, $\rho_0 = -100C/m^2$, ε_0 is dielectric constant and two choices of a_1 and a_2 have been made such that $a_1, a_2 \in \{1, 2, 5, 10\}$.

With different a_1 and a_2 the analytic solution is different. The analytic solution of this problem is:

$$u(\mathbf{x}) = \sin\left(\frac{y}{a_1}\pi\right)\cos\left(\frac{x}{a_2}\pi\right)\frac{\rho_0}{\varepsilon_0}. \quad (33)$$

The Analytical solution based on equation (33) is shown in Figs. 2 and 3 for different values of a_1 and a_2. A comparison of the exact solution with numerical results from both EFG and MLPG methods along the line x=5 is shown in Fig. 4 and Fig. 5. The total number of nodes was 400 for Fig. 4 and 2500 nodes for Fig. 5. Each Fig shows the results for the two different values of a_1 and a_2.

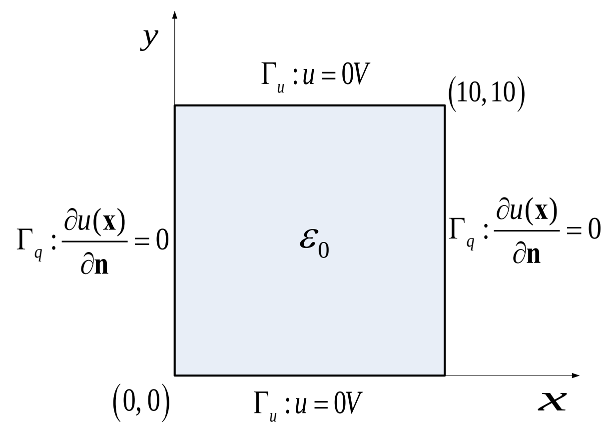

Fig. 1. Problem domain for Poisson's equation.

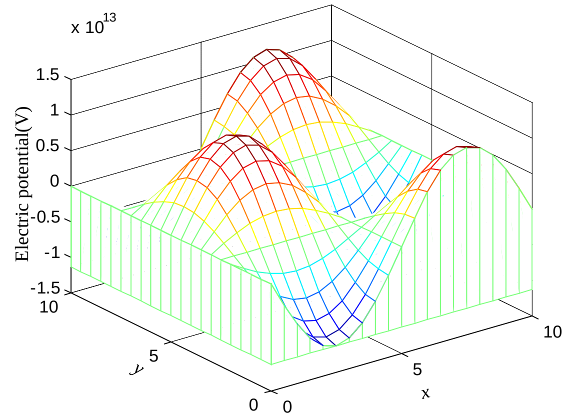

Fig. 2. The analytic solution of the Poisson's problem with a_1=5 and a_2=5.

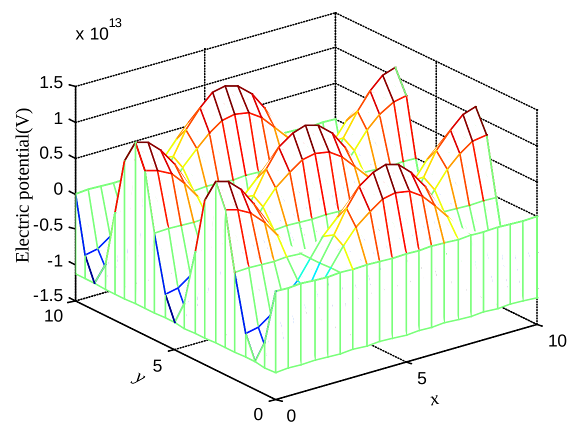

Fig. 3. The analytic solution of the Poisson's problem with a_1=2 and a_2=5.

We can observe good agreement between analytical and numerical results from Fig. 4 and Fig. 5. And the numerical results become more accurate as more nodes are used in the calculation.

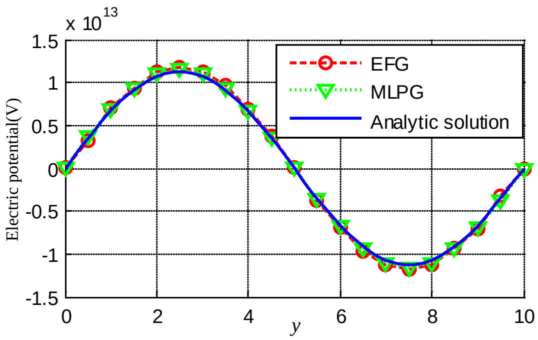

(a) a_1=5 and a_2=5.

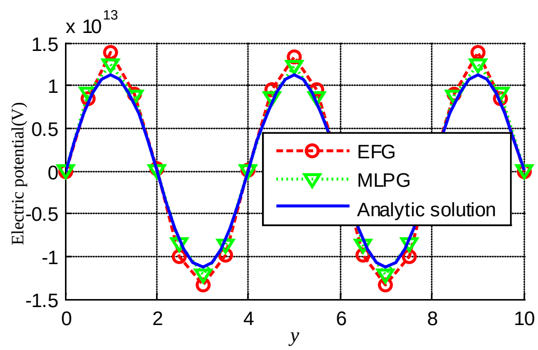

(b) a_1=2 and a_2=5.

Fig. 4. Comparison between the analytic solution, EFG method and MLPG method with 400 nodes along x=5 .

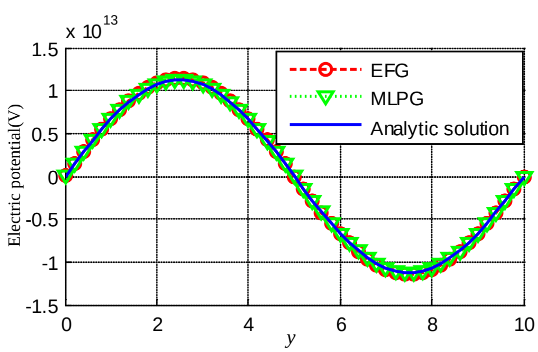

(a) a_1=5 and a_2=5.

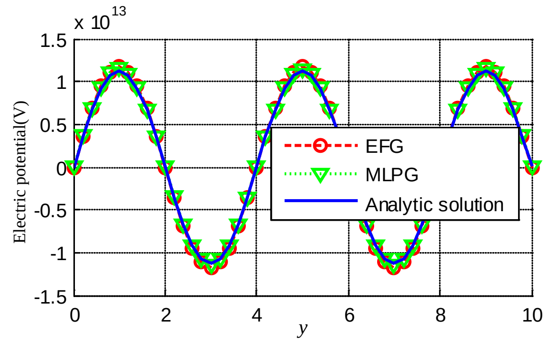

(b) a_1=2and a_2=5.

Fig. 5. Comparison between the analytic solution, EFG and MLPG method with 2500 nodes used along x=5.

B. Solution of Helmholtz equation

Next, let us consider a problem domain which is governed by the Helmholtz equation [8]:

$$\nabla^2 E_z + k^2 E_z = 0 \quad for\ (x,y) \in \Omega, \tag{34}$$

$$E_z(x,y) = f(x,y) \quad for\ (x,y) \in \partial\Omega. \tag{35}$$

The problem domain along with the associated boundary conditions is illustrated in Fig. 6.

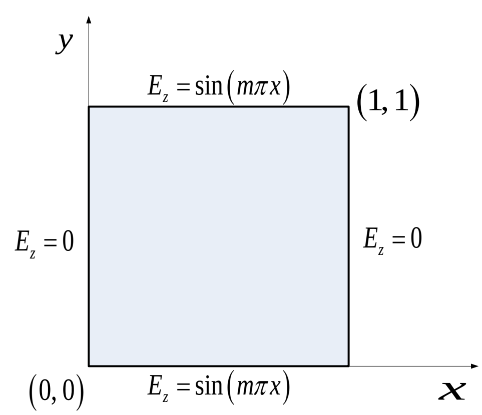

Fig. 6. Example of Helmholtz equation.

Consider the case for which $\lambda = \frac{2\pi}{k} = 1$. The analytic solutions of this problem with two different choices of m in boundary conditions are shown in Figs. 7 and 8.

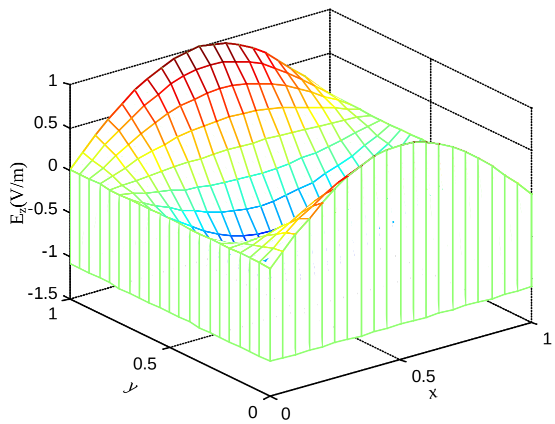

Fig. 7. The analytic solution of the Helmholtz equation with m=1.

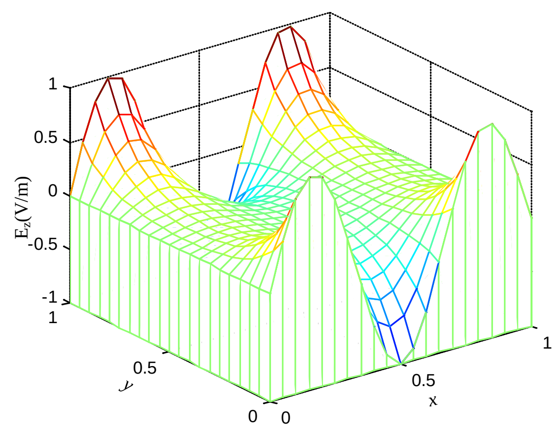

Fig. 8. The analytic solution of the Helmholtz equation with m=3.

A comparison of the exact solution with numerical results from both EFG and MLPG methods along the line y=0.5 is shown in Fig. 9 and Fig. 10. The total number of nodes was 400 for Fig. 9 and 2500 nodes for Fig. 10.

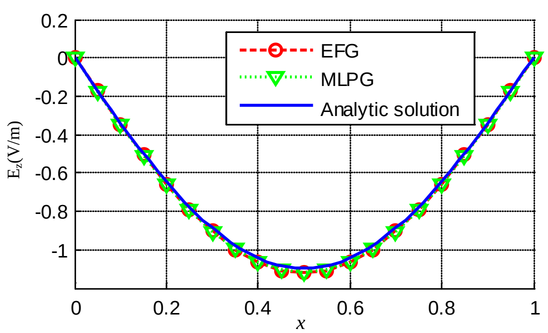

(a) The analytic and numerical solutions with m=1.

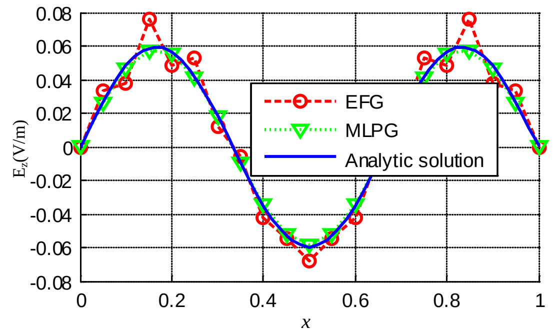

(b) The analytic and numerical solutions with m=3.

Fig. 9. Comparison between the analytic solution, EFG method and MLPG method with 400 nodes along y=0.5.

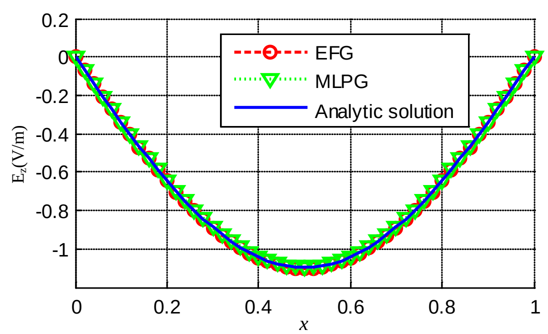

(a) The analytic and numerical solutions with m=1.

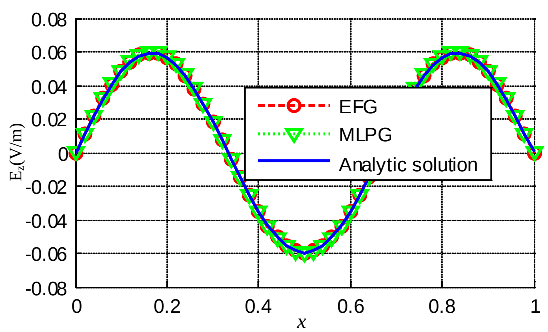

(b) The analytic and numerical solutions with m=3.

Fig. 10. Comparison between the analytic solution, EFG method and MLPG method with 2500 nodes along y=0.5.

According to the results shown in Fig. 9 and Fig. 10, it can be concluded that both the EFG method and MLPG method work well for the Helmholtz problem. In addition, more nodes used in the model, more accurate of the results, this is the same as that in the example of Poisson's problem.

Based on the analytic solutions with different a_1 and a_2 in Poisson's problem, the relative error and computational efficiency of EFG and MLPG method are investigated.

In order to discuss the relationship of the relative error, the total number of nodes with different problems (different a_1 and a_2), a relative error with different number of nodes in EFG method and MLPG method is given in Fig. 11. Figure 11 shows the MLPG method is more accurate than EFG with the same number of nodes, especially when the total number of nodes is substantially lower. With the increase of total number of nodes used, the relative error of both EFG method and MLPG method are getting close to zero.

For the case where a_1=2 and a_2=5, the analytic electric potential is much more complex than the case where a_1=a_2=5, more nodes are required to get an exact answer.

To investigate the computational efficiency of the two methods, the average processing time required as a function of the total number of nodes is obtained and plotted in Fig. 12. It should be noted that he computation was done with the same Lenovo computer.

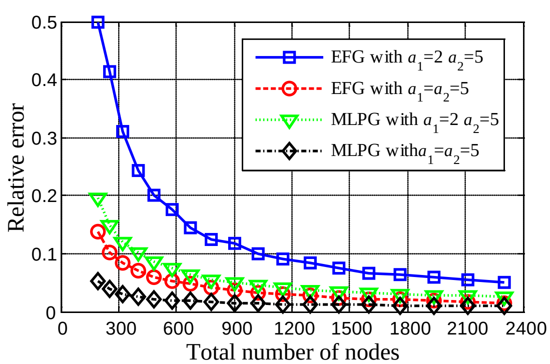

Fig. 11. Relative error with the total number of nodes in EFG and MLPG method.

It can be found that, the MLPG method needs more processing time than the EFG method. It is mainly due to the following two reasons: At first, the MLPG method requires more integration points than the EFG method in the computation. Both of the EFG method and the MLPG method need to integrate over the domain. The EFG method needs shadow meshes to set integration points over the entire domain of the problem. The MLPG method doesn't need elements or meshes for integration, all the integrals are carried out on spheres centered at each node in the domain, so the MLPG method can be referred to as a "real" meshless method or at least close to the ideal mesh-free method. But because of the complexity of the integrand that results from the Petrov-Galerkin formulation, the integration difficulty is more severe than EFG. The MLPG method needs to be divided into small cells and more Gaussian quadrature points should be used for the integration [15]. The second reason for the increased processing time is that the system matrices produced by the MLPG method are asymmetric and those that are produced by the EFG methods are symmetric. The asymmetric matrices require more CPU time for their solution.

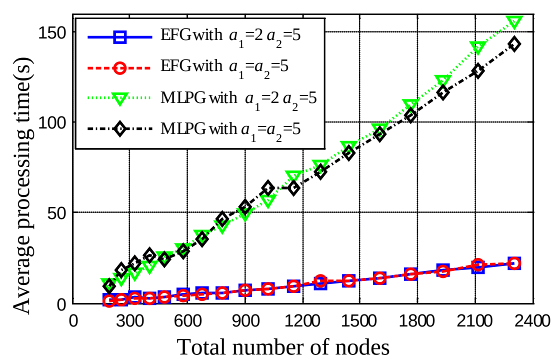

Fig. 12. Comparison of the proceeding time with different total number of nodes of EFG and MLPG method.

V. CONCLUSIONS

Implementations of the element free galerkin method (EFG) and the meshless local Petrov-Galerkin method have been presented in this paper. Both of the methods are formulated in detail for a basic problem governed by Poisson's equation. Problem domains governed by Poisson's and Helmholtz's equations have been considered and the numerical results are compared with the analytic solutions to investigate the accuracy and computational efficiency of the EFG method and the MLPG method. The results show that the MLPG method needs more CPU time but can obtain a more accurate result using fewer nodes than the EFG method. The reasons the MLPG method needs more processing time are that the MLPG method needs more integration points and the solution of the asymmetric matrices require more CPU time.

ACKNOWLEDGMENT

This work is supported by the Major State Basic Research Development Program of China (973 Program) (No. 2011CB209401), the National Natural Science Foundation of China (Grant No. 51007096) and Scientific Research Foundation of State Key Lab. of Power Transmission Equipment and System Security (2007DA10512711203 &2007DA10512711102).

REFERENCES

[1] Q. Li and K. M. Lee, "An adaptive meshless method for magnetic field computation," *Magnetics, IEEE Transactions on*, vol. 42, pp. 1996-2003, 2006.

[2] G. R. Liu, *Meshfree Methods: Moving Beyond the Finite Element Method*, Boca Raton, CRC, 2009.

[3] T. Belytschko, Y. Y. Lu and L. Gu, "Element-free Galerkin methods," *International Journal for Numerical Methods in Engineering*, vol. 37, pp. 229-256, 1994.

[4] I. Singh, "Meshless EFG method in three-dimensional heat transfer problems: a numerical comparison, cost and error analysis," *Numerical Heat Transfer Part A: Applications*, vol. 46, pp. 199-220, 2004.

[5] M. H. Afshar, M. Naisipour and J. Amani, "Node moving adaptive refinement strategy for planar elasticity problems using discrete least squares meshless method," *Finite Elements in Analysis and Design*, vol. 47, pp. 1315-1325, 2011.

[6] P. F. Thomas and G. M. Hermann, "Classification and overview of meshfree methods," *Institute of Scientific Computing, Technical University Braunschweig*, Brunswick, Germany, 2004.

[7] R. D. Soares, R. C. Mesquita, F. J. S. Moreira, “Axisymmetric electromagnetic resonant cavity solution by a meshless local Galerkin method,” *Applied Computational Electromagnetics Society (ACES) Journal*, vol. 26, pp. 792 – 799, 2011.

[8] R. K. Gordon, W. E. Hutchcraft, “The use of multiquadric radial basis functions in open region problems,” *Applied Computational Electromagnetics Society (ACES) Journal*, vol. 21, pp. 127 – 134, 2006.

[9] K. Y. Dai, G. R. Liu, K. M. Lim, and Y. T. Gu, "Comparison between the radial point interpolation and the Kriging interpolation used in meshfree methods," *Computational Mechanics*, vol. 32, pp. 60-70, 2003.

[10] M. Fooladi, H. Golbakhshi, M. Mohammadi, and A. Soleimani, "An improved meshless method for analyzing the time dependent problems in solid mechanics," *Engineering Analysis with Boundary Elements*, vol. 35, pp. 1297-1302, 2011.

[11] S. N. Atluri and S. Shen, "The meshless local Petrov-Galerkin (MLPG) method: A simple & less-costly alternative to the finite element and boundary element methods," *CMES: Computer Modeling in Engineering & Sciences*, vol. 3, pp. 11-52, 2002.

[12] S. Ikuno, K. Takakura and A. Kamitani, "Influence of Method for Imposing Essential Boundary Condition on Meshless Galerkin/Petrov Galerkin Approaches," *Magnetics, IEEE Transactions on*, vol. 43, pp. 1501-1504, 2007.

[13] P. Lancaster and K. Salkauskas, "Surfaces generated by moving least squares methods," *Mathematics of Computation*, vol. 37, pp. 141-158, 1981.

[14] J. Dolbow and T. Belytschko, "An introduction to programming the meshless Element Free Galerkin method," *Archives of Computational Methods in Engineering*, vol. 5, pp. 207-241, 1998.

[15] S. N. Atluri, H. G. Kim and J. Y. Cho, "A critical assessment of the truly meshless local Petrov-Galerkin (MLPG), and local boundary integral equation (LBIE) methods," *Computational Mechanics*, vol. 24, pp. 348-372, 1999.

Wei He was born in 1957. He earned his Ph.D. in Germany in 1996. Now he is a Professor in school of electrical engineering, Chongqing University, China. His main research interests are in the areas of electromagnetic theory, electromagnetism environment and EMC and medical imaging.

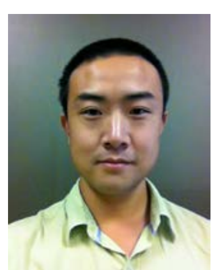

Zehui Liu was born in 1987, Henan Province, China. He got his B.S. in electrical engineering at Henan Polytechnic University at 2004. Now he is a Ph.D. candidate in the school of electrical engineering, Chongqing University, China. His research activities mainly include: electromagnetic environment of power system and meshless methods for solving electromagnetics problems.

Richard K. Gordon was born in Birmingham, Alabama on November 26, 1959. He earned his B.S. in physics at Birmingham Southern College, Birmingham, AL in 1983, his M.S. in mathematics at the University of Illinois, Urbana, IL in 1986 and his Ph. D. in electrical engineering at the University of Illinois, Urbana, IL in 1990. He is an Associate Professor in the Department of Electrical Engineering at the University of Mississippi in Oxford, Mississippi. Dr. Gordon is a member of Eta Kappa Nu, Phi Beta Kappa, and Tau Beta Pi.

W. Elliott Hutchcraft was born in Lexington, Kentucky on April 29, 1973. He earned his B.S. in electrical engineering at the University of Mississippi, Oxford, MS in 1996, and his M.S. in electrical engineering at the University of Mississippi, Oxford, MS in 1998 and his Ph. D. in electrical engineering at the University of Mississippi, Oxford, MS in 2003. He is an Associate Professor in the Department of Electrical Engineering at the University of Mississippi in Oxford, Mississippi. Dr. Hutchcraft is a member of Eta Kappa Nu, Sigma Xi, IEEE, Tau Beta Pi, Phi Kappa Phi, and ARFTG.

Fan Yang was born in ShanDong Province, China. Now he got his PhD degree in school of electrical engineering, Chongqing University, China and now he is an Associate Professor in electrical engineering of Chongqing University. His research of interests includes: high voltage electrical apparatus, electromagnetic devices and sensors, electromagnetic environment of power system.

Afei Chang was born in Anyang, Henan Province, China in 1986. She got her B.S. in electrical engineering at Henan Polytechnic University in 2004. She earned her M.S. in school of electrical engineering, Chongqing University, Chongqing, China. Now she is working in the State Nuclear Electric Power Planning Design & Research Institute, Beijing, China.

MoM Analysis of Apertures in Chiral Bodies of Revolution

Khaja Qutubuddin[1], Halid Mustacoglu[2], Joseph R. Mautz[1], and Ercument Arvas[1]

[1] Department of EECS
Syracuse University, Syracuse, NY 13244, USA
kqutubud@syr.edu, jrmautz@syr.edu, earvas@syr.edu

[2] Anaren Microwave, Inc.
East Syracuse, NY 13057, USA
hmustacoglu@anaren.com

Abstract **─** A chiral body of revolution (BOR) which is partially covered by a thin conducting shield is analyzed using the Method of Moments (MOM). The axisymmetric system is excited by a plane wave. The internal fields and the far scattered fields are computed. The problem is solved using the surface equivalence principle. The scattered fields outside the structure are assumed to be produced by an equivalent magnetic surface current that exists on the unshielded part of BOR surface and an external equivalent electric surface current that exists over the entire BOR surface. These two currents are assumed to radiate in the unbounded external medium. Similarly, the internal fields are assumed to be produced by the negative of the above magnetic current and an internal electric surface current that exists over the entire BOR surface, but is an independent unknown only on the shielded part of the BOR surface. These two currents radiate in the unbounded internal medium. Enforcing the boundary conditions at the surface of the BOR results in a set of coupled integral equations for the three equivalent surface currents. These equations are solved numerically using the MOM. The computed results for the partially shielded spherical chiral body are in excellent agreement with other data.

Index Terms **─** Aperture, body of revolution, chiral body, method of moments, equivalence principle.

I. INTRODUCTION

Figure 1 shows a chiral body of revolution that is partially covered by a perfectly conducting shield. The system is excited by a plane wave. We are interested in finding the field that penetrates into the chiral body through the apertures on its surface and the far field scattered by the structure. The problem of electromagnetic penetration into a regular dielectric body of revolution that is partially covered by a perfectly conducting shield is analyzed in [1] and [2]. The problem of electromagnetic transmission through an arbitrary aperture in an arbitrary 3-D conducting surface enclosing chiral material is analyzed in [3]. The electromagnetic analysis of general bodies of revolution is given in [4].

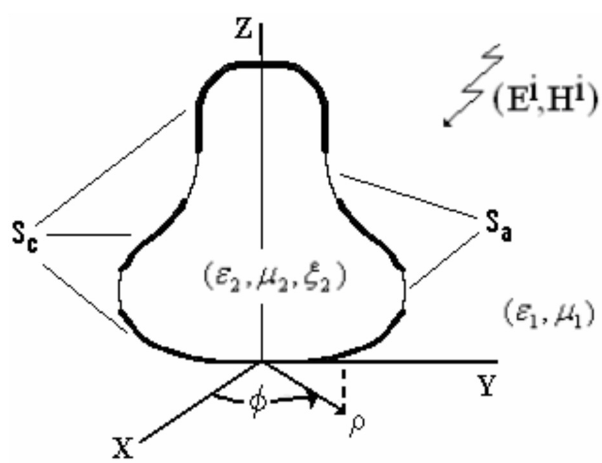

Fig. 1. A chiral body of revolution with two apertures.

Submitted On: Jan. 16, 2012
Accepted On: July 22, 2012

Penetration of electromagnetic waves through apertures has been studied extensively. Two dimensional apertures in thin infinite planes are studied in [5] and [6]. Apertures in arbitrarily shaped three dimensional objects are studied in [3] and [7]. In [3] the internal medium considered was chiral and in [7] both internal and external media were regular dielectrics. The research problem dealt with in [8] relates to a rotationally symmetric aperture on a perfectly conducting BOR containing the same homogeneous dielectric in the interior as well as the exterior. A boundary integral equation is used in [9] for dielectric objects partially coated with a perfectly conductive layer. Diffraction of an electromagnetic plane wave by a rectangular plate and a rectangular hole in the conducting plate [10] is rigorously tackled using the method of the Kobayashi potential (KP method).

In [11], there is a method applicable to arbitrarily-shaped apertures (in particular those not axially symmetric in bodies of revolution) employing the method of moments. The problem of the scattering of an electromagnetic plane wave with arbitrary polarization and angle of incidence from a perfectly conducting spherical shell with a circular aperture [12] is solved with a generalized dual series approach. In [13], the problem of scattering from a spherical shell with a circular aperture symmetrically illuminated by a plane electromagnetic wave is solved by expanding the fields inside and outside the cavity in terms of spherical vector wave functions. In [14], a hybrid FE−BI method that combines the finite element (FEM) and boundary integral (BI) methods is used to analyze electromagnetic scattering from structures consisting of an inhomogeneous dielectric body attached to perfectly conducting bodies. A new variational direct boundary integral equation approach is presented in [15] for solving the scattering and transmission problem for dielectric objects partially coated with a perfect electric conducting (PEC) layer. The absorption cross section of a dielectric sphere partially covered by a thin perfectly conducting spherical surface is calculated in [16]. Two-dimensional electromagnetic scattering by a dielectric cylinder partially covered by zero-thickness perfect conductors is treated in [17]. In [18], an axisymmetric chiral radome is analyzed via the method of moments. In [19], a method of moments solution is presented for electromagnetic scattering by a three-dimensional (3-D) inhomogeneous chiral scatterer illuminated by an arbitrary incident field.

This research work is important because of its significance for numerous applications in radar techniques and for tracking and discriminating between space vehicles and objects.

II. ANALYSIS

Let S_c be the part of the surface of the chiral body (scatterer) covered by rotationally symmetric perfect conductors, let S_a be the part of the surface of the scatterer not covered by the rotationally symmetric conductors, and let S be the entire surface of the scatterer as shown in Fig. 1. Here, the subscript "*c*" stands for conductor and the subscript "*a*" stands for aperture.

The surface equivalence principle is used to separate the problem of Fig. 1 into two simpler parts, namely, the region external to surface S and the region internal to S. The scattered fields in the external region are produced by an equivalent magnetic surface current **M** and an equivalent electric surface current $\mathbf{J}_e$ radiating in the unbounded external medium. The current **M** exists on only S_a and the current $\mathbf{J}_e$ exists on the whole surface S. The requirement that the tangential electric field of the external equivalence be zero just inside S is expressed as

$$-\frac{1}{\eta_e}\left[\mathbf{E}_e\left(\mathbf{J}_e,\mathbf{M}\right)\right]_{S^-}=\frac{1}{\eta_e}\left[\mathbf{E}^{inc}\right]_S, \qquad (1)$$

where $\eta_e=\sqrt{\mu_e/\varepsilon_e}$ is the intrinsic impedance of the homogeneous achiral medium outside the scatterer in the original problem. Also, $\mathbf{E}_e(\mathbf{J}_e, \mathbf{M})$ is the electric field of the combination of $\mathbf{J}_e$ and **M**, both radiating in all space filled with the homogeneous achiral medium that is outside the scatterer in the original problem. The subscript S^- denotes evaluation on the side of S facing inside the scatterer of the tangential part of the enclosed vector. In (1), $\left[\mathbf{E}^{inc}\right]_S$ is the tangential part of the incident electric field on S.

The requirement that the tangential magnetic field of the external equivalence be zero just inside S is expressed as

$$-\left[\mathbf{H}_e\left(\mathbf{J}_e,\mathbf{M}\right)\right]_{S^-}=\left[\mathbf{H}^{inc}\right]_S, \qquad (2)$$

where $\mathbf{H}_e(\mathbf{J}_e, \mathbf{M})$ is the magnetic field of the combination of $\mathbf{J}_e$ and $\mathbf{M}$, both radiating in all space filled with the homogeneous achiral medium that is outside the scatterer in the original problem.

The field in the chiral medium is produced by the equivalent magnetic surface current $-\mathbf{M}$, and an equivalent surface electric current $-\mathbf{J}_i$ radiating in the unbounded chiral medium. $\mathbf{J}_i$ exists on the whole surface S. The requirement that the tangential electric field of the internal equivalence be zero just outside S is expressed as

$$-\frac{1}{\eta_e}\left[\mathbf{E}_i\left(\mathbf{J}_{ie},\mathbf{M}\right)\right]_{S^+}=0, \tag{3}$$

where $\mathbf{E}_i(\mathbf{J}_{ie}, \mathbf{M})$ is the electric field of the combination of $\mathbf{J}_{ie}$ and $\mathbf{M}$, both radiating in all space filled with the homogeneous chiral medium that is inside the scatterer in the original problem. Here, $\mathbf{J}_{ie}$ is the combination of $\mathbf{J}_i$ on S_c and $\mathbf{J}_e$ on S_a. The subscript S^+ denotes evaluation on the side of S facing outside the scatterer of the tangential part of the enclosed vector.

The requirement that the tangential magnetic field of the internal equivalence be zero just outside S is expressed as

$$-\left[\mathbf{H}_i\left(\mathbf{J}_{ie},\mathbf{M}\right)\right]_{S^+}=0, \tag{4}$$

where $\mathbf{H}_i(\mathbf{J}_{ie}, \mathbf{M})$ is the magnetic field of the combination of $\mathbf{J}_{ie}$ and $\mathbf{M}$, both radiating in all space filled with the homogeneous chiral medium that is inside the scatterer in the original problem.

In view of (1) – (4), the equivalent currents $\mathbf{J}_e$ and $\mathbf{M}$ of the external equivalence and the equivalent currents $-\mathbf{J}_{ie}$ and $-\mathbf{M}$ of the internal equivalence assure that there is no electric field on both sides of S_c and that the tangential electric and magnetic fields are continuous across S_a.

The product of an arbitrary constant α with (3) is added to (1) to obtain

$$-\frac{1}{\eta_e}\left[\mathbf{E}_e\left(\mathbf{J}_e,\mathbf{M}\right)\right]_{S^-} -\frac{\alpha}{\eta_e}\left[\mathbf{E}_i\left(\mathbf{J}_{ie},\mathbf{M}\right)\right]_{S^+}=\frac{1}{\eta_e}\left[E^{inc}\right]_S, \tag{5}$$

and the product of an arbitrary constant β with (4) is added to (2) to obtain

$$-\left[\mathbf{H}_e\left(\mathbf{J}_e,\mathbf{M}\right)\right]_{S^-}-\beta\left[\mathbf{H}_i\left(\mathbf{J}_{ie},\mathbf{M}\right)\right]_{S^+}=\left[\mathbf{H}^{inc}\right]_S. \tag{6}$$

The method of moments as applied to bodies of revolution is used to solve (5) and (6) numerically. Piecewise linear variation of the currents is assumed along the generating curve of the BOR. The variation of the currents along the circumferential direction is represented by Fourier series. An approximate Galerkin's method is used for testing. If αβ* is real and positive where * denotes the complex conjugate, then it can be shown that (5) and (6) imply (1)–(4) [20, Section 2]. Equations (5) and (6) are two vector equations on S where the unknowns in (5) and (6) are $\mathbf{J}_e$ on S and the composite unknown consisting of $\mathbf{J}_i$ on S_c and $\mathbf{M}$ on S_a.

A. Expansion functions and testing functions

Let electric and magnetic currents $\mathbf{J}_e$, $\mathbf{J}_{ie}$, and $\mathbf{M}$ be expanded as

$$\mathbf{J}_e=\sum_{n=-N}^{N}\sum_{j=1}^{N_t}\left(I_{nj}^t\mathbf{J}_{nj}^t+I_{nj}^\phi\mathbf{J}_{nj}^\phi\right) \tag{7}$$

$$\mathbf{J}_{ie}=\sum_{n=-N}^{N}\sum_{j=1}^{N_t}\left(\left(L_j'V_{nj}^t+L_jI_{nj}^t\right)\mathbf{J}_{nj}^t+\left(L_j'V_{nj}^\phi+L_jI_{nj}^\phi\right)\mathbf{J}_{nj}^\phi\right) \tag{8}$$

$$\mathrm{M}=\eta_e\sum_{n=-N}^{N}\sum_{j=1}^{N_t}L_j\left(V_{nj}^t\mathbf{J}_{nj}^t+V_{nj}^\phi\mathbf{J}_{nj}^\phi\right), \tag{9}$$

where I_{nj}^t, I_{nj}^ϕ, V_{nj}^t, and V_{nj}^ϕ are complex constants to be determined and $\mathbf{J}_{nj}^t$ and $\mathbf{J}_{nj}^\phi$ are expansion functions given by

$$\mathbf{J}_{nj}^t=\hat{\mathrm{t}}\frac{T_j\left(t\right)}{\rho}e^{jn\phi} \tag{10}$$

$$\mathbf{J}_{nj}^\phi=\hat{\phi}\frac{T_j\left(t\right)}{\rho}e^{jn\phi}, \tag{11}$$

where t is the arc length along the generating curve C of the body of revolution (BOR), $\rho=\rho\left(t\right)$ is the distance from the z-axis of the BOR, ϕ is the angle measured from the positive x-axis toward the y-axis in the xy-plane, and $T_j\left(t\right)$ is the triangular function defined by

$$T_j\left(t\right)=\begin{cases}\dfrac{t-t_{2j-1}}{d_j}, & t_{2j-1}\le t\le t_{2j+1}\\ \dfrac{t_{2j+3}-t}{d_{j+1}}, & t_{2j+1}\le t\le t_{2j+3}\\ 0, & elsewhere\end{cases}, \tag{12}$$

where

$$d_j=\Delta_{2j-1}+\Delta_{2j} \tag{13}$$

$$\Delta_j = t_{j+1} - t_j . \tag{14}$$

The generating curve C consists of the straight line segment from $t=t_1$ to $t=t_2$, that from t_2 to t_3,…, that from $t_{2\mathrm{Nt}+2}$ to $t_{2\mathrm{Nt}+3}$ where, as in (7), N_t is the number of triangles on C. In (8) and (9),

$$L_j = \begin{cases} 1, & T_j(t) \text{ is in an aperture} \\ 0, & T_j(t) \text{ is on a conductor} \end{cases} \tag{15}$$

$$L'_j = \begin{cases} 1, & T_j(t) \text{ is on a conductor} \\ 0, & T_j(t) \text{ is in an aperture.} \end{cases} \tag{16}$$

Testing functions $\mathbf{J}^t_{-mi}$ and $\mathbf{J}^\phi_{-mi}$ are defined by

$$\mathbf{J}^t_{-mi} = \hat{\mathrm{t}} \frac{T_i(t)}{\rho} e^{-jm\phi} \tag{17}$$

$$\mathbf{J}^\phi_{-mi} = \hat{\phi} \frac{T_i(t)}{\rho} e^{-jm\phi} . \tag{18}$$

Henceforth, we assume that (7)–(9) have been substituted into (5) and (6). The symmetric product of two vector functions is the integration over S of their dot product. First taking the symmetric product of $\mathbf{J}^t_{-mi}$ with (5), then taking the symmetric product of $\mathbf{J}^\phi_{-mi}$ with (5), next taking the symmetric product of $\mathbf{J}^t_{-mi}$ with (6), and finally taking the symmetric product of $\mathbf{J}^\phi_{-mi}$ with (6), one obtains, for (i=1,2,…, N_t) and for (m= –N, –N+1,…,N), the following matrix equation.

$$\begin{bmatrix} Z_n^{tt} & Z_n^{t\phi} & C_n^{tt} & C_n^{t\phi} \\ Z_n^{\phi t} & Z_n^{\phi\phi} & C_n^{\phi t} & C_n^{\phi\phi} \\ D_n^{tt} & D_n^{t\phi} & Y_n^{tt} & Y_n^{t\phi} \\ D_n^{\phi t} & D_n^{\phi\phi} & Y_n^{\phi t} & Y_n^{\phi\phi} \end{bmatrix} \begin{bmatrix} I_n^t \\ I_n^\phi \\ V_n^t \\ V_n^\phi \end{bmatrix} = \begin{bmatrix} \vec{V}_n^t \\ \vec{V}_n^\phi \\ \vec{I}_n^t \\ \vec{I}_n^\phi \end{bmatrix} \tag{19}$$

For (n= –N, –N+1,…, N) where, for $q=t$ or $q=\phi$, I_n^q and V_n^q are column matrices whose j^{th} elements are I_{nj}^q and V_{nj}^q, respectively. The ij^{th} elements of the members of the 4×4 array in (19) are, for $p=t$ or $p=\phi$ and $q=t$ or $q=\phi$,

$$Z_{nij}^{pq} = \iint_S \mathbf{J}^p_{-ni} \cdot \left[-\frac{1}{\eta_e} \mathbf{E}_e\left(\mathbf{J}^q_{nj}, 0\right) \right]_{S^-} dS$$

$$+L_j \iint_S \mathbf{J}^p_{-ni} \cdot \left[-\frac{\alpha}{\eta_e} \mathbf{E}_i\left(\mathbf{J}^q_{nj}, 0\right) \right]_{S^+} dS \tag{20}$$

$$C_{nij}^{pq} = L_j \left(\iint_S \mathbf{J}^p_{-ni} \cdot \left[-\mathbf{E}_e\left(0, \mathbf{J}^q_{nj}\right) \right]_{S^-} dS \right.$$

$$\left. + \iint_S \mathbf{J}^p_{-ni} \cdot \left[-\alpha \mathbf{E}_i\left(0, \mathbf{J}^q_{nj}\right) \right]_{S^+} dS \right)$$

$$+L'_j \iint_S \mathbf{J}^p_{-ni} \cdot \left[-\frac{\alpha}{\eta_e} \mathbf{E}_i\left(\mathbf{J}^q_{nj}, 0\right) \right]_{S^+} dS \tag{21}$$

$$D_{nij}^{pq} = \iint_S \mathbf{J}^p_{-ni} \cdot \left[-\mathbf{H}_e\left(\mathbf{J}^q_{nj}, 0\right) \right]_{S^-} dS$$

$$+L_j \iint_S \mathbf{J}^p_{-ni} \cdot \left[-\beta \mathbf{H}_i\left(\mathbf{J}^q_{nj}, 0\right) \right]_{S^+} dS \tag{22}$$

$$Y_{nij}^{pq} = L_j \left(\iint_S \mathbf{J}^p_{-ni} \cdot \left[-\eta_e \mathbf{H}_e\left(0, \mathbf{J}^q_{nj}\right) \right]_{S^-} dS \right.$$

$$\left. + \iint_S \mathbf{J}^p_{-ni} \cdot \left[-\beta\eta_e \mathbf{H}_i\left(0, \mathbf{J}^q_{nj}\right) \right]_{S^+} dS \right)$$

$$+L'_j \iint_S \mathbf{J}^p_{-ni} \cdot \left[-\beta \mathbf{H}_i\left(\mathbf{J}^q_{nj}, 0\right) \right]_{S^+} dS . \tag{23}$$

For $p=t$ or $p=\phi$, the i^{th} elements of $\vec{V}_n^p$ and $\vec{I}_n^p$ are, respectively, $\vec{V}_{ni}^p$ and $\vec{I}_{ni}^p$ given by

$$\vec{V}_{ni}^p = \iint_S \mathbf{J}^p_{-ni} \cdot \left[\frac{1}{\eta_e} \mathbf{E}^{inc} \right]_S dS \tag{24}$$

$$\vec{I}_{ni}^p = \iint_S \mathbf{J}^p_{-ni} \cdot \left[\mathbf{H}^{inc} \right]_S dS . \tag{25}$$

The preceding discretization gives the 2N+1 small matrix equations {(19) for n=–N, –N+1,…, N} instead of one large matrix equation because, due to the rotational symmetry, an $e^{jn\phi}$ dependent current source produces only an $e^{jn\phi}$ dependent field.

III. COMPUTED RESULTS

Numerical results are given for the bodies shown in Fig. 2.

Figs. 3 to 8 are for a chiral sphere contained in a perfectly conducting thin metallic spherical shell with a single aperture of $\alpha_0 = 30°$ at its bottom that exposes the chiral material to the unit plane wave that illuminates the bottom of the sphere, as shown in Figure 2. The purpose of choosing this partially covered chiral sphere is to compare our results with those of early researchers, particularly with graphic results in [3]. The generating curve is approximated by 1200 straight line segments for Figs. 3 and 5.

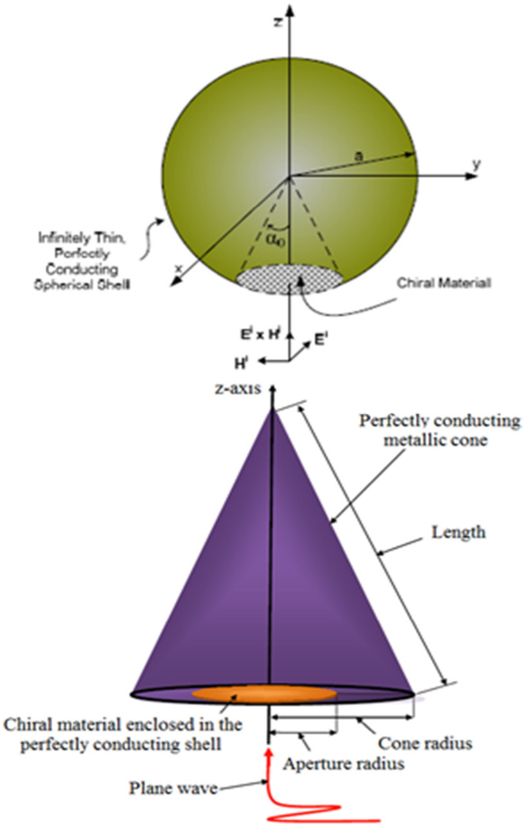

Fig. 2. Sphere and cone with single aperture.

We see marked resemblance between our graph of Fig. 3 and that of the insert from [3], Fig. 4. Both graphs indicate insignificant variations in the overall RCS values as relative chirality varies from ξ_r=0.2 to ξ_r=0.9 with parameters $k_e a$=1.5, ε_r=2, and μ_r=1.

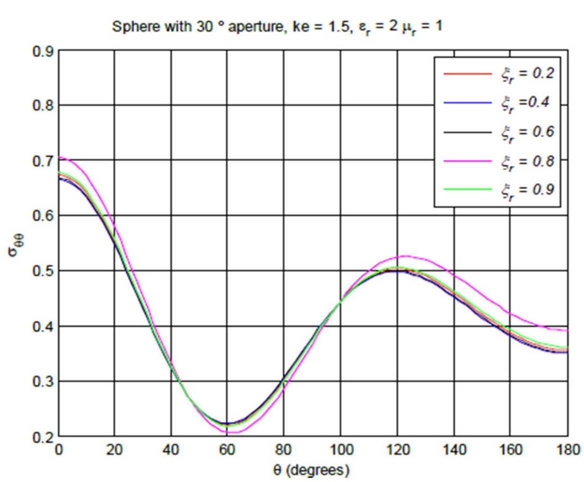

Fig. 3. $\sigma_{\theta\theta}/\lambda_0^2$ of the obstacle with 30° aperture at its bottom.

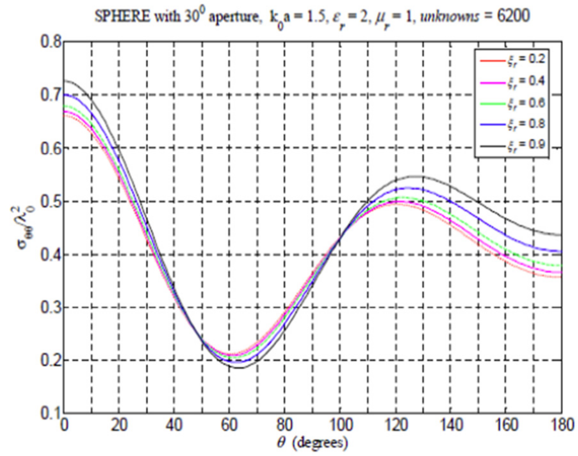

Fig. 4. $\sigma_{\theta\theta}/\lambda_0^2$ of the obstacle with 30° aperture at its bottom. (Insert taken from [3]).

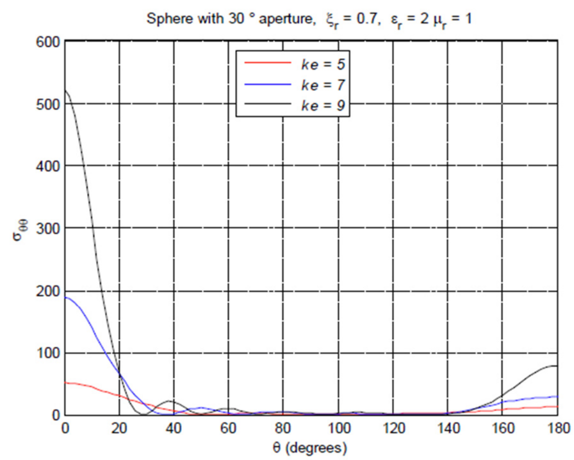

Fig. 5. $\sigma_{\theta\theta}/\lambda_0^2$ of the obstacle with 30° aperture at its bottom.

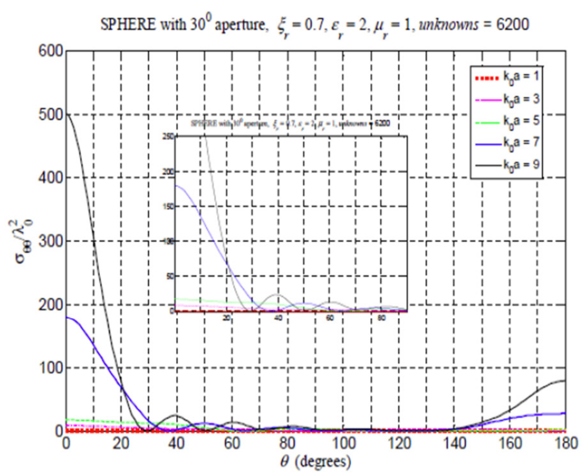

Fig. 6. $\sigma_{\theta\theta}/\lambda_0^2$ of the obstacle with 30° aperture at its bottom. (Insert taken from [3]).

We see marked resemblance between our graph of Fig. 5 and that of the insert from [3], Fig. 6.

Figures 7 and 8 show the internal electric fields along the *z*-axis of the body with varying chiralities. The generating curve is approximated by 3132 straight line segments and 102 points on the *z*-axis were used to obtain the graphs.

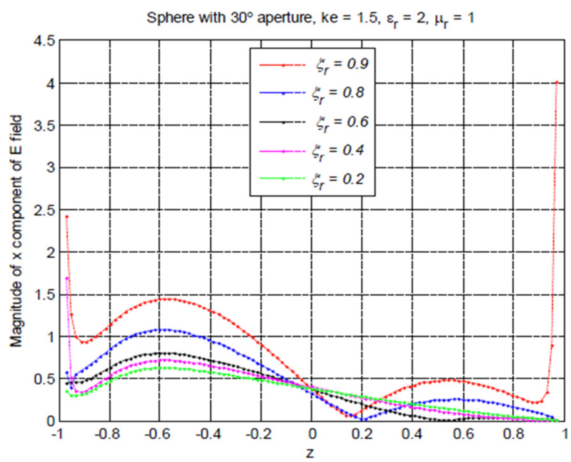

Fig. 7. Magnitude of *x*-component of internal electric field along *z*-axis.

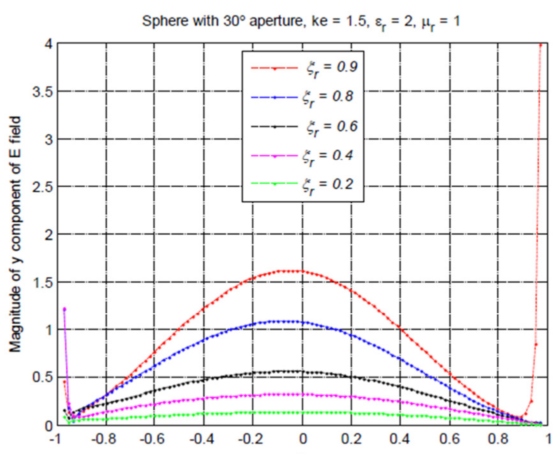

Fig. 8. Magnitude of *y*-component of internal electric field along *z*-axis.

Figs. 9 and 10 are for a conical-shaped chiral BOR contained in a perfectly conducting thin metallic shell with a single aperture at its bottom that exposes the chiral material to the plane wave that illuminates the BOR along the *z*-axis from the bottom of the conical shell, as shown in Figure 2. The radius of the aperture is 0.5m, the radius of the cone is 1m, and the length of the cone is 2m. The generating curve is approximated by 3132 straight line segments.

More results for these structures are available in [21].

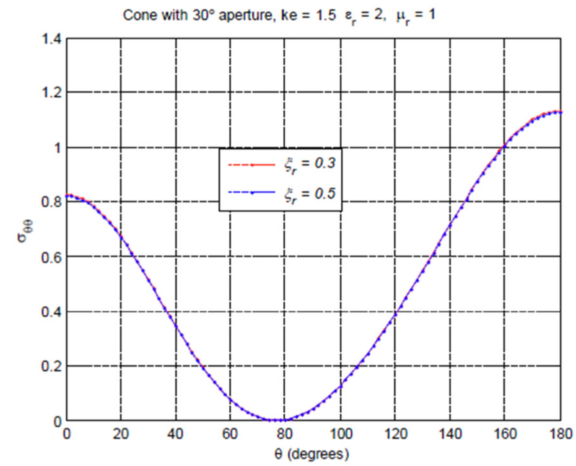

Fig. 9. $\sigma_{\theta\theta}/\lambda_0^2$ of the obstacle with single aperture at its bottom.

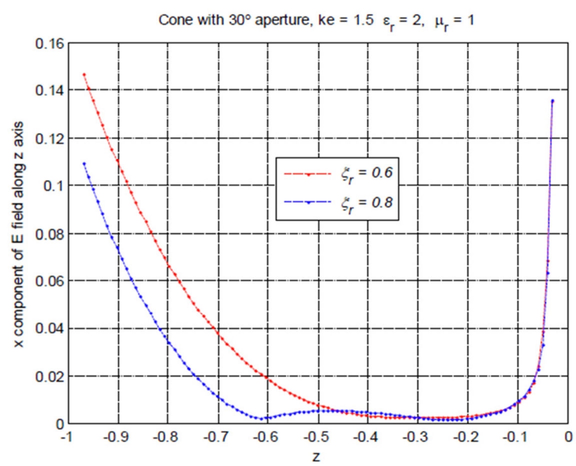

Fig. 10. Magnitude of *x*-component of internal electric field along *z*-axis.

VI. CONCLUSION

In this paper, plane wave incidence on a homogeneous chiral body partially covered by a thin perfectly conducting surface is investigated using the surface equivalence principle and MoM.

The body is replaced by equivalent electric and magnetic surface currents, which produce the correct fields inside and out. The application of the boundary conditions on the tangential components of the electric and the magnetic fields results in a set of two equations to be solved. Triangular expansion functions are used for both *t*-directed and ϕ-directed currents. The unknown coefficients of these expansion functions are obtained using the method of moments.

The inside fields and the scattering cross section are computed. The results are generated by a computer code, which produces agreement with available published results.

The theoretical framework presented in this paper can be used to obtain results that are not available elsewhere.

REFERENCES

[1] H. K. Schuman and D. E. Warren, "Coupling Through Rotationally Symmetric Apertures in Cavities of Revolution," Rome air Development Center, RADC-TR-77-214, Phase Report, June 1977.

[2] H. K. Schuman and D. E. Warren, "Aperture Coupling in Bodies of Revolution," *IEEE Trans. Antennas Propagat.*, vol. AP-26, no. 6, pp. 778-783, November 1978.

[3] F. Altunkilic, "Transmission Through an Arbitrary Aperture in an Arbitrary 3-D Conducting Surface Enclosing Chiral material," Ph.D. dissertation, Syracuse University, September 2007.

[4] J. R. Mautz and R. F. Harrington, "Radiation and Scattering from Bodies of Revolution," *Appl. Sci. Res.*, vol. 20, no. 6, pp. 405-435, June 1969.

[5] C. M. Butler and K. R. Umashankar, "Electromagnetic Penetration Through an Aperture in an Infinite, Planar Screen Separating Two Half Spaces of Different Electromagnetic Properties," *Radio Sci.*, vol. 11, no. 7, pp. 611-619, July 1976.

[6] S. T. Imeci, F. Altunkilic, J. R. Mautz, and E. Arvas, "Transmission Through an Arbitrarily Shaped Aperture in a Conducting Plane Separating Air and a Chiral Medium," *Applied Computational Electromagnetics Society (ACES) Journal*, vol. 25, no. 7, pp. 587-599, July 2010.

[7] T. Wang, R. F. Harrington, and J. R. Mautz, "Electromagnetic Scattering from and Transmission Through Arbitrary Apertures in Conducting Bodies," *IEEE Trans. Antennas Propagat.*, vol. 38, no. 11, pp. 1805-1814, Nov. 1990.

[8] H. K. Schuman and B. J. Strait, "Aperture Coupling in Bodies of Revolution," *IEEE Int. Antenna Propagat. Symp. Dig.*, vol. 14, pp. 507-510, Oct. 1976.

[9] B. Cranganu-Cretu and R. Hiptmair, "Scattering from Apertures: A General Boundary Integral Equations Based Approach," *Rev. Roum. Sci. Techn. - Electrotechn. et Energ.*, vol. 49, no. 4, pp. 1-20, 2004.

[10] K. Hongo and H. Serizawa, "Diffraction of Electromagnetic Plane Wave by a Rectangular Plate and a Rectangular Hole in the Conducting Plate," *IEEE Trans. Antennas Propagat.*, vol. 47, no. 6, pp. 1029-1041, June 1999.

[11] H. K. Schuman and B. J. Strait, "Coupling Through Apertures of Arbitrary Shape in Bodies of Revolution," *IEEE Int. Antennas Propagat. Symp. Dig.*, vol. 13, pp. 85-88, June 1975.

[12] R. W. Ziolkowski and W. A. Johnson, "Electromagnetic Scattering of an Arbitrary Plane Wave from a Spherical Shell with a Circular Aperture," *J. Math. Phys.*, vol. 28, no. 6, pp. 1293-1314, June 1987.

[13] T. B. A. Senior and G. A. Desjardins, "Electromagnetic Field Penetration into a Spherical Cavity," *IEEE Trans. Electromagn. Compat.*, vol. EMC-16, no. 4, pp. 205-208, Nov. 1974.

[14] Y. Hua, Q. Z. Liu, Y. L. Zou, and L. Sun, "A Hybrid FE-BI Method for Electromagnetic Scattering from Dielectric Bodies Partially Covered by Conductors," *J. of Electromagn. Waves and Appl.*, vol. 22, pp. 423-430, 2008.

[15] B. Cranganu-Cretu and R. Hiptmair, "Direct Boundary Integral Equation Method for Electromagnetic Scattering by Partly Coated Dielectric Objects," *Comput. Visual. Sci.*, vol. 8, nos. 3-4, pp. 145-158, 2005.

[16] S. S. Vinogradov and A. V. Sulima, "Calculation of the Absorption Cross Section of a Partially Shielded Dielectric Sphere," *Radio Physics and Quantum Electronics*, vol. 26, no. 10, pp. 927-931, 1984. Translated from *Izvestiya Vysshikh Uchebnykh Zavedenii, Radiofizika*, vol. 26, no. 10, pp. 1276-1281, Oct. 1983.

[17] X. Yuan, R. F. Harrington, and S. S. Lee, "Electromagnetic Scattering by a Dielectric Cylinder Partially Covered by Conductors," *J. Electromag. Waves Appl.*, vol. 2, no. 1, pp. 21-44, 1988.

[18] H. Mustacoglu, J. R. Mautz, and E. Arvas, "Method of Moments Analysis of an Axisymmetric Chiral Radome," *General Assembly and Scientific Symposium*, 2011 XXXth URSI, Oct. 2011.

[19] M. Hasanovic, C. Mei, J. R. Mautz, and E. Arvas, "Scattering from 3-D Inhomogeneous Chiral Bodies of Arbitrary Shape by the Method of Moments," *IEEE Trans. Antennas Propagat.*, vol. 55, no. 6, June 2007.

[20] J. R. Mautz and R. F. Harrington, "Electromagnetic Scattering from a Homogeneous Material Body of Revolution," *AEÜ*, vol. 33, no. 2, pp. 71-80, 1979.

[21] K. Qutubuddin, "MoM Analysis of Apertures in Chiral Bodies of Revolution," Ph.D. Dissertation, Syracuse University, January 2012.

Khaja Qutubuddin received his M.S. degree in Engineering Science from Florida State University in 1968 and Computer Engineer degree from Syracuse University, in 2002. He worked from 1968 until 2006 as Associate Professor and later as Professor in the Technology Department of Onondaga Community College, Syracuse, NY. His primary fields of interest are electromagnetic waves and fields and microwave engineering.

Halid Mustacoglu was born in Kocaeli, Turkey, in 1980. He received the B.S. degree in electronics and communication engineering from Yildiz Technical University, Istanbul, Turkey, in 2002 and the M.S. and Ph.D. degrees in electrical engineering from Syracuse University, Syracuse, NY, in 2005 and 2011, respectively.

From 2002 to 2003, he was a Research Assistant at Syracuse University and between 2003 and 2004 he was an intern at Herley Microwave, working on microwave filter designs. From 2004 to 2011, he was a co-op at Anaren Microwave, Inc., where he worked on passive component designs. Since 2011, he has been an RF/Microwave Engineer at Anaren Microwave, Inc., where he designs RF/Microwave components. His research interests include RF/Microwave design, scattering problems, and computational electromagnetics.

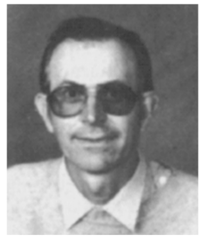

Joseph R. Mautz was born in Syracuse, NY, in 1939. He received the B.S., M.S., and Ph.D. degrees in electrical engineering from Syracuse University in 1961, 1965, and 1969, respectively.

Until July 1993, he was a Research Associate with the Electrical Engineering and Computer Science Department, Syracuse University, where he worked on radiation and scattering problems. Currently, he is affiliated with the Electrical Engineering and Computer Science Department at the same university. His primary fields of interest are electromagnetic theory and applied mathematics.

Ercument Arvas received the B.S. and M.S. degrees from the Middle East Technical University, Ankara, Turkey, in 1976 and 1979, respectively, and the Ph.D. degree from Syracuse University, Syracuse, NY, in 1983, all in electrical engineering.

From 1984 to 1987, he was with the Electrical Engineering Department, Rochester Institute of Technology, Rochester, NY. In 1987, he joined the Electrical Engineering and Computer Science Department, Syracuse University, where he is currently a Professor in the Electrical Engineering and Computer Science Department. His research and teaching interests are in electromagnetic scattering and microwave devices.

Prof. Arvas is a Member of the Applied Computational Electromagnetics Society (ACES).

A Novel Enhancing Technique for Parallel FDTD Method using Processor Affinity and NUMA Policy

Lei Zhao [1,2], Geng Chen [1], and Wenhua Yu [3]

[1] Center for Computational Science and Engineering, School of Mathematical Sciences
Jiangsu Normal University, Xuzhou, China
lzhaomax@163.com, gengchn@163.com

[2] State Key Laboratory of Millimeter Waves
Southeast University, Nanjing, China

[3] 2COMU, State College, PA 16803, USA
wenyu@2comu.com

Abstract **─** The traditional multiple CPUs mounted on one node in a high performance cluster is based on Symmetric Multi-Processing (SMP) architecture. The memory bandwidth is a major bottleneck in the high performance computing. Recently, Intel and AMD companies developed the (Non-uniform Memory Access (NUMA) architecture for the multi-CPU server that is an important extension of the SMP computer. In the NUMA architecture server, each CPU has its own memory and can also be access to the memory located the nearby of other CPUs through the onboard network. For a parallel code, we can allocate the data for each CPU inside its local memory to accelerate the memory access. In this paper, we investigate a way how to achieve the high performance of parallel FDTD code on a computer cluster that includes 21 nodes with 42 CPU and 168 cores. Numerical experiments have demonstrated that different job binding schemes can significantly affect the performance of parallel FDTD code.

Index Terms – NUMA, parallel FDTD, processor affinity, SMP.

I. INTRODUCTION

A high performance cluster has become a popular hardware platform today for the computational electromagnetic methods to solve the electrically large problems. In three popular computational electromagnetic methods, FDTD method [1] is parallel in nature, and hence, has high parallel performance than method of moment (MoM) [2], finite element method [3] due to a parallel FDTD method only requires the field exchange on the interface between the adjacent neighboring subdomains. For simulating electromagnetic (EM) problem from electrically-large and complex structures with FDTD method, parallel technology is a powerful tool to provide the necessary computing power and memory resources [4-8]. The parallel performance of FDTD code depends on not only the way how we develop the parallel FDTD code and problem type, but also on the hardware platform such as CPU type, network system, Input/Ouput (I/O) system, and the operating system as well. In this paper, the parallel FDTD code is developed based on the literature [7, 8] that uses the combination of Open Multiple Processing (OpenMP) [9] and Message passing Interface (MPI) library [10]. OpenMP is developed for the efficient use of multi-core processors and the MPI library is developed to use the distributed resource.

For the same parallel FDTD code, we investigate the performance of parallel FDTD code on an intermediate cluster that includes 21 nodes (42 CPUs with 168 cores) when we use the different binding techniques and the running environment variables. In all the numerical

Submitted On: Jan. 29, 2012
Accepted On: June 24, 2012

1054-4887

experiments, we do not modify the parallel FDTD code and keep the same hardware platform and operating system as well. Each node in the cluster includes two Intel Xeon X5520 2.67GHz processor, which support the NUMA architecture. Namely, it allows us to allocate the data for each CPU in one node to its local memory. If one job unit is assigned to one node, the communication between two CPUs in one node is realized through OpenMP. And the communication between the nodes is realized by the MPI functions. Otherwise, if one job unit is assigned to one core, all the communication between the cores is realized by the MPI functions. Furthermore, if one job unit is assigned to each CPU, the communication between the CPUs is realized by the MPI function but the communication between the cores inside each CPU is realized through OpenMP.

To achieve a good performance of the parallel FDTD code on the high performance cluster, the NUMA policy is used to extend the memory bandwidth and reduce memory access time by allocating the data for each CPU in its own local memory. The advantage of NUMA architecture is obvious from the numerical experiments. We also investigate the effect of processor affinity [11] on the parallel FDTD code performance by binding each rank to the node, CPU, or core. In this paper, all the test examples are carried out by using GEMS software [12].

II. THEORY AND METHOD

Both the electric and magnetic field updates in the FDTD method only require field information from their nearest neighboring cells, which requires much less communication information than other methods that require the 3-D communication data. Hence, the parallel FDTD method gives much less burden on the network system, and in turn, it generates the higher parallel efficiency. To achieve the better parallel performance, we install two sets of network systems in a regular cluster, one of them is design the data communication during the simulation and usually is fast. And the second one is designed the cluster management, namely, it allows simultaneously to check the cluster status without interrupting the data communication.

In Yee's scheme [1], the computational domain is discretized by using a rectangular grid. The electric fields are located along the edges of the electric elements, while the magnetic fields are sampled at the centers of the electric element surfaces and are oriented normal to these surfaces, this being consistent with the duality property of the electric and magnetic fields in Maxwell's equations, as shown in Fig. 1.

If the computational domain is broken into two subdomains, and the interface coincides with the FDTD mesh. The electric fields on the interface can be counted into either subdomain 1 or 2. For instance, if it is belong to the subdomain 1, we need to borrow the magnetic field H_z^2 from the subdomain 2 when we calculate the electric field $E_y^{\text{interface}}$ on the interface.

$$E_y^{\text{interface, n+1}} = E_y^{\text{interface, n}} + \frac{\Delta t}{\varepsilon_y} \cdot \left[\frac{H_x^{2,n+1/2} - H_x^{1,n+1/2}}{\Delta z} - \frac{H_z^{2,n+1/2} - H_z^{1,n+1/2}}{\Delta x} \right]. \quad (1)$$

We need to borrow the electric field $E_y^{\text{interface}}$ on the interface when we calculate the magnetic field H_z^2 in the subdomain 2:

$$H_z^{2,n+1/2} = H_z^{2,n-1/2} + \frac{\Delta t}{\mu_z} \left[\frac{E_x^{2,n} - E_x^{1}}{\Delta y} - \frac{E_y^{2,n} - E_y^{1,\text{interface}}}{\Delta x} \right]. \quad (2)$$

In the MPI library, the communication of the electric and magnetic fields between the subdomains 1 and 2 are realized by the MPI functions MPI_Send and MPI_Recv. The information is changed through the high performance network system. OpenMP is based on the fine grid technique in the shared memory system, and its information exchange is through a shared memory. In the optimization of the parallel FDTD code, we need to achieve a balance between the minimum area of interface and performance of network. Internal consistency should be maintained

Uniform Memory Access (UMA) is a shared memory architecture used in parallel computers, as shown in Fig. 2. In the UMA model, all the processors share the physical memory uniformly, and access time to a memory location is independent of which processor makes the request or which memory chip contains the transferred data. The UMA model is suitable for general purpose and time sharing applications by multiple users. Contrasted with UMA, NUMA is a shared memory architecture that describes the placement of main memory modules with respect to processors in a multiprocessor system, as shown in Fig. 3. Based on the idea, however, Intel and AMD use the different technical paths to realize the NUMA architecture.

To better understanding NUMA roles in parallel FDTD method, we do many simulations using GEMS with NUMA and UMA policy, respectively. For example, the command for running the GEMS project with NUMA is:

mpirun –np 9 -machinefile hosts nuamctl--physcpubind=0-8,9-15 /gpfsAPP/GEMS /GEMS_Solver test.gpv

and the command for running the GEMS project without NUMA is:

mpirun -np 9 -machinefile hosts /gpfsAPP /GEMS/GEMS_Solver test.gpv

In addition, job balancing plays an important role in determining performance of the parallel code. Proper job balancing can obtain good performance of the parallel FDTD code on the HPC system, while improper job balancing may reduce the performance of parallel code for most of the processors in the cluster to that of "waiting" during the simulation process. Another important factor that affects the parallel efficiency is the division of the sub-domains according to the allocation of the array in the computer's memory. Processor affinity is a modification of the native central queue scheduling algorithm in a symmetric multiprocessing operating system. Taking advantage of the fact that some remnants of a process may remain in one processor's state from the last time the process ran, we can enhance the performance of parallel FDTD code on a HPC cluster. For example, if we use two nodes (4 CPUS, 16 cores) to run GEMS with binding rank to nodes, CPUs and cores, respectively, we should first edit the rank files for banding nodes, CPUs and cores as following:

For binding nodes:

rank 0=host0 slot=0-7
rank 1=host1 slot=0-7

For binding CPUs:

rank 0=host0 slot=0-3
rank 1=host0 slot=4-7
rank 2=host1 slot=0-3
rank 3=host1 slot=4-7

For binding Cores:

rank 0=host0 slot=0
rank 1=host0 slot=1
rank 2=host0 slot=2
rank 3=host0 slot=3
rank 4=host0 slot=4
…….
rank 7=host0 slot=7
rank 8=host1 slot=0
… ….
rank 15=host1 slot=7

And the following commands will be used to run GEMS testing project.

mpirun -np n -machinefile hosts -rf ranks /opt/GEMS/bin64/GEMS_Solver test.gpv

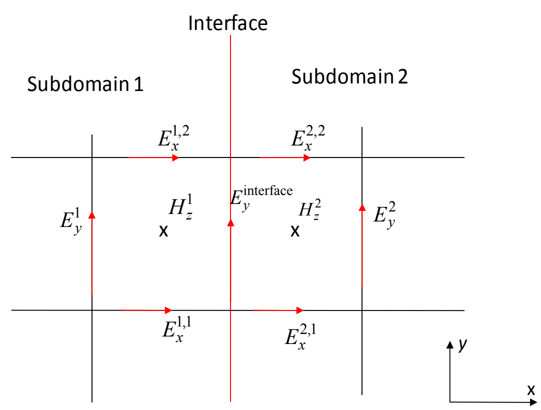

Fig. 1. Distributions of electric and magnetic fields near the subdomain interface.

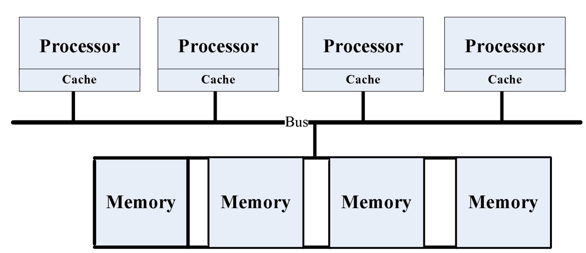

Fig. 2. UMA architecture.

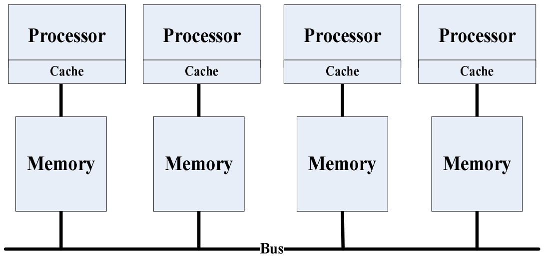

Fig. 3. NUMA architecture.

III. NUMERICAL EXPERIMENT RESULTS

In this section, we introduce a parallel processing platform installed with Linux operating system and investigate GEMS performance on the platform. The HPC cluster shown in Table 1 includes 23 nodes (21 computation nodes and 2 master nodes) and each node has two CPUs with Intel Xeon X5550 2.7GHz processor. The 10Gbps Ethernet is used to connect the computation nodes. To evaluate the performance of the FDTD code, we define the performance as follows:

$$Performance\left(Mcells/s\right) = \frac{\left(N_x \times N_y \times N_z\right) \times Number\_of\_timesteps}{Simulation\_time\ (\mathrm{second})}, \quad (3)$$

where N_x, N_y, N_z are the number of grids in *x, y* and *z* direction, respectively.

Firstly, NetPIPE [13] was used to test the performance of a network inside a node and internode. Table 2 gives NetPIPE results about the bandwidth, which shows that the network speed inside node is around 4 times of the internode. The NetPIPE results about the latency is described in Fig. 4, which shows the internode has a latency that is over 3 times than that inside-node. To test the job balancing role in determining performance of the parallel FDTD, a job with different processes has been run in one node of the HPC cluster. Fig. 5 shows the performance of the parallel code on one node with different processes, which indicates that job balancing plays an important role for performance of a parallel code.

An ideal case that is a hollow box with the simplest excitation and output, and its domain is truncated by using the Perfect Electric Conductor (PEC) boundary condition, was used as an example to study the impacts of processor affinity on parallel FDTD performance. The project settings including the number of unknowns, excitation type, output parameters and binging strategy (Binding each rank by node, by CPU and by core) are identical in the cluster simulations. Fig. 6 shows the performance of the parallel FDTD with different banding strategy, which indicates that parallel FDTD with banding rank to CPU give the best performance, and the worst case is banding rank to core. For example, the performances of the parallel FDTD code using 18 nodes are 5300 Mcells/sec, 4900 Mcells/sec, and 2700 Mcells/sec for binding rank to CPUs, nodes and cores, respectively. From the results shown in Fig. 6, we can also see that the job balancing between the internode and inside node play an important role to obtain good performance. If we bind each process to each core, we will suffer from the high latency of messages transmitting for there are more processes created between nodes. Binding each process to each node, we will not use the whole processor. However, if we choose to bind each process to CPU, all processors can be used and the latency of messages transmitting is less than that by banding to core.

Then, NUMA policy is used to reduce memory access time in the average case through the fast introduction of local memory. For NUMA providing each node with its own local memory, memory accesses, parallel code with NUMA policy can avoid throughput limitations. The performances of GEMS with NUMA policy are plotted in Fig. 7, where the numactl command is used as a plugin of GEMS software. As a compared date, the performances of GEMS without NUMA policy are also shown in Fig. 7. Comparing the results shown in Fig. 7, we can obtain that the performance of GEMS with NUMA is around 1.5 times than that without NUMA. For example, the performances of GEMS using 18 nodes of the HPC system are 3400 Mcells/sec and 5400 Mcells/sec for without NUMA policy and with NUMA policy, respectively.

Finally, we use the different options described above to simulate a reflector antenna fed by a dual mode circular horn, as shown in Fig. 8. The thinner horn part is excited by TE11 mode. The transit will generate the TM10 mode and have the same magnitude and out of phase with the TE11 mode at the end of the thicker horn. This horn will generate a very low slob by cancelling the fields generated by the TE11 and TM10 modes.

Table 1: HPC cluster information

Computation Nodes (21) Master Nodes(2)	CPU type	Intel Xeon E5520
	Clock speed	2.67GHz
	Number of nodes	23
	Available memory	12GB (DDR3 1067MHz)
	Operating system	Cent OS (Linux)
	Network system	BNT 10Gbps Ethernet

Table 2: NetPIPE testing results: bandwidth

Netpipe Testing	Internode	8822.02 Mbps
	Inside node	33462.93 Mbps

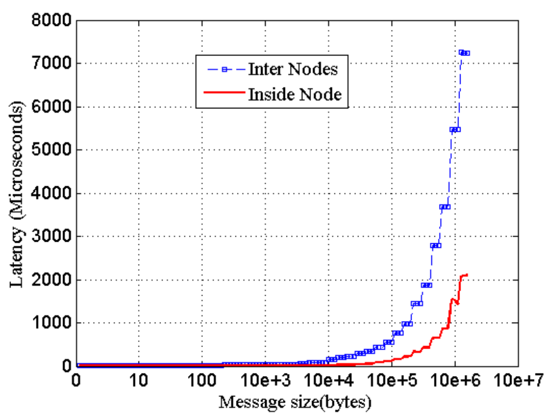

Fig. 4. NetPIPE testing results: latency.

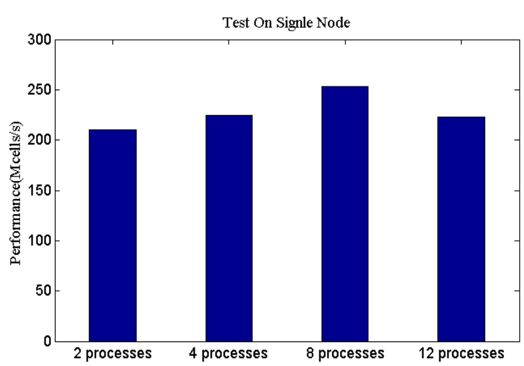

Fig. 5. Testing results about job balancing problem.

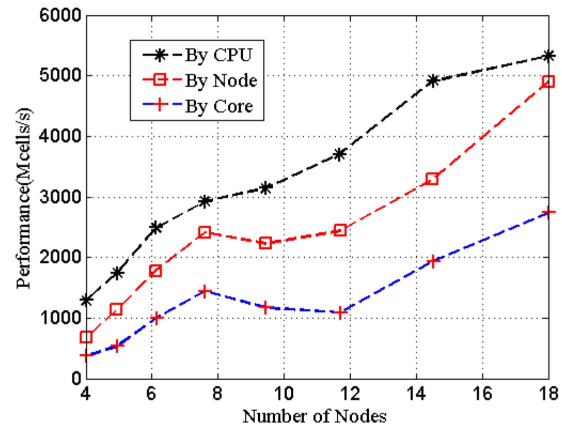

Fig. 6. Parallel FDTD performance with different binding strategy.

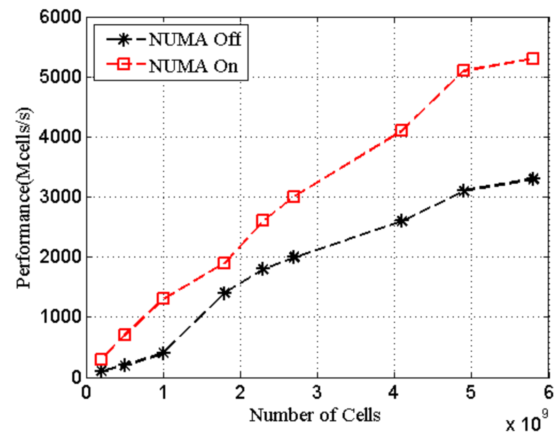

Fig. 7. Parallel PDTD performance with NUMA and without NUMA.

Finally, we use the different options described above to simulate a reflector antenna fed by a dual mode circular horn, as shown in Fig. 8. The thinner horn part is excited by TE11 mode. The transit will generate the TM10 mode and have the same magnitude and out of phase with the TE11 mode at the end of the thicker horn. This horn will generate a very low slob by cancelling the fields generated by the TE11 and TM10 modes.

Due to the symmetric property, we need only to simulate one quart of the original problem. The original domain size is 770 mm$\times$ 770 mm$\times$ 670 mm, and the one quart domain size is 385 mm $\times$ 385 mm $\times$ 670 mm, which is discretized into 569 $\times$ 569 $\times$ 1144 non-uniform cells. Output parameters include the far field pattern and return loss. This is a very large problem, which cannot be solved by two nodes of the HPC directly even using parallel FDTD method. The return loss of the reflector antenna is plotted in Fig.9, and Fig.10 gives directivity of the parabolic reflector antenna at working frequency 12GHz.

The comparison between with and without NUMA option is shown in Fig. 11, where 4 computation nodes are used to simulate the problem. Fig.11 shows that parallel FDTD with banding rank to CPU give the best performance, and the performance of GEMS with NUMA is around 1.5 times than that without NUMA. To investigate the parallel efficiency of the parallel FDTD, 18 computation nodes are used to simulate the parabolic reflector antenna fed by a dual mode circular horn. The performance and consumed time of parallel FDTD using 18 computation nodes are illustrated in Fig. 12. Comparing the results in Fig. 11 and Fig. 12, we can obtain that the parallel efficiency of parallel FDTD is almost 90%. For example, when we run the parallel FDTD code by binding each rank to CPU, the consumed time of parallel FDTD with NUMA using 4 nodes is 2 hours, and that using 18 nodes is 23 minutes.

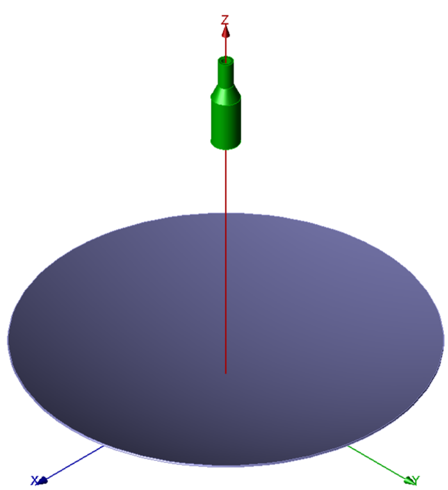

Fig. 8. Parabolic reflector antenna fed by a dual mode circular horn.

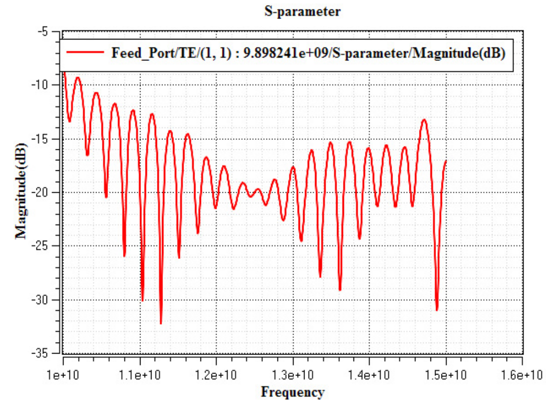

Fig. 9. Return loss of the parabolic reflector antenna.

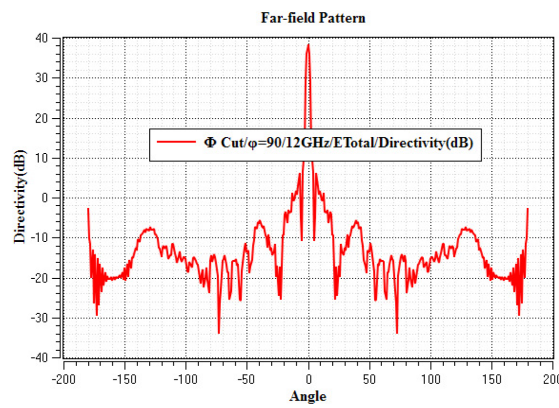

(A)

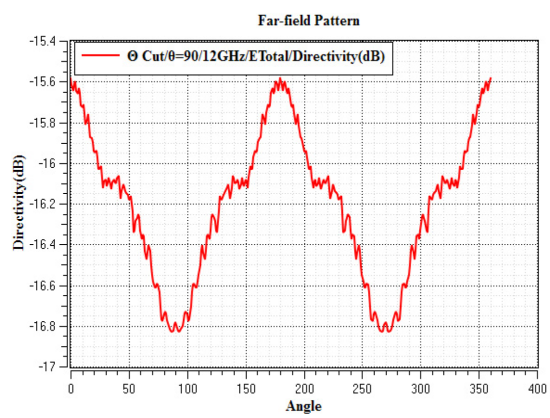

(B)

Fig. 10. Directivity of the parabolic reflector antenna at working frequency 12GHz. (A) ϕ cut-plane with $\phi = 90^0$ (B) θ cut-plane with $\theta = 90^0$.

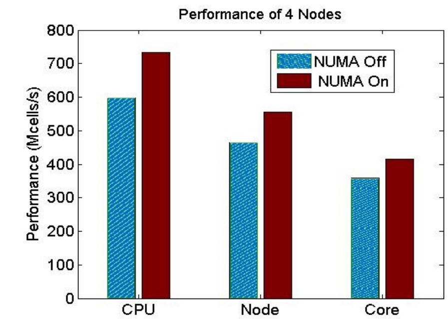

(A)

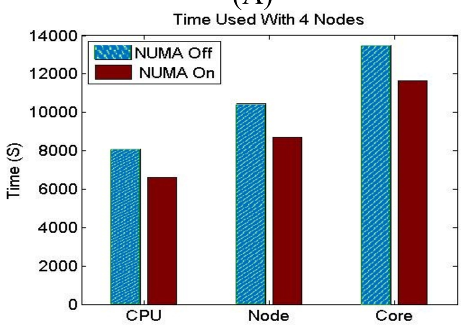

(B)

Fig. 11. Parallel FDTD with NUMA and without NUMA using 4 computation nodes. (A) Performance of parallel FDTD. (B) Consumed time of parallel FDTD.

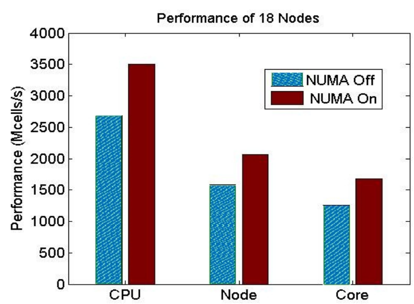

(A)

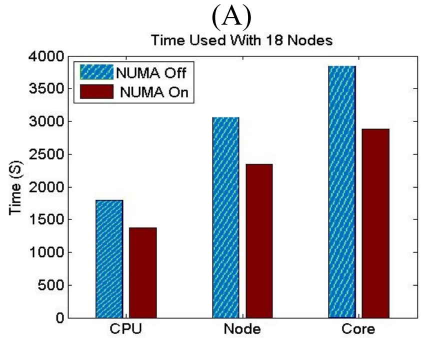

(B)

Fig. 12. Parallel FDTD with NUMA and without NUMA using 18 computation nodes. (A) Performance of parallel FDTD. (B) Consumed time of parallel FDTD.

IV. CONCLUSION

In this paper, the processor affinity and NUMA policy are used to enhance the performance of a parallel FDTD code on a HPC cluster. By binding each rank to the node, CPU and core, we investigate the effect of processor affinity on parallel FDTD code performance and find that the processor affinity has significant impacts on the performance. With the advantage of NUMA policy that can reduce memory access time, the parallel FDTD code using NUMA policy can obtain better performance than that without NUMA policy. The proposed methods for optimizing the performance of parallel FDTD code are suite for other parallel code, which is very useful enhance the performance of a HPC cluster.

ACKNOWLEDGMENT

This work was supported in part by the Natural Science Foundation of Jiangsu Province under Grant No. BK2010174, in part by Natural Science Foundation of the Jiangsu Higher Education Institutions under Grant No. 10KJB510025, in part by the Open Project of State Key Laboratory of Millimeter Waves under Grant No. K201008, and in part by Postgraduate Innovation Project of Jiangsu Province under Grant No. CXZZ11_0899.

REFERENCES

[1] A. Taflove and S. Hagness, *Computational Electromagnetics: The Finite-Difference Time-Domain Method*, 3rd ed., Artech House, Norwood, MA, 2005.

[2] Harrington, R. F., *Field Computation by Moment Methods*, MacMillan, New York, 1968.

[3] J. M. Jin, *The Finite Element Method in Electromagnetics* (2nd Edition), New York: John Wiley & Sons, 2002.

[4] F. L. Teixeira, “A Summary Review on 25 Years of Progress and Future Challenges in FDTD and FETD Techniques,” *Applied Computational Electromagnetics Society (ACES) Journal*, vol. 25, no. 1, pp. 1-14, 2010.

[5] V. Demir, “A Stacking Scheme to Improve the Efficiency of Finite-Difference Time-Domain Solutions on Graphics Processing Units,” *Applied Computational Electromagnetics Society (ACES) Journal*, vol. 25, no. 4, pp. 323 - 330, 2010.

[6] X. Duan, X. Chen, K. Huang, H. Zhou, “A High Performance Parallel FDTD Based on Winsock and Multi-Threading on a PC-Cluster,” *Applied Computational Electromagnetics Society (ACES) Journal*, vol. 26, no. 3, pp. 241 - 249, 2011.

[7] W. Yu, R. Mittra, T. Su, Y. Liu, and X. Yang, *Parallel Finite Difference Time Domain Method*, Artech House, Massachusetts, June, 2006.
[8] W. Yu, R. Mittra, X. Yang, and Y. Liu, *Electromagnetic Simulation Techniques Based FDTD Method*, John Wiley and Sons, 2009.
[9] W. Gropp, E. Lusk, and A. Skjellum, *Using MPI: Portable Parallel Programming with the Message-Passing Interface*, 2nd ed., MIT Press, Cambridge, MA, 1999.
[10] Optimizing software applications for NUMA Site: http://software.intel.com.
[11] C. Zhang, X. Yuan, and A. Srinivasan, "Processor Affinity and MPI Performance on SMP-CMP Clusters," *IEEE International Symposium on Parallel & Distributed Processing*, Workshops and PHD. Forum (IPDPSW), pp. 1-8, 2010.
[12] GEMS-A 3D Parallel EM simulation software package, www.2comu.com, State College, PA, 16801, USA.
[13] http://www.scl.ameslab.gov/netpipe/.

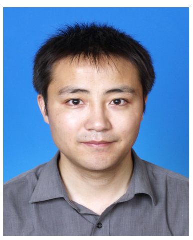

Lei Zhao received a BS in Mathematics from Jiangsu Normal University, Xuzhou, China, in 1997, and an MS in Computational Mathematics and a PhD in Electromagnetic Fields and Microwave Technology from Southeast University, Nanjing, China, in 2004 and 2007, respectively. From August 2007 to August 2009, he worked in the Department of Electronics Engineering, the Chinese University of Hong Kong, as a research Associate. Since September 2009, he has worked in the School of Mathematical Sciences, Jiangsu Normal University. He is also the Director of the Center of Computational Science and Engineering, which is affiliated with the Jiangsu Normal University. He has published over 20 technical papers. His current research interests include accurate numerical modeling, biomedical EM compatibility, and parallel computing in computational EM.

Geng Chen was born in Suqian, China, in February 1989. He received the BS degree in Computational Mathematics from Jiangsu Normal University in 2012, and is currently working toward the MS degree at Jiangsu Normal University, Xuzhou, China. His research interests include parallel-processing techniques, numerical methods, and software development.

Wenhua Yu joined the Department of Electrical Engineering of the Pennsylvania State University and has been a group leader of the Electromagnetic Communication Lab since 1996. He received his PhD in Electrical Engineering from the Southwest Jiaotong University in 1994. He worked at the Beijing Institute of Technology as a Postdoctoral Research Associate from February 1995 to August 1996. He has published five books related to the FDTD method, parallel-processing techniques, software-development techniques, and simulation techniques, from 2003 to 2009. He has published over 150 technical papers and four book chapters. He founded the Computer and Communication Unlimited company, and serves as President and CEO. He is a Senior Member of the I EEE. His research interests include computational electromagnetic methods, software-development techniques, parallel-processing techniques, simulation and design of antennas, antenna arrays, and microwave circuits.

A Comprehensive 2D FE-SIBC Model for Calculating the Eddy Current Losses in a Transformer Tank-Wall

J. M. Díaz-Chacón, C. Hernandez, and M. A. Arjona

División de Estudios de Posgrado e Investigación
Instituto Tecnológico de la Laguna, Torreón, Coah. 27000, México
jmauri12@gmail.com, coni.hernandez@ieee.org, marjona@ieee.org

***Abstract* ─** The calculation of the eddy-current losses is one of the most important aspects that must be considered in the design of transformers and electrical machines. In this paper, a comprehensive 2D finite element (FE) model for calculating the eddy-current losses in a tank-wall of the transformer is presented. The FE model takes into account the Surface Impedance Boundary Condition (SIBC). A detailed 2D-SIBC formulation in terms of the magnetic vector potential is described. The SIBC is incorporated into the FE formulation by using the Galerkin method. An axi-symmetric electromagnetic model of the transformer is solved by applying the SIBC formulation for calculating the loss intensity distribution along the vertical tank-wall. To demonstrate the validity of the SIBC formulation, the results are compared against those computed with a model based on first-order triangular elements. The advantages of using the SIBC formulation in the modeling of power transformers are highlighted.

Index Terms – Eddy current losses, finite element method, power transformer, surface impedance boundary condition.

I. INTRODUCTION

The Finite Element Method (FEM) is a computational tool that can be applied in several fields of electrical engineering where knowledge of electromagnetic fields is needed [1]. Alwash et al. used the 3D-FEM to analyze a helical motion induction motor [2]. Afjei et al. applied the finite element (FE) in a switched reluctance generator under faulty conditions [3]. B. Ali et al. presented a 3D-FEM analysis in modeling periodic structures using high-order multiscalets functions [4]. Wan et al. implemented an efficient FE time-domain method via a hierarchical matrix algorithm for electromagnetic simulation [5]. Torkaman et al. applied the 3D-FEM to evaluate the main characteristics of a three-phase external rotor switched reluctance motor [6].

The power transformer is an essential component and the most expensive asset within the transmission and distribution electrical networks [7]. A transformer includes several metallic parts, such as frames, shunts, and the tank. In these metallic parts, the stray losses are generated by the magnetic flux leakage of the transformer windings. The prediction of the stray losses in the transformer is fundamental at the design stage. This can help to avoid the presence of hot spots on the surface of metallic components. In oil-immersed transformers, the appearance of hot spots may provoke an undesirable overheating of conductive regions. This may generate internal gases, which may lead to the transformer failure [8].

In conductive regions exposed to time varying electromagnetic fields where the penetration depth is much smaller than their domain size, the Surface Impedance Boundary Condition (SIBC) can be used to reduce the FE model size. Hence, the aim of combining the FEM and the SIBC is to reduce the computational cost needed in the solution of an eddy-current problem. The SIBC is

Submitted On: Jan. 6, 2012
Accepted On: July 22, 2012

based in the analytical solution of the diffusion equation. In FE transformer modeling, the computational cost to obtain stray losses in regions with induced eddy currents is high. This is due to the equipment size and the large number of finite elements needed in the discretisation of the metallic parts. Hence, the Surface Impedance Boundary Condition (SIBC) represents an economic alternative for calculating these stray losses because it avoids the FE meshing of conducting parts. The FE literature recommends the usage of line elements to represent the conductive regions with the SIBC [9-11]. For this reason, the incorporation of the SIBC into a FE model presents two important advantages in its usage. Firstly the resulting model decreases the computational cost and secondly it can easily be implemented into a FE code.

Several researchers have applied the SIBC for calculating the stray losses in power transformers. Holland et al. used 3D FE and SIBC to analyze the tank-wall losses of a three-phase transformer [12]. Guerin et al. made a simulation of a three-phase transformer using the volume AV, shell AV and surface impedance formulations [13]. Guerin et al. also applied the non-linear surface impedance condition using a B-H rectangular curve known as Agarwal curve to simulate an 100 MVA three-phase transformer [14].

In addition, some papers have published the application of the SIBC in electrical motors and in the time domain. Adamiak et al. analyzed a low-speed linear induction motor using the 2D SIBC [15]. Yuferev et al. presented several high order generalized expressions of the SIBC, which were obtained by solving the diffusion equation using a perturbation technique [16]. Sabariego et al. developed a dual formulation of the time-domain SIBC both the magnetic field and magnetic vector potential [17]. Sabariego et al. also combined the SIBC in the time domain with a coarse volume FE discretisation of the massive conductors to capture the slowly varying flux components [18].

Futhermore, the SIBC has also been applied to high frequencies problems. Sakellaris et al. developed a SIBC formulation based in the magnetic vector potential, which was applied to a high frequency problem [19]. Darcherif et al. applied the SIBC to obtain the parameters of multiconductor and shielded cables at medium and high frequencies [20].

However, the above references show a lack of a clarity in the SIBC formulation, which does not help to its implementation into a FE code. A FE beginner will grasp easily a detailed step-by-step SIBC formulation such that can be incorporated into his FE code. This can be useful in those situations where the usage of commercial software is not available due to its high cost.

In this paper, a comprehensive SIBC 2D-FE linear formulation is presented. This formulation is expressed in terms of the magnetic vector potential. To illustrate the SIBC application, an axi-symmetric model of the transformer is solved. The loss intensity on the vertical tank-wall of the transformer is obtained using the Poynting's vector formulation. The SIBC model is compared against the results of a first order FE model of the transformer. The results obtained demonstrate the validity of using the SIBC for calculating the stray losses on the tank-wall of a transformer.

II. FINITE ELEMENT DISCRETISATION

The diffusion equation can be derived from the Maxwell's equations. It describes the behavior of the electromagnetic fields in the frequency domain and it is given by [9].

$$\nu\nabla^2 A = j\omega\sigma A - J_0, \tag{1}$$

where ω is the angular frequency, σ and ν are the conductivity and reluctivity of the material, respectively. A is the magnetic vector potential. J_0 is the imposed current density.

The FEM can be used to obtain the solution to the diffusion equation in 2D. By applying the Galerkin method, where the residual is multiplied by a weighted function and by using first-order FE, the solution of (1) is given by (2) [19]:

$$\frac{\nu}{4\Delta}[S][A] + \frac{j\omega\sigma\Delta}{12}[T][A] = \frac{J_0\Delta}{3}[I], \tag{2}$$

where the matrices S and T are given by:

$$[S] = \begin{bmatrix} b_1^2 + c_1^2 & b_1b_2 + c_1c_2 & b_1b_3 + c_1c_3 \\ b_1b_2 + c_1c_2 & b_2^2 + c_2^2 & b_2b_3 + c_2c_3 \\ b_1b_3 + c_1c_3 & b_2b_3 + c_2c_3 & b_3^2 + c_3^2 \end{bmatrix}, \tag{3}$$

$$[T] = \begin{bmatrix} 2 & 1 & 1 \\ 1 & 2 & 1 \\ 1 & 1 & 2 \end{bmatrix}, [I] = \begin{bmatrix} 1 \\ 1 \\ 1 \end{bmatrix}, [A] = \begin{bmatrix} A_1 \\ A_2 \\ A_3 \end{bmatrix}. \tag{4}$$

Where b_1, b_2, b_3, c_1, c_2 and c_3 are geometrical coefficients and Δ is the area of the element. A_1, A_2 and A_3 are the nodal potentials on the element.

The calculation of the loss intensity P of a first-order FE is given by (5), (6) and (7) [21]

$$P = \mathrm{Re}\left\{\frac{JJ^*}{2\sigma}\right\}, \tag{5}$$

$$J = \sigma E, \tag{6}$$

$$E = -j\omega\frac{\left(A_1 + A_2 + A_3\right)}{3}, \tag{7}$$

where J is the eddy current density in a triangular element, J^* is its complex conjugate and E is the electric field.

III. THE SIBC FORMULATION

The SIBC has its origin in the phenomena known as skin effect, where the flux density is concentrated at the surface of the conductive material. This effect can be found in regions characterized by high values of permeability, conductivity or frequency. The diffusion equation without the presence of current sources is given by (8),

$$\nabla\times(\nabla\times\mathbf{A}) = j\omega\mu\sigma\mathbf{A}, \tag{8}$$

where μ is the permeability of the material.

The one-dimension (1D) form of (8) can be written as

$$\frac{\partial^2 A}{\partial x^2} = j\omega\mu\sigma A, \tag{9}$$

its analytical solution is given by (10) [10], and the normal derivative of the magnetic vector potential is given by (11).

$$A = A_0 e^{-\gamma x}, \tag{10}$$

$$\frac{\partial A}{\partial x} = \frac{\partial A}{\partial n} = -\gamma A_0 e^{-\gamma x} = -\gamma A, \tag{11}$$

where A_0 is the magnetic vector potential of the separating surface. γ and the penetration depth δ are defined by (12) and (13), respectively.

$$\gamma = \frac{1+j}{\delta}, \tag{12}$$

$$\delta = \sqrt{\frac{2}{\omega\mu\sigma}}. \tag{13}$$

To implement the concept of SIBC into a FE formulation, the diffusion equation is solved using the neighbor region jointed to the boundary with eddy currents [20].

$$\nabla\times(v_1\nabla\times\mathbf{A}) = 0, \tag{14}$$

where v_1 is the reluctivity of the region without eddy currents.

By discretizing (14) with the FE Galerkin method and using the normal derivative (11) of the 1D analytical solution, the following result is obtained,

$$v_1\int_\Gamma N\frac{\partial A}{\partial n}\,d\Gamma = -v_2\gamma\int_\Gamma NA\,d\Gamma, \tag{15}$$

where v_2 is the reluctivity of the region with eddy currents and N stands for the shape function.

Taking into account the right hand side of (15) and the linear interpolation of the potentials within a finite element, the expression (16) can be obtained,

$$-v_2\gamma\int_\Gamma NA\,d\Gamma = -v_2\gamma\int_\Gamma [N^e]^T[N^e][A^e]\,d\Gamma, \tag{16}$$

where $[N^e]$ are the shape functions of the linear element and $[A^e]$ are the unknown nodal potentials, which are expressed by (17) and (18). T means matrix transpose.

$$[N^e] = [N_1 \quad N_2], \tag{17}$$

$$[A^e] = \begin{bmatrix} A_1 \\ A_2 \end{bmatrix}. \tag{18}$$

Therefore, the discretisation of (16) of a linear element is as follows,

$$-v_2\gamma\int_\Gamma NAd\Gamma = -v_2\gamma\int_\Gamma\begin{bmatrix} N_1^2 & N_1N_2 \\ N_1N_2 & N_2^2 \end{bmatrix}\begin{bmatrix} A_1 \\ A_2 \end{bmatrix}d\Gamma. \tag{19}$$

By using the definite integral given in (20), the values of the characteristic matrix are obtained,

$$\int_\Gamma N_1^a N_2^b\,d\Gamma = \frac{a!b!l}{(a+b+1)!}, \tag{20}$$

where l is the length of the linear element and it is given by:

$$l = \sqrt{\left(x_1 - x_2\right)^2 + \left(y_1 - y_2\right)^2}, \tag{21}$$

where x_1, x_2, y_1 and y_2 are their spatial coordinates.

Therefore, Eq. (19) can be written as

$$-v_2\gamma\int_\Gamma NA\,d\Gamma = -\frac{v_2\gamma l}{6}\begin{bmatrix} 2 & 1 \\ 1 & 2 \end{bmatrix}\begin{bmatrix} A_1 \\ A_2 \end{bmatrix}. \tag{22}$$

Consequently, by employing the SIBC, the elemental matrix (2) can be transformed into:

$$\frac{\nu_1}{4\Delta}[S][A]+\frac{j\omega\sigma_1\Delta}{12}[T][A] \\ +(1+j)\frac{\nu_2 l}{6\delta_s}[P][A]=\frac{J_0\Delta}{3}[I], \tag{23}$$

$$[P]=\begin{bmatrix}2 & 1 & 0\\ 1 & 2 & 0\\ 0 & 0 & 0\end{bmatrix}, \tag{24}$$

$$\delta_s=\sqrt{\frac{2\nu_2}{\omega\sigma_2}}. \tag{25}$$

Where σ_1 is the conductivity of the 2D region and σ_2 is the conductivity of the SIBC region.

The SIBC edge of the first-order FE is located between the first two local nodes, Fig. 1.

IV. APPLICATION OF THE SIBC TO A TRANSFORMER

This section presents the application of the SIBC for calculating the stray losses on the tank-wall of a transformer. The theory of Poynting's vector states that at the surface of good conductors the tangential components of the electric and magnetic fields are approximately proportional to each other. This is known as surface impedance [11].

The magnetic field intensity **H** within one FE is given by (26) [9]

$$\mathbf{H}=\nu_2\mathbf{B}=\nu_2\nabla\times\mathbf{u}_z A_0 e^{-\gamma x} \\ =\mathbf{u}_y\nu_2\gamma A_0 e^{-\gamma x}=\mathbf{u}_y\nu_2\gamma A, \tag{26}$$

and the electric field **E** is expressed as (27).

$$\mathbf{E}=-j\omega\mathbf{A}=-\mathbf{u}_z j\omega A_0 e^{-\gamma x}=-\mathbf{u}_z j\omega A. \tag{27}$$

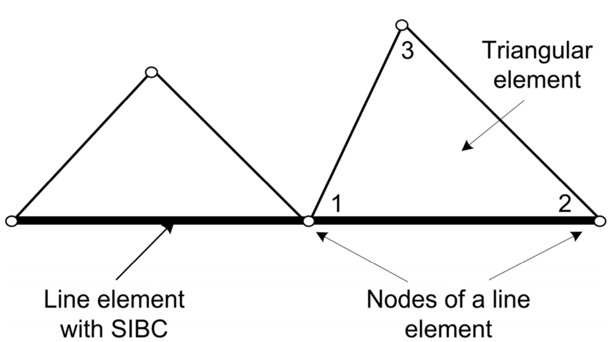

Fig. 1. Line element with SIBC between two first local nodes of a triangular element.

By employing (26) and (27), the surface impedance, Z_s, is obtained as (28).

$$Z_s=\frac{E_t}{H_t}=\frac{|\mathbf{E}|}{|\mathbf{H}|}=\frac{j\omega}{\nu_2\gamma}=\frac{\gamma}{\sigma_2}=\frac{(1+j)}{\sigma_2\delta_s}, \tag{28}$$

where E_t and H_t are the tangential components of the electric and magnetic fields, respectively.

Therefore the resulting equations for the post-processing of the solution are (29) and (30).

$$E_t=-j\omega\frac{(A_1+A_2)}{2}, \tag{29}$$

$$H_t=\frac{E_t\sigma_2\delta_s}{\sqrt{2}}. \tag{30}$$

The loss intensity P_e within a linear element is obtained by using the Poynting vector and it is given by (31).

$$P_e=\frac{1}{2}\mathrm{Re}(Z_s)|H_t|^2=\frac{1}{2}\frac{|H_t|^2}{\sigma_2\delta_s}. \tag{31}$$

The SIBC formulation is implemented in a C language program and the solver PARDISO is used to solve the resulting system of linear equations [22-23].

For a student, the demonstration of the validity of the SIBC formulation is illustrative. For this purpose, two FE meshes of the axi-symmetric model of the transformer (Fig. 2) are constructed. The loss intensity along the vertical tank-wall is calculated by employing two FE meshes. One mesh is generated using first-order FE to represent the tank-wall while the other mesh is created using line elements that represent the SIBC. The thickness of the tank-wall is 4.83 mm. The parameters of the transformer model are shown in Table 1 and the electrical frequency is 60 Hz. Therefore, the skin depth has a value of 1.2579 mm which is smaller than the thickness of the tank-wall. The FE meshes were generated using a free software library [24]. A computer with an Intel dual-core processor was used in the simulations. The mesh size and the computational time for each model are indicated in Table 2. It can be seen that by using the SIBC approach, the mesh size can be reduced by 57.44 % and the computational time can be decreased by 52.34 %.

The comparative results of eddy current losses by using the SIBC and FE used to represent the plate of transformer tank-wall are shown in Table 3.

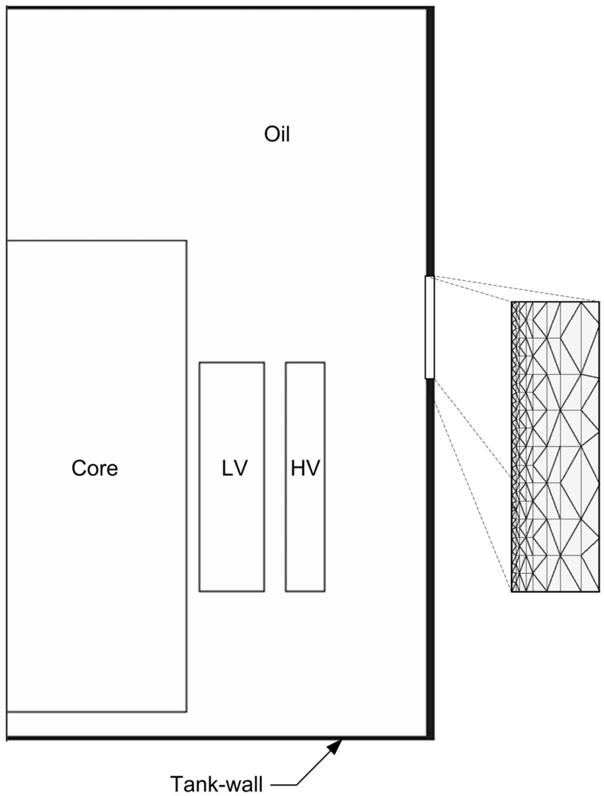

Fig. 2. Schematic diagram of the transformer FE model.

It can be seen that both results are almost of the same magnitude. This demonstrates the validity of the SIBC formulation. Table 3 also shows that losses are mainly concentrated in the vertical tank wall due to the small loss increment obtained in the total stray losses.

The flux distribution obtained with the model that uses first-order FE is shown in Fig. 3, whereas the solution obtained by using the SIBC formulation is illustrated in Fig. 4. It can be seen that both flux distributions are very similar.

In order to compare the loss intensity on the vertical tank-wall, it is firstly computed with a first-order FE mesh. A technique was developed to obtain this surface representation of loss intensity.
This technique is based on the linear distribution property of losses within a FE. Firstly, the total area of the vertical tank-wall is divided into equidistant rectangular regions. This allows the calculation of loss intensity by using the loss quantity allocated in each rectangular region. An interpolation technique was used to obtain the amount of the losses in the rectangular area.

Table 1: Parameters of the transformer model

Region	Current	Turns	μ_r	σ
LV	5552.3A	6.0	1.0	—
HV	53.56 A	622.0	1.0	—
Core	—	—	Non-linear (M4)	0.0 S
Oil	—	—	1.0	0.0 S
Tank	—	—	400.0	6.67e6 S

Thereafter, the losses of each rectangular region are divided along its vertical length (height). Since the problem is axi-symmetric, the losses are also divided by its cylindrical depth, $2\pi r$, where r is the radius of the tank-wall surface. To illustrate the above process, a mesh with six rectangular regions (shaded) is shown in Fig. 5. To complement the analysis presented in this paper, the magnetic nonlinearity of the tank-wall material is included in the FE model. The Newton-Raphson algorithm is employed to solve the resulting nonlinear equations. The A36 steel is used to represent the tank-wall. The loss intensity behavior in the transformer tank-wall is shown in Fig. 6. It can be observed that the nonlinear model underpredicts the loss intensity with respect to the linear FE and SIBC-FE models. This is a useful result for manufacturers because a linear solution can be used to approximately predict the eddy current losses. The rather small loss difference is due to the slightly saturation of the transformer plates since it is only excited by the magnetic leakage fluxes of the transformer windings.

Table 2: CPU time and mesh size for both models

Model	CPU time	Nodes
Linear FE	40.92 s	278,249
Linear SIBC-FE	21.42 s	160,018
Non-linear FE	253.81 s	278,249

Table 3: Computed stray losses of the transformer

Model	Vertical tank-wall losses	Total tank-wall losses
Linear FE	84.3245 W	86.9237 W
Linear SIBC-FE	84.5805 W	87.1889 W
Non-linear FE	77.5774 W	79.2268 W

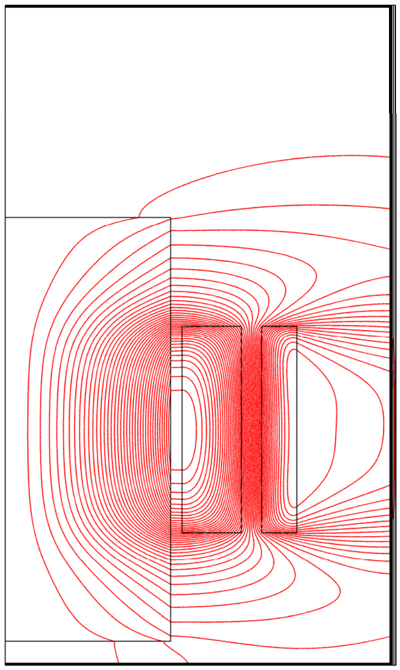

Fig. 3. Flux distribution in the FE linear model of the transformer.

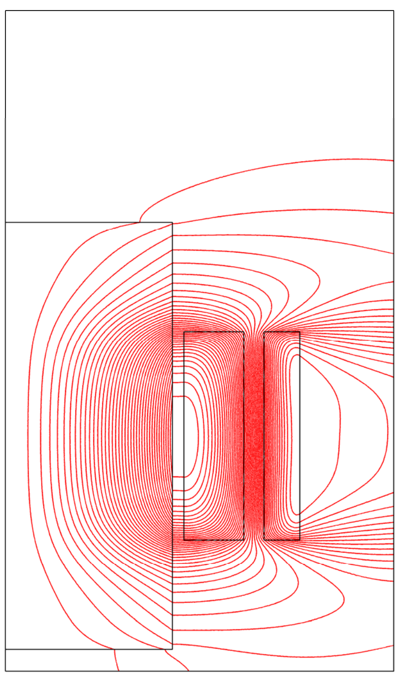

Fig. 4. Flux distribution in the SIBC-FE linear model.

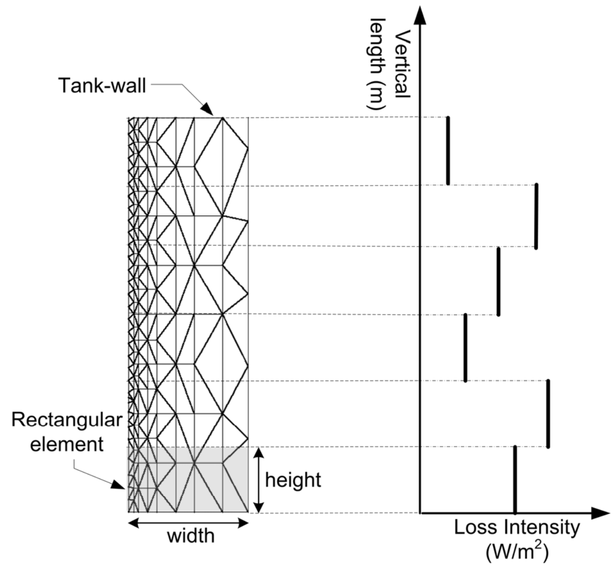

Fig. 5. Projection of the FE losses in the vertical tank-wall into an equivalent surface.

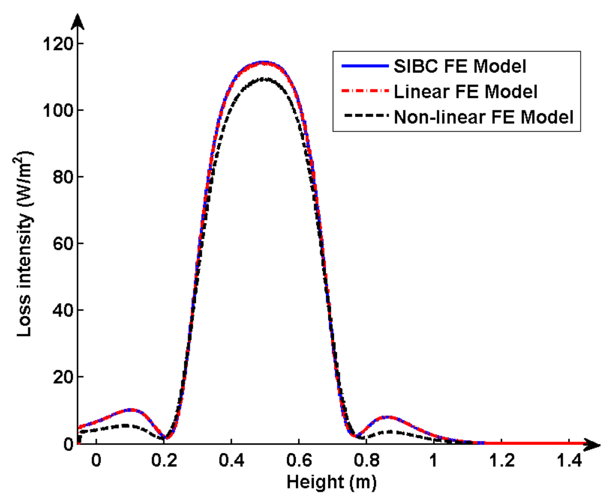

Fig. 6. Loss intensity behavior along the vertical tank-wall.

V. CONCLUSION

In this paper, a comprehensive FE-SIBC formulation has been presented and applied to the modeling of the transformer tank-wall. The formulation allows an easy understanding of the SIBC and its incorporation into a FE code. Besides, it was illustrated that this formulation has advantages in terms of computational time and mesh size, which makes it attractive for computing stray losses in large electrical equipment. An axi-symmetric FE model of the transformer was developed and the SIBC formulation was used to represent the tank-wall. In order to compare the results obtained by using the SIBC and FE models, a projection technique of the 2D-FE losses was developed. Finally, it was shown that the SIBC is a useful approach that can be used in conductive regions allowing to decrease the FE mesh size.

ACKNOWLEDGMENT

The authors would like to thank to CONACYT, PROMEP and DGEST for their financial support to carry out this work.

REFERENCES

[1] S. Savin, S. Ait-Amar, D. Roger, and G. Vélu, "Prospective method for partial discharge detection in large AC machines using magnetic sensors in low electric field zones," *Applied Computational Electromagnetics Society (ACES) Journal*, vol. 26, no. 9, pp. 729-736, September 2011.

[2] J. H. Alwash and L. J. Qaseer, "Three-dimension finite element analysis of a helical motion induction motor," *Applied Computational Electromagnetics Society (ACES) Journal*, vol. 25, no. 8, pp. 703-712, August 2010.

[3] E. Afjei and H. Torkaman, "Finite element analysis of switched reluctance generator fault condition oriented towards diagnosis of eccentricity fault," *Applied Computational Electromagnetics Society (ACES) Journal*, vol. 26, no. 1, pp. 8-16, January 2011.

[4] A. B. Ali, E. A. Hajlaoui, and A. Gharsallah, "Efficient analysis technique for modeling periodic structures based on finite element method using high-order multiscalets functions," *Applied Computational Electromagnetics Society (ACES) Journal*, vol. 25, no. 9, pp. 755-763, September 2011.

[5] T. Wan, R. Cheng, J. She, D. Ding, and Z. Fan, "An efficient finite-element time-domain method via hierarchical matrix algorithm for electromagnetic simulation", *Applied Computational Electromagnetics Society (ACES) Journal*, vol. 26, no. 7, pp. 584-595, July 2011.

[6] H. Torkaman, N. Arbab, H. Karim, and E. Afjei, "Fundamental and magnetic force analysis of an external rotor switched reluctance motor," *Applied Computational Electromagnetics Society (ACES) Journal*, vol. 26, no. 10, pp. 868-875, October 2011.

[7] S. V. Kulkarni and S. A. Khaparde, *Transformer Engineering Design and Practice*, Marcel Dekker, Inc. New York, 2004.

[8] S. Singh and M. N. Bandyopadhyay, "Dissolved gas analysis technique for incipient fault diagnosis in power transformers: A bibliographic survey," *IEEE Electrical Insulation Magazine*, vol. 26, no. 6, pp. 41-46, November/December 2010.

[9] S. R. H. Hoole, *Computer Aided Analysis Design of Electromagnetic Devices*, Elsevier, New York, 1989.

[10] K. J. Binns, P. J. Lawrenson, and C. W. Trowbridge, *The Analytical and Numerical Solution of Electric and Magnetic Fields*, John Wiley & Sons, London, 1994.

[11] S. V. Yuferev and N. Ida, *Surface Impedance Boundary Conditions: A Comprehensive Approach*, CRC Press, 2010.

[12] S. Holland, G. P. O'Connell, and L. Haydock, "Calculating stray losses in power transformers using surface impedance with finite elements," *IEEE Trans. on Magnetics*, vol. 28, no. 2, pp. 1355-1358, March 1992.

[13] C. Guerin, G. Tanneau, and G. Meunier, "3D eddy current losses calculation in transformer tanks using the finite element method," *IEEE Trans. on Magnetics*, vol. 29, no. 2, pp. 1419-1422, March 1993.

[14] C. Guerin and G. Meunier, "Surface impedance for 3D non-linear eddy current problem - application to loss computation in transformers," *IEEE Trans. on Magnetics*, vol. 32, no. 3, pp. 808-811, May 1996.

[15] K. Adamiak, G. E. Dawson, and A. R. Eastham, "Application of impedance boundary conditions in finite element analysis of linear motors," *IEEE Trans. on Magnetics*, vol. 27, no. 6, Part: 2, pp. 5193-5195, November 1991.

[16] S. Yuferev and L. Di Rienzo, "Surface-impedance boundary conditions in terms of various formalisms," *IEEE Trans. on Magnetics*, vol. 46, no. 9, pp. 3617-3628, September 2010.

[17] R. V. Sabariego, P. Dular, C. Geuzaine, and J. Gyselinck, "Surface-impedance boundary conditions in dual time-domain finite-element formulations," *IEEE Trans. on Magnetics*, vol. 46, no. 8, pp. 3524-3531, August 2010.

[18] R. V. Sabariego, C. Geuzaine, P. Dular, and J. Gyselinck, "Time-domain surface impedance boundary conditions enhanced by coarse volume finite-element discretisation," *IEEE Trans. on Magnetics*, vol. 48, no. 2, pp. 631-634, February 2012.

[19] J. Sakellaris, G. Meunier, A. Raizer, and A. Darcherif, "The impedance boundary condition applied to the finite element method using the magnetic vector potential as state variable: a rigorous solution for high frequency axisymmetric

problems," *IEEE Trans. on Magnetics*, vol. 28, no. 2, pp. 1643-1646, March 1992.

[20] A. Darcherif, A. Raizer, J. Sakellaris, and G. Meunier, "On the use of the surface impedance concept in shielded and multiconductor cable characterization by the finite element method," *IEEE Trans. on Magnetics*, vol. 28, no. 2, pp. 1446-1449, March 1992.

[21] S. J. Salon, *Finite Element Analysis of Electrical Machines*, Springer, 1995.

[22] O. Schenk and K. Gartner, "Solving unsymmetric sparse systems of linear equations with PARDISO," *Journal of Future Generation Computer Systems*, vol. 20, pp. 475-487, 2004.

[23] O. Schenk and K. Gartner, "On fast factorization pivoting methods for symmetric indefinite systems," *Elec. Trans. Numer. Anal.*, vol. 23, pp. 158-179, 2006.

[24] J. R. Shewchuk, "Triangle: engineering a 2D quality mesh generator and Delaunay triangulator," *Applied Computational Geometry: Towards Geometric Engineering*, *Lectures notes in Computer Science,* Springer-Verlag Berlin*,* vol. 1148, pp. 203-222, May 1996.

J. M. Díaz-Chacón received the B.Sc. degree in electronic engineering in 2006 and M.Sc. degree in electrical engineering in 2010 from the Instituto Tecnológico de la Laguna, Torreón, México. He is currently working toward his doctoral degree in electrical engineering at the Instituto Tecnológico de la Laguna. His research interests include numerical methods applied to analysis of electrical machines.

C. Hernandez received the B.Sc. degree in computer science from the Instituto Tecnológico de Estudios Superiores de Monterrey, Monterrey, México, in 1990, the M.Sc. degree in foundations of advanced information technology from Imperial College, London, U.K., in 1995, and the Sc.D. degree in electrical engineering from the Instituto Tecnológico de la Laguna, Torreón, México, in 2007. She was with the Simulation Department, Instituto de Investigaciones Eléctricas from 1991 to 2000. She is currently with the Instituto Tecnológico de la Laguna, Torreón, México. Her interests are in artificial intelligence and global optimization applied to electrical machines.

M. A. Arjona received the B.Sc. degree in electrical engineering from the Instituto Tecnológico de Durango, Durango, México, in 1988, the M.Sc. degree in electrical engineering from the Instituto Tecnológico de la Laguna, Torreón, México, in 1990, and the Ph.D. degree in electrical engineering from Imperial College, London, U.K., in 1996.

He was with the Simulation Department, Instituto de Investigaciones Eléctricas from 1991 to 1999. He is currently a Professor of electrical machines with the Instituto Tecnológico de la Laguna. His interests are in the electromagnetic design, analysis, and control of electrical machines.

A Novel Compact Monopole Antenna with Triple High Quality Rejected Bands for UWB Applications

Zhi-Li Zhou, Li Li, and Jing-Song Hong

Institute of Applied Physics
University of Electronic Science and Technology, Chengdu, 610054, China
zhouzhili003@163.com, liliangirl@126.com, cemlab@uestc.edu.cn

Abstract ─ A novel compact ultra-wideband (UWB) monopole antenna with triple high quality notch bands is presented. By attaching a T-shaped strip to the semicircular patch on the front side and adding a rectangular ring on the back side, a notch band for WiMAX is obtained. Furthermore, by symmetrically etching a pair of curved slots and a pair of L-shaped slots in the radiation patch, band rejected filtering properties in the lower WLAN band and upper WLAN band are also achieved. Experimental results show that the designed antenna, with compact size of $24\times28\text{mm}^2$ has an impedance bandwidth of 2.75GHz-14.7GHz for VSWR<2, except three frequency stop bands of 3.3GHz-3.75GHz, 4.77GHz-5.4GHz,and 5.7GHz-6.23GHz. Moreover, good omnidirectional radiation patterns in the H-plane are also obtained.

Index Terms ─ Compact, monopole antenna, rejected bands, UWB applications.

I. INTRODUCTION

Ultra-wideband (UWB) technology has undergone many significant developments in recent years [1-2]. However, there still remain many challenges in making this technology alive up to its full potential [3-4]. Planar monopole antennas have been found to be excellent candidates to operate in UWB systems, owing to wide bandwidth, simple structure and omnidirectional radiation patterns [5]. However, over the UWB frequency band ranging from 3.1GHz to 10.6GHz, other frequency bands exist such as WiMAX band (3.3GHz-3.7GHz), and WLAN band (5.15GHz-5.35GHz, 5.725GHz-5.825GHz). Therefore, many band notched technologies [6-9] have been reported such as etching a pair of asymmetrical spurlines on the feedline [10], embedding a pair of Γ-shaped stubs in the patch and G-slot on the ground plane [11]. Nevertheless, all these antennas have only two notch bands and especially have only one notch band for WLAN in 5.15GHz-5.825GHz. This reveals that potential interference from other narrow bands may still exist and the frequency range between 5.35GHz-5.725GHz cannot be utilized with these antennas.

In this paper, a novel compact monopole UWB antenna with three independent notch bands is presented. By attaching a T-shaped strip to the semicircular patch on the front side and adding a rectangular ring on the back side, a notch band of 3.3GHz-3.7GHz is achieved. To realize another two narrow bands of WLAN centered at 5.2GHz and 5.8GHz, a pair of curved slots and a pair of L-shaped slots are etched in the patch symmetrically. Details of this antenna are presented and the measured results are given to demonstrate its performance.

II. ANTENNA DESIGN

Fig. 1(a) and (b) show the geometry of the proposed band notched antenna, which is fabricated on a FR4 substrate of thickness 1.6mm and permittivity 4.5. The width of the feeding line is fixed at 3.2mm to achieve 50Ω characteristic impedance (at the centre frequency). The proposed compact band notched antenna is based on a simple circular monopole antenna. The notches defected on the ground plane is designed to achieve better impedance matching over the entire UWB frequency band, because the modified truncation creates a capacitive load that neutralizes the inductive nature of the patch to produce nearly pure resistive input impedance. To realize the

Submitted On: Nov. 27, 2011
Accepted On: July 22, 2012

notch band for WiMAX band, a T-shaped strip was connected to the semicircular patch on the front side and a rectangular ring was added on the back side. Therefore, an extra resonator was constructed. Adjusting the related dimensions to make it resonates at the desired notch frequency (3.5GHz). Because of the symmetrical characteristics of such resonator, the fields yielded by the currents concentrated in the resonator cancel each other. As a result, a steep rejection property is achieved.

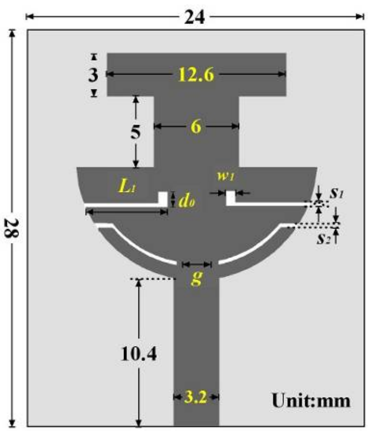

(a)Front view

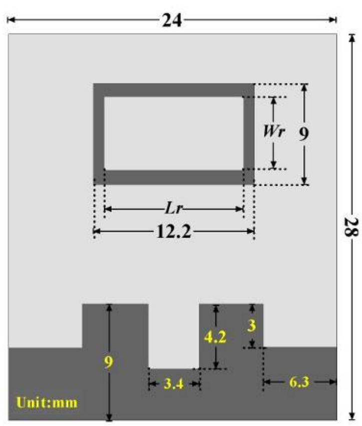

(b)Back view

Fig. 1. Geometry of the proposed band notched antenna: (a) front view. (b) back view.

Similarly, the second notch band for lower WLAN band (5.15GHz-5.35GHz) comes from the pair of L-shaped slots on the patch and the third rejection band for upper WLAN band (5.725GHz-5.825GHz) is attributed to the two curved slots on the patch.

III. RESULATS AND DISCUSSION

The proposed compact monopole antenna with triple high quality rejected bands is constructed, and the numerical and experimental results are presented and discussed. The parameters of this proposed antenna are studied by changing one parameter at a time and fixing the others. To fully understand the behavior of the antenna's structure and to determine the optimum parameters, the antenna was analyzed using the commercial software CST. And a photograph of some fabricated prototypes with optimal design, i.e. d_0=1mm, L_1=5.9mm, d=0.8mm, s_1=0.1mm, s_2=0.2mm, w_1=0.7mm, L_r=10.8mm, W_r=7.4mm, is shown in Fig. 2.

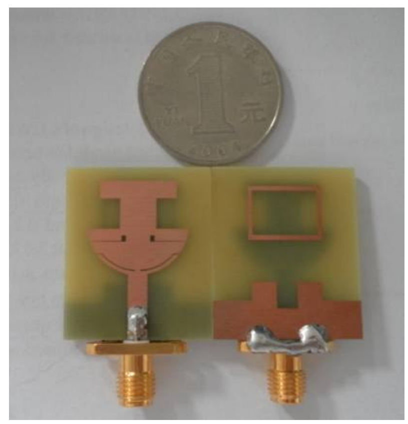

Fig. 2. Prototype of the proposed band notched antenna.

In order to minimize the physical size of the proposed antenna, the upper half circular patch was cut first and then a T shaped strip is attached to the lower half circular patch. As a result, the maximum equivalent electrical length is effectively lengthened thus compact size can be achieved. Furthermore, by adding a rectangular ring on the back, a notch band is achieved. Fig. 3 exhibits the effects of the rectangular ring to the performance of the proposed antenna. And from the results it can be observed that the inner length of the rectangular L_r have only impact on the first notch band. With the parameter L_r decreases from 11.6mm to 10.0mm gradually, the first rejected band shifts right correspondingly, while the other two rejected bands almost remain still.

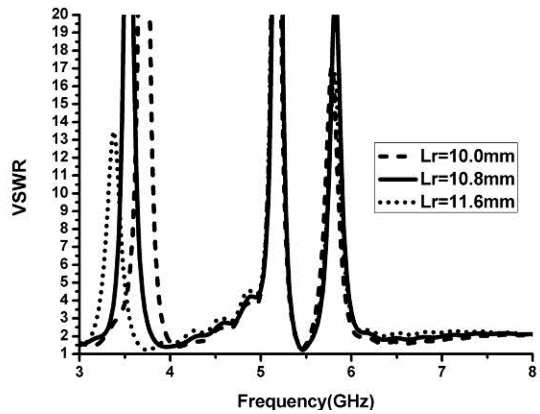

Fig. 3. Simulated VSWRs for the proposed antenna with different length of *Lr*.

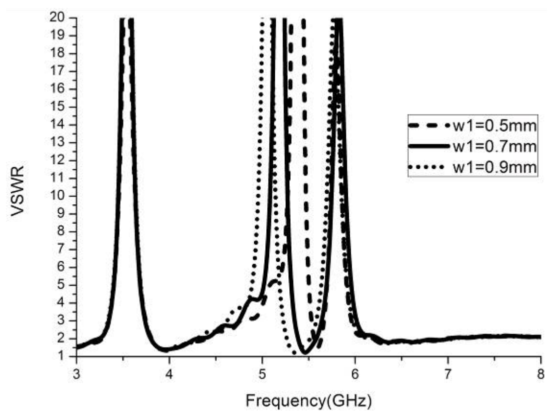

Fig. 4. Simulated VSWRs for various width w_1.

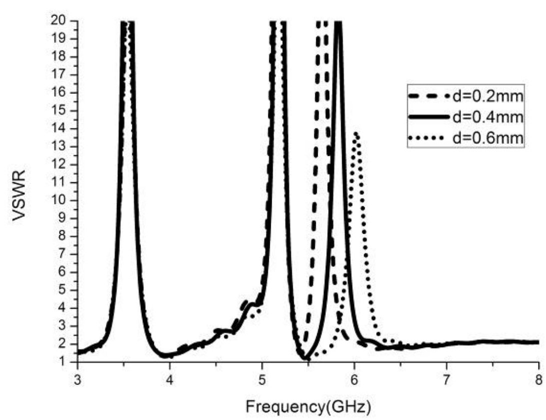

Fig. 5. Simulated VSWRs for various distances *d*.

Moreover, the VSWRs for various width w_1 are plotted in Fig. 4. It can be observed that the parameter w_1 has only great impact on the second notch band. And with 'w_1' increases from 0.5mm to 0.9mm, the second notch band shift left gradually. Similarly, the parameter *d* mostly affects the third notched band alone, as shown in Fig. 5. And with d_1 increase from 0.2mm to 0.6mm, the third rejected band shifts right while the other two notch bands stand still.

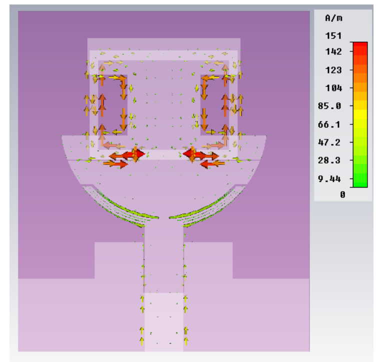

(a) At 3.5GHz

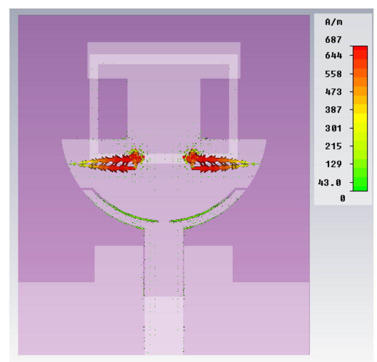

(b) At 5.2GHz

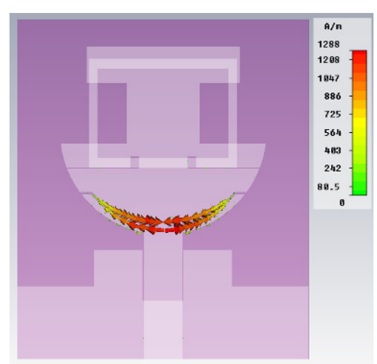

(c) At 5.8GHz

Fig. 6. The current distribution at different frequencies: (a) at 3.5GHz. (b) at 5.2GHz. (c) at 5.8GHz.

The simulated current distribution of the proposed antenna at 3.5GHz, 5.2GHz, and 5.8GHz for the optimal design is presented in Fig. 6 (a), (b) and (c), respectively. It can be seen that the current at the notch frequencies are symmetrically distributed. Accordingly the radiation fields generated by the oppositely directed currents cancel each other at the notch frequencies. Thus notch bands are obtained. Furthermore, the current is mainly distributed along the T-shaped strip and the rectangular ring at 3.5GHz, and distributed along the edge of the L-shaped slots at 5.2GHz. While at 5.8GHz the current is mostly exists along the curved slots. As a result, the three notch bands are independent adjustable, which is very convenient when it comes to specific application.

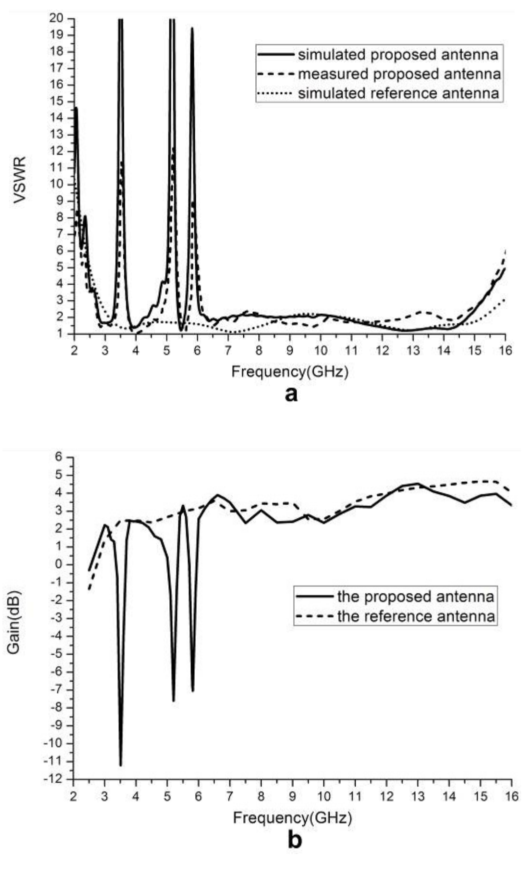

Fig. 7. (a) Simulated and measured VSWR for the proposed antenna. (b) The antenna gain of the proposed antenna and the reference antenna.

The simulated and measured VSWR of the proposed band notched UWB antenna is shown in Fig. 7 (a). Furthermore, the simulated VSWR of the UWB antenna without notched characteristics (the traditional circular monopole antenna) is also shown for comparison. It can be observed that the designed antenna has wideband performance of 3GHz-15GHz for VSWR<2, except three steep rejection bands of 3.3GHz-3.75GHz, 4.77GHz-5.4GHz, and 5.7GHz-6.23GHz. And the realized gain showed in Fig. 7 (b) exhibits three sharp gain decreases at 3.3GHz-3.75GHz, 4.77GHz-5.4GHz, and 5.7GHz-6.23GHz. Particularly, compared with other band notched antennas, the proposed antenna with VSWRs>19 at all the three notch bands demonstrates even much better rejection characteristics. Furthermore, the frequency range between 5.4GHz-5.7GHz can be utilized with the proposed antenna, which is rejected by other WLAN band notched antennas. Figure 8 shows the radiation patterns of the proposed antenna at 3.1GHz, 5.4GHz, and 7.5GHz, respectively. It can be seen that the proposed antenna exhibits a fairly good omnidirectional radiation pattern in the H-plane and a dipole-like radiation pattern in the E-plane.

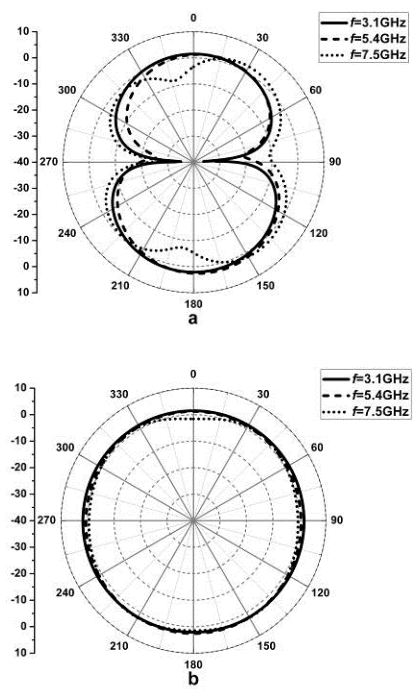

Fig. 8. The radiation patterns of the proposed antenna: (a) E plane. (b) H plane.

Furthermore, as a very important aspect of a practical antenna, the efficiency of the proposed antenna is also investigated. The simulated efficiency of the proposed band notched antenna is shown in Fig. 9. And the efficiency of the reference UWB antenna is also shown for comparison. It can be observed that the efficiency of the reference UWB antenna without notched characteristics is mostly above 80% in the operation band. However, the efficiency of the proposed band notched antenna is not more than 10% in the three notch bands, while almost remain the same in the operation band.

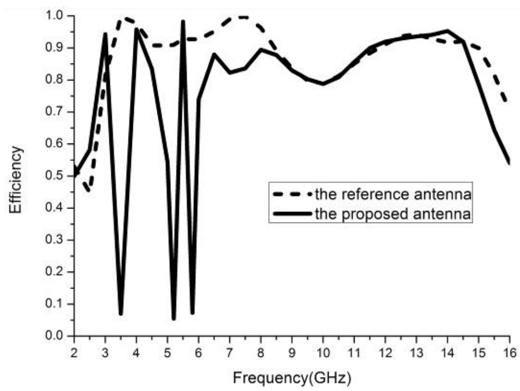

Fig. 9. The efficiency of the proposed antenna and the reference antenna.

IV. CONCLUSION

A novel compact UWB printed monopole antenna with triple high quality rejected bands has been presented. The notch bands are realized by attaching a T-shaped strip to the semicircular patch on the front side and adding a rectangular ring on the back side, etching a pair of L-shaped slots and a pair of curved slots in the radiation patch. Both wide bandwidth and good monopole-like radiation patterns are obtained. The proposed antenna's features such as sufficient and independent adjustable band notches, higher rejection peak, wide bandwidth, and omnidirectional radiation patterns, show that the proposed antenna is a very good candidate for UWB applications.

ACKNOWLEDGMENT

This work was supported partially by the National Science Foundation of China (No.60872029 and No.60872034), partially by the High-Tech Research and Development Program of China (No.2008AA01Z206), partially by the Aeronautics Foundation of China (No.2010018003), and partially by the Fundamental Research Founds for the Central Universities (No.ZYGX 2009J037).

REFERENCES

[1] R. Azim, M. T. Islam, N. Misran, 'Design of a planar UWB antenna with new band enhancement technique,' *The Applied Computational Electromagnetics Society (ACES) Journal*, vol. 26, no. 10, pp. 856-862, October 2011.

[2] D. S. Javan, O. H. Ghouchani, 'Cross slot antenna with U-shaped tuning stub for ultra wideband applications,' *The Applied Computational Electromagnetics Society (ACES) Journal*, vol. 24, no. 4, pp. 427-432, August 2009.

[3] H.Schantz, The Art and Science of Ultra Wideband Antennas. Norwood, MA: Artech House, 2005.

[4] Chung. K, Kim. J, Choi. J: 'Wideband microstrip-fed monopole antenna having frequency band-notch function', *IEEE Microw.Wirel.Compon.Lett.*, 15, pp. 766–768, 2005.

[5] M. N.-Jahromi, N. K.-Barchloui, 'Analysis of the behavior of Sierpinski carpet monopole antenna,' *The Applied Computational Electromagnetics Society (ACES) Journal*, vol. 24, no. 1, pp. 32-36, February 2009.

[6] J. William, R. Nakkeeran, 'A new UWB slot antenna with rejection of WiMax and WLAN bands,' *The Applied Computational Electromagnetics Society (ACES) Journal*, vol. 25, no. 9, pp. 787-793, September 2010.

[7] M. Mighani, M. Akbari, N. Felegari, 'A CPW dual band notched UWB antenna,' *The Applied Computational Electromagnetics Society (ACES) Journal*, vol. 27, no. 4, pp. 352-359, April 2012.

[8] Wu. Q, Jin. R, Ding. M: 'Printed omnidirectional UWB monopole antenna with very compact size', *IEEE Trans. Antennas Propag.*, 56(3), pp. 896-899, 2008.

[9] Movahedinia. R, Azarmanesh. M.N, 'Ultra-wideband band-notched printed monopole antenna' *IET Microw.Antennas Propagate.*, 4(12), pp. 2179-2186, 2010.

[10] Y.H. Zhao, J.P. Xu and K. Yin, 'Dual band notched ultra wideband microstrip antenna using asymmetrical spurlines', *Electron. Lett.*, 44, pp. 1051-1052, 2008.

[11] M. Abdollahvand, G. Dadashzadeh, and D. Mostafa, 'Compact dual band notched printed monopole antenna for UWB application', *IEEE Antenna and wireless propagation letters*, 9, pp. 1148-1151, 2010.

Zhi-Li. Zhou was born in Chongqing, China. He received his B.S. degree in electronics information and engineering from Sichuan University, China, in 2009. He is now working toward his M.S. degree in Radio Physics from the University of Electronic Science and Technology of China (UESTC).His research interests include antennas for wireless communication and microwave power transmission.

Li. Li was born in Meishan, China. She received her B.S. degree in physics from Leshan Normal University in 2009. She is now a graduate student major in Radio Physics in University of Electronic Science and Technology of China (UESTC). Her interests include antenna technology and wireless communication technology.

Jing-Song. Hong received the B.S. degree in electromagnetic from Lanzhou University, China, in 1991, and the M.S. and Ph. D. degrees in electrical engineering from the University of Electronic Science and Technology of China (UESTC), in 2000 and 2005, respectively. He is now a professor with UESTC. His research interest includes the use of numerical techniques in electromagnetic and the use of microwave methods for materials characterization and processing.

Analysis of Electromagnetic Scattering Problems by Means of a VSIE-ODDM-MLFMA Method

Jialin Chen [1], Shangsheng Li [1] and Yaping Song[2]

[1] Department of Electronic and Communication Engineering
Naval Aeronautical Engineering Institute
Yantai, P. R. China, 264001
cjl21806780@163.com

[2] The 91919th Unit of PLA,
Huanggang, P. R. China, 438021

Abstract ─ The hybrid volume-surface integral equation (VSIE) method has the advantage of solving electromagnetic scattering problems involving complex structure mixed metal with dielectric. In this paper, a method combining VSIE with overlapped domain decomposition method (ODDM) is used to analyze electromagnetic scattering problems successfully. To further improve efficiency, the multilevel fast multipole algorithm (MLFMA) is adopted, then a novel VSIE-ODDM-MLFMA is proposed. Numerical results show that the proposed method has low memory requirement, fast convergence, and accurate simulation result. It indicates that the proposed method has the ability to analyze complicated electromagnetic problems.

Index Terms ─ volume-surface integral equation, electromagnetic scattering, overlapped domain decomposition method, multilevel fast multipole algorithm.

I. INTRODUCTION

The solution of the hybrid volume-surface integral equation (VSIE) is based on the method of moments (MoM) which has been widely used for numerical analysis of electromagnetic radiation and scattering problems [1-3]. For direct solver, the memory requirement is $O(N^2)$ and the CPU time is $O(N^3)$ in MoM. However, both of them in MoM are $O(N^2)$ for iterative solvers, where N denotes the number of unknowns. For the electrically large problems, it is difficult to fulfill the requirement of memory and efficiency on single personal computer presently. The overlapped domain decomposition method (ODDM) has the function of decomposing the computed domain into several subdomains. Each subdomain is extended with a buffer domain. The solution of the whole domain could be completed by solving the extended subdomains circularly. Due to introducing buffer domain, the current edge-effect in each subdomain could be depressed effectively and the convergence of the outer iteration is much fast. For solving only one subdomain at a time, the ODDM has the advantage of saving computing resources. The fast multipole method (FMM) can accelerate the matrix vector product with complexity of $O(N^{1.5})$ and its extension, the multilevel fast multipole algorithm (MLFMA) [4-7], further reduces the complexity to $O(N\log N)$ [8]. In this paper, a new VSIE-ODDM-MLFMA is proposed which combines both ODDM and MLFMA with VSIE. Numerical results show the accuracy and efficiency of the proposed method. It demonstrates that the proposed method has the ability to analyze complicated electromagnetic problems.

II. FORMULATION

The section presents the VSIE-ODDM-MLFMA solver and its computational complexity analysis.

Submitted On: Nov. 30, 2011
Accepted On: July 30, 2012

A. Outline of the VSIE

Using the equivalence principle, the conducting bodies are replaced by equivalent surface currents and the dielectric materials are replaced by equivalent volume currents [9]. Above is the basic idea of the VSIE [10-11] method.

For the electromagnetic scattering problems involving complex structure mixed metal with dielectric, the integral equations can be expressed by mathematical relationship with corresponding magnetic vector and electric scalar potentials. As follows, the volume integral equation (VIE) and the surface integral equation (SIE) are given by

$$\mathbf{E}^i = \frac{\mathbf{D}}{\hat{\varepsilon}(\mathbf{r})} + j\omega\mathbf{A}_V(\mathbf{r}) + \nabla\Phi_V(\mathbf{r}) + j\omega\mathbf{A}_S(\mathbf{r}) + \nabla\Phi_S(\mathbf{r}) \quad \mathbf{r}\in V, \tag{1}$$

and

$$\mathbf{E}^i{}_{\tan} = [j\omega\mathbf{A}_V(\mathbf{r}) + \nabla\Phi_V(\mathbf{r}) + j\omega\mathbf{A}_S(\mathbf{r}) + \nabla\Phi_S(\mathbf{r})]_{\tan} \quad \mathbf{r}\in S \tag{2}$$

where $\hat{\varepsilon}(\mathbf{r})$ is the permittivity of the dielectric material, $\mathbf{A}_V(\mathbf{r})$, $\mathbf{A}_S(\mathbf{r})$, $\Phi_V(\mathbf{r})$, and $\Phi_S(\mathbf{r})$ are vector and scalar potentials produced by the volume and surface current, respectively, given by

$$\mathbf{A}_u(\mathbf{r}) = \mu_0\int_u \mathbf{J}_u(\mathbf{r}')g(\mathbf{r},\mathbf{r}')du' \quad u=S,V \tag{3}$$

$$\Phi_u(\mathbf{r}) = -\frac{1}{j\omega\varepsilon_0}\int_u \nabla\cdot\mathbf{J}_u(\mathbf{r}')g(\mathbf{r},\mathbf{r}')du' \quad u=S,V. \tag{4}$$

In (3) and (4), $g(\mathbf{r},\mathbf{r}') = \frac{e^{-jk_0|\mathbf{r}-\mathbf{r}'|}}{4\pi|\mathbf{r}-\mathbf{r}'|}$, the Green's function of free space, $\mathbf{J}_S$ is the surface current, $\mathbf{J}_V$ is the volume current which is related to the total electric flux density $\mathbf{D}$ in equation (1).

To solve the equations (1) and (2), the conducting surface is discretized into small triangular patches, while the dielectric region is divided into tetrahedral elements [9]. Employing both the Schaubert-Wilton-Glisson (SWG) [12] and the Rao-Wilton-Glisson (RWG) [1] basis functions in equations (1) and (2), then testing (1) with SWG basis function and testing (2) with RWG basis function, we can get a matrix equation which could be written as a submatrix form in the following:

$$\begin{bmatrix} Z^{DD} & Z^{DM} \\ Z^{MD} & Z^{MM} \end{bmatrix}\begin{bmatrix} I_{Dn} \\ I_{Mn} \end{bmatrix} = \begin{bmatrix} E^D \\ E^M \end{bmatrix}, \tag{5}$$

where the first matrix is impedance matrix, I_{Dn} and I_{Mn} are the unknown expansion coefficients, E^D and E^M denote the excitation vectors. The more details of the VSIE can be found in [9].

B. Basic principle of ODDM

When decomposing the whole computed domain to several subdomains, the corresponding impedance matrix $[Z]$ will be decomposed into several submatrices. The solution of the whole domain could be got by solving submatrix equations circularly. Above-mentioned process is the idea basis of domain decomposition method (DDM) [13]. For solving only one submatrix equation at a time, the memory requirement can be reduced. However, as the whole matrix equation need to be solved by iterative solvers, the computing time would become longer usually. Using parallel computation could improve efficiency. Similarly, employing preconditioned techniques can reduce iteration number and CPU time.

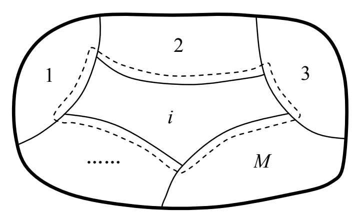

Fig. 1. The illustration of the DDM model.

As is shown in figure 1, if the domain is decomposed along the thin solid lines, there would be no common elements among the submatrices. In this way, the electric current of subdomain boundary would have singularity which can lead to the problem of low efficiency and slow convergence, even no convergence. In order to restrain electric current singularity, Brennan proposed a forward and backward buffer region (FBBR) iterative scheme which regards the forward or backward domain of subdomain boundary as buffer domain of the subdomain [14]. However, only the current edge-effect in one side of each subdomain is depressed. On the basis of the idea presented in [14], the ODDM was proposed in [15]. The dotted line in Figure 1 is the boundary of the extended subdomain whose solution is restricted to the original subdomain by discarding the currents in buffer domain. The whole domain current could be got by solving circularly. Above paragraph has illustrated the basic principle of ODDM.

The ODDM involves twofold iterations including inner iteration and outer iteration. The iteration solving subdomain is inner iteration while the process of solving all the subdomains once is called as an outer iteration, in which the current in the whole domain is updated once by the inner iteration. The following figure has explained the relation between inner iteration and outer iteration.

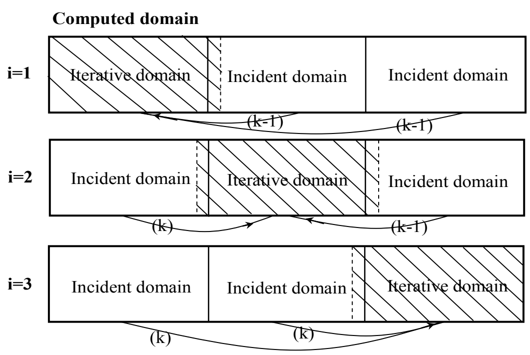

Fig. 2. The relation between inner iteration and outer iteration.

In figure 2, the iterative domain denotes the extended subdomain that need to be computed and its complementary domain is the corresponding incident domain, the thin solid line is subdomain boundary, the dotted line is the boundary of the extended subdomain with buffer domain, i represents the sequence number of the solved subdomain and k denotes kth outer iteration.

C. FMM and MLFMA

Based on FMM, the MLFMA has gained great success in solving electromagnetic problems with electrically large size [16-17]. MLFMA is the promotion of FMM in hierarchical structure. The basic principle of FMM is to divide scattering units which derived by discretizing scattering object into groups. The mutual coupling of any two scattering units is calculated by different methods according to the relative position of their groups. When they are adjacent, we use direct calculation method, otherwise, separate into three steps containing aggregation, translation and disaggregation. As shown in Fig.3, for a given group of field point, firstly, the contributions of all scattering units in its non-adjacent group would be aggregated to the center of each group, secondly, the contributions of these groups would be translated from each center to the center of the given group, finally, all the contributions of the non-adjacent groups would be disaggregated from the center of the given group to each scattering unit in the group. For a group of source point, the group center represents the contributions of all scattering units in this group to its non-adjacent groups. For a group of field point, the group center represents the contributions of all non-adjacent groups to this group. In this way, the number of scattering center is considerably reduced [18-19].

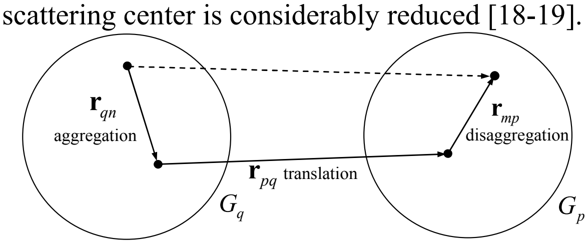

Fig. 3. The direct interaction between two far-field elements is separated into three steps containing aggregation, translation and disaggregation.

The expression for matrix vector product in FMM is written as

$$\sum_{n=1}^{N} Z_{mn} I_n = \sum_{q\in B_p} \sum_{n\in G_q} Z_{mn} I_n$$
$$+\oiint \mathbf{R}_{mp}(\hat{k}) \cdot \sum_{q\notin B_p} \Gamma_{pq}(\mathbf{k}, \hat{r}_{pq}) \sum_{n\in G_q} \mathbf{F}_{qn}(\hat{k}) I_n d^2\hat{k}. \quad (6)$$

The first term in (6) denotes the contribution from nearby groups (including the self-group) which is represented by the symbol B_p, the second term is the far-field interaction calculated by FMM, the $\mathbf{F}_{qn}(\hat{k})$, $\Gamma_{pq}(\mathbf{k}, \hat{r}_{pq})$, and $\mathbf{R}_{mp}(\hat{k})$ donate the aggregation, translation, and disaggregation factor, respectively.

D. The VSIE method combined with ODDM

As is shown in (3) and (4), using the volume current $\mathbf{J}_V$ and surface current $\mathbf{J}_S$ to respectively denote magnetic vector and electric scalar potentials in equation (1) and equation (2), we get the incident field expression. To derive the formulation of VSIE-ODDM conveniently, we define one F linear operator as

$$F_u(\mathbf{J}_u(\mathbf{r}')) = j\omega\mu_0 \int_u \mathbf{J}_u(\mathbf{r}') g(\mathbf{r},\mathbf{r}') du' - \frac{\nabla}{j\omega\varepsilon_0} \int_u \nabla \cdot \mathbf{J}_u(\mathbf{r}') g(\mathbf{r},\mathbf{r}') du' \quad u = S, V. \quad (7)$$

Then the equation (1) and equation (2) could be expressed as

$$\mathbf{E}^i = \frac{\mathbf{D}(\mathbf{J}_V(\mathbf{r}))}{\hat{\varepsilon}(\mathbf{r})} + F_V(\mathbf{J}_V(\mathbf{r}')) + F_S(\mathbf{J}_S(\mathbf{r}')) \quad \mathbf{r} \in V, \quad (8)$$

$$\mathbf{E}^i_{\tan} = [F_V(\mathbf{J}_V(\mathbf{r}')) + F_S(\mathbf{J}_S(\mathbf{r}'))]_{\tan} \quad \mathbf{r} \in S. \quad (9)$$

To build the integral iteration formula between subdomains, we define two linear operators $T^D(\mathbf{r},\mathbf{J})$ and $K^D(\mathbf{r},\mathbf{J})$ for the VIE (8). The two linear operators can be written as

$$T^D(\mathbf{r},\mathbf{J}) = \frac{\mathbf{D}(\mathbf{J}_V(\mathbf{r}))}{\hat{\varepsilon}(\mathbf{r})} + F_V(\mathbf{J}_V(\mathbf{r}')) + F_S(\mathbf{J}_S(\mathbf{r}')) \quad \mathbf{r}' \in \Omega_i', \mathbf{r} \in V_i' \quad (10)$$

$$K^D(\mathbf{r},\mathbf{J}) = F_V(\mathbf{J}_V(\mathbf{r}')) + F_S(\mathbf{J}_S(\mathbf{r}')) \quad \mathbf{r}' \in \bar{\Omega}_i', \mathbf{r} \in V_i' \quad (11)$$

where i is the sequence number of subdomain, the ith extended subdomain Ω_i' includes V_i' and S_i', $\bar{\Omega}_i'$ is the complementary domain of Ω_i'. Here, $\Omega_i' = \Omega_i + \Omega_{b(i)}$ where $\Omega_{b(i)}$ denotes the buffer domain of Ω_i. Similarly, $V_i' = V_i + V_{b(i)}$ and $S_i' = S_i + S_{b(i)}$. Combining equation (8) with equation (10) and equation (11), we get the VIE-ODDM iteration scheme which is expressed as

$$T^D(\mathbf{r},\mathbf{J}^{(k)}) = -K^D(\mathbf{r},\mathbf{J}^{(k-1)}) + \mathbf{E}^i(\mathbf{r}) \quad \mathbf{r} \in V_i'. \quad (12)$$

Comparing equation (12) with equation (8), the computed domain is reduced from V to V_i', and the excitation source in the computed domain includes both the information of incident plane wave and the coupling from other subdomains.

A similar procedure can be applied for the SIE (9). We define two linear operators $T^M(\mathbf{r},\mathbf{J})$ and $K^M(\mathbf{r},\mathbf{J})$, then we can get the SIE-ODDM iteration scheme, expressed as

$$T^M(\mathbf{r},\mathbf{J}^{(k)}) = -K^M(\mathbf{r},\mathbf{J}^{(k-1)}) + \mathbf{E}^i(\mathbf{r})_{\tan} \quad \mathbf{r} \in S_i'. \quad (13)$$

Expanding the equation (12) by RWG and SWG basis function and testing it with SWG basis function, the matrix form of the VIE-ODDM can be obtained. Similarly, for equation (13), selecting RWG basis function as testing function, we can get the matrix form of the SIE-ODDM. Combining the two matrix equations, a VSIE-ODDM iteration scheme is presented as

$$\begin{bmatrix} \tilde{Z}_{ii}^{DD} & \tilde{Z}_{ii}^{DM} \\ \tilde{Z}_{ii}^{MD} & \tilde{Z}_{ii}^{MM} \end{bmatrix} \begin{bmatrix} \tilde{I}_{Di}^{(k)} \\ \tilde{I}_{Mi}^{(k)} \end{bmatrix} = \begin{bmatrix} \tilde{E}_{V_i'}^{D} \\ \tilde{E}_{S_i'}^{M} \end{bmatrix} - \sum_{j<i, c(j)\notin b(i)} \begin{bmatrix} \tilde{Z}_{ij}^{DD} & \tilde{Z}_{ij}^{DM} \\ \tilde{Z}_{ij}^{MD} & \tilde{Z}_{ij}^{MM} \end{bmatrix} \begin{bmatrix} I_{Dj}^{(k)} \\ I_{Mj}^{(k)} \end{bmatrix} - \sum_{j>i, c(j)\notin b(i)} \begin{bmatrix} \tilde{Z}_{ij}^{DD} & \tilde{Z}_{ij}^{DM} \\ \tilde{Z}_{ij}^{MD} & \tilde{Z}_{ij}^{MM} \end{bmatrix} \begin{bmatrix} I_{Dj}^{(k-1)} \\ I_{Mj}^{(k-1)} \end{bmatrix} \quad i = 1, 2, \cdots, M. \quad (14)$$

Here, M denotes the number of subdomain, $\begin{bmatrix} \tilde{E}_{V_i'}^{D} & \tilde{E}_{S_i'}^{M} \end{bmatrix}^T$ represents the vector of incident field in the ith extended subdomain Ω_i'. $\tilde{Z}_{ii}^{DD}$, $\tilde{Z}_{ii}^{DM}$, $\tilde{Z}_{ii}^{MD}$, and $\tilde{Z}_{ii}^{MM}$ are the self-impedance matrices in Ω_i'. $\tilde{Z}_{ij}^{DD}$, $\tilde{Z}_{ij}^{DM}$, $\tilde{Z}_{ij}^{MD}$, and $\tilde{Z}_{ij}^{MM}$ are the mutual-impedance matrices between Ω_j and Ω_i'. By solving the equation (14) and discarding the current in the buffer domain $\Omega_{b(i)}$, the current in subdomain Ω_i could be updated. The process of solving the equation (14) is an inner iteration. By several outer iterations, we can get the current in the entire domain.

E. The VSIE-ODDM-MLFMA solver

The MLFMA may be employed to accelerate the matrix vector product. The entire object is first enclosed into a large cube, which is partitioned into eight smaller cubes. Each subcube is then recursively subdivided into smaller cubes until the edge length of the finest cube is about 0.1 wavelength. In ODDM, the whole computed domain needs to be decomposed into iterative domain and incident domain. However, when combining the ODDM and MLFMA, it is necessary to consider the problems of decomposition and grouping simultaneity.

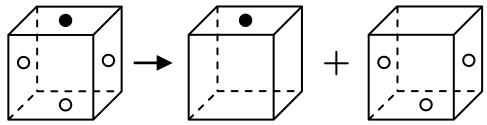

Fig. 4. The cube belongs to iterative domain and incident domain simultaneity. (● , ○ represent basis function units in the ith iterative and incident domain, respectively.)

In VSIE-ODDM-MLFMA, for a certain cube of a certain MLFMA layer, if no less than one basis function unit is located in ith iterative domain or incident domain, the cube belongs to ith iterative domain or incident domain. As is shown in Fig. 4, the cube (a) belongs to ith iterative and incident domain simultaneity because it has both ● and ○ basis function units. As a cube in ith iterative domain, the cube (a) is equal to cube (b), while as a cube in ith incident domain, the cube (a) is equal to cube (c). Due to outside of the iterative domain, the ○ basis function units will contribute outgoing radiation (called aggregation) but do not receive updates via translation and disaggregation.

F. Computational complexity analysis of the VSIE-ODDM-MLFMA

The computational complexity for the VSIE-ODDM-MLFMA is composed of the inner and outer iterations. We define the average number of unknowns in every iterative domain as $N_i=N/M+N_b$ where N is the total number of unknowns, N_b denotes the average number of unknowns in buffer domain. Suppose that the average number of inner iterations is ξ, the average CPU time of solving each iterative domain is $O(\xi N_i \log N_i)$. Assuming that the number of the outer iterations is ς, then the total CPU time of the inner iteration is about

$$O(\varsigma \cdot M \cdot \xi \cdot N_i \log N_i)$$
$$= O(\varsigma \cdot M \cdot \xi \cdot (\frac{N}{M} + N_b) \log(\frac{N}{M} + N_b))$$
$$= O(\varsigma \cdot \xi \cdot (N + MN_b) \log(\frac{N}{M} + N_b)). \tag{15}$$

When the size of the whole coefficient matrix is fixed, the CPU time of inner iteration is mostly determined by $\varsigma \cdot \xi$. According to past experience, the accuracy of both electric current and radar cross section (RCS) could generally meet the requirements when ς is 3. Obviously, the memory requirement for the inner iteration is $O(N_i \log N_i)$. When using an iterative solver to solve the problems, only near-field matrix elements need to be stored. So the VSIE-ODDM-MLFMA is better than VSIE and VSIE-ODDM in the aspects of memory requirement or computational efficiency. In contrast to VSIE-MLFMA, the memory requirement is reduced significantly, which is very important to analyze electrically large problems.

III. NUMERICAL RESULTS

To demonstrate the accuracy and efficiency of the proposed method, several numerical examples are presented in this section.

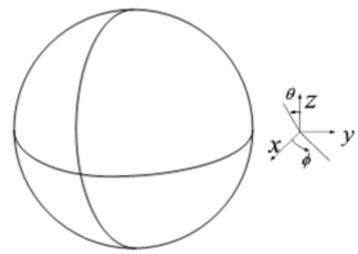

Fig. 5. Perfectly conducting sphere coated with dielectric layer.

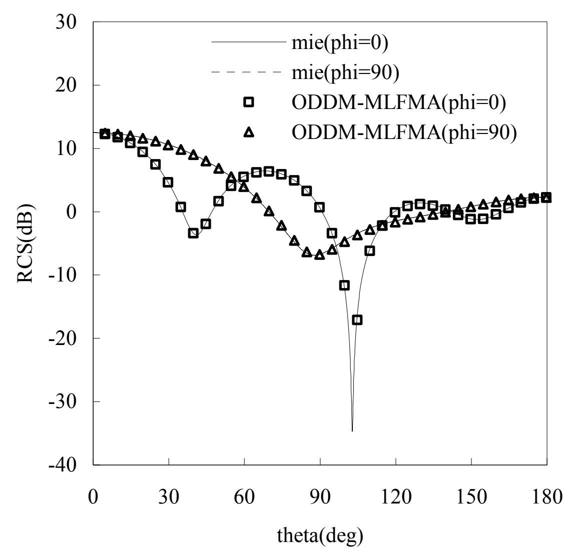

Fig. 6. Bistatic radar cross sections of a dielectric-coated sphere.

The first example is a perfectly conducting sphere with a diameter of $0.3423\lambda_0$, which is coated with a $0.1017\lambda_0$ thick dielectric layer whose relative dielectric constant is ε_r=2. The mixed structure is illuminated by a plane wave. In order to use the VSIE-ODDM-MLFMA, the target is decomposed into four domains. The dielectric domain is discretized into tetrahedrons and the metal domain is discretized into triangles, as a result, 14332 SWG basis functions and 963 RWG basis functions are generated.

The bistatic RCS computed by the VSIE-ODDM-MLFMA is shown in Figure 6. The comparison with the exact Mie series solution is given and excellent agreement is found. The example demonstrates the accuracy of VSIE-ODDM-MLFMA for analyzing the structure mixed metal with dielectric.

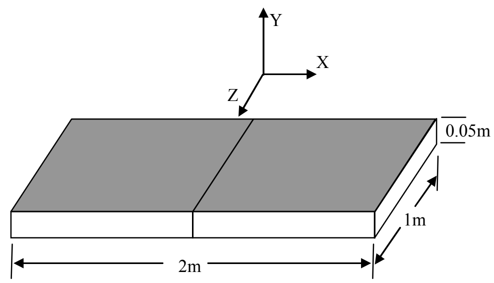

Fig. 7. A dielectric cuboid coated with a metal layer on the surface.

As shown in Figure 7, the second example is a dielectric cuboid coated with a metal layer on the surface whose specific size is marked. The relative permittivity of the dielectric cuboid is 1.6. The incident wave frequency is 300MHz. To apply the ODDM, first we divide the computed domain into two domains averagely in X direction. Then we discretize the dielectric and metal domains as the first example, as a result, 4959 basis functions are generated, which includes 4323 SWG basis functions and 636 RWG basis functions.

We use VSIE-MLFMA program, VSIE-ODDM-MLFMA program, VSIE-ODDM program and VSIE program to compute bistatic RCS of the target respectively. The comparative results are presented in Figure 8.

As shown in Table 1, the comparison of the total memory requirement and CPU time between VSIE-ODDM-MLFMA and VSIE-MLFMA is provided. In VSIE-ODDM-MLFMA, the total memory requirement is 42288KB, which is reduced by 35.3% significantly in contrast to 65364KB in VSIE-MLFMA. If we divide the computed domain into more subdomains, the memory requirement will be further reduced. This experiment results also tell us that the total memory requirement of VSIE-ODDM-MLFMA only accounts for 10.6% of VSIE, 20.4% of VSIE-ODDM, and the CPU time is reduced significantly in contrast to VSIE and VSIE-ODDM.

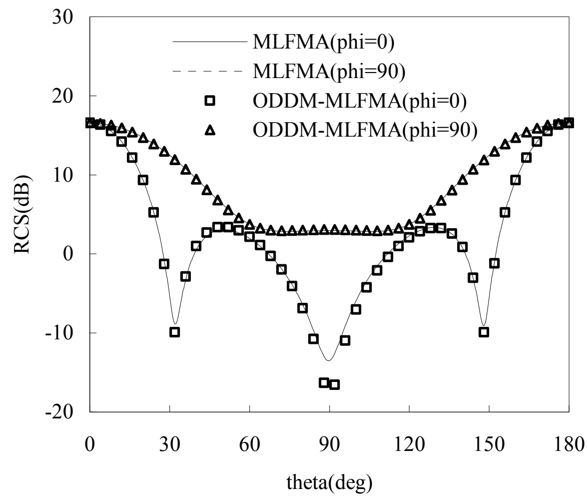

(a)

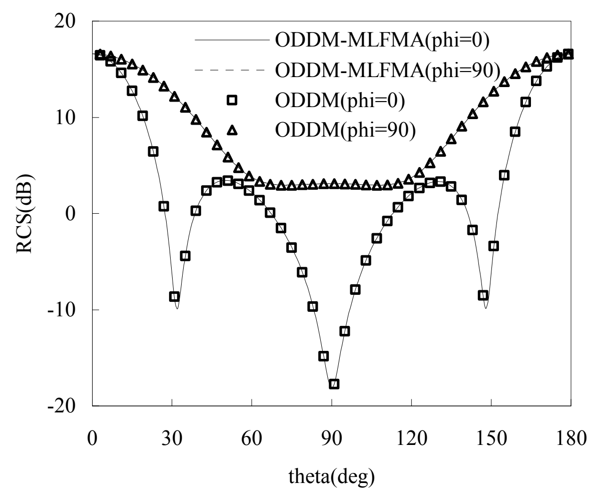

(b)

Fig. 8. Bistatic radar cross sections of a dielectric cuboid coated with a metal layer on the surface.

Table 1: The comparison of the total memory requirement and CPU time between VSIE-MLFMA and VSIE-ODDM-MLFMA

Method	Memory requirement(KB)	CPU time(s)
VSIE-MLFMA	65364	88
VSIE-ODDM-MLFMA	42288	132

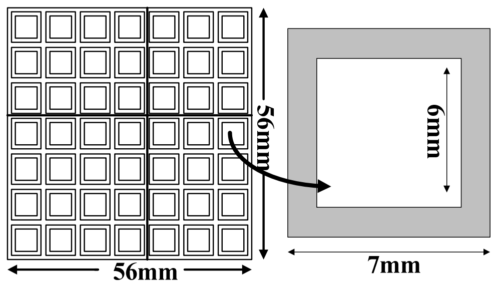

Fig. 9. The illustration of a 7×7 planar FSS array and the square ring unit.

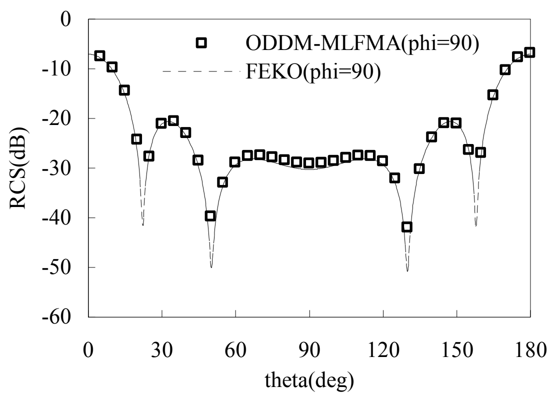

(a)

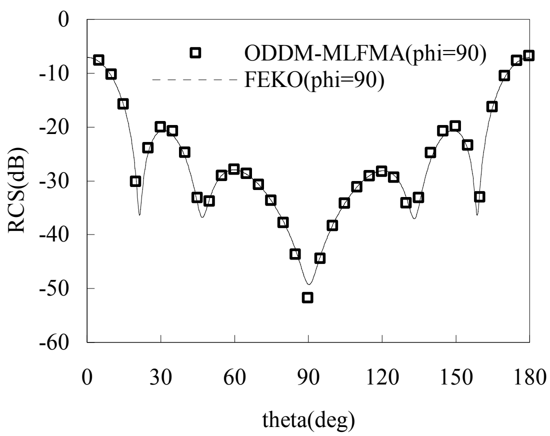

(b)

Fig. 10. Bistatic radar cross sections computed by the VSIE-ODDM-MLFMA and FEKO.

In order to further demonstrate the VSIE-ODDM-MLFMA has the ability to solve the problems of complicated structure, we take the third example of a 7×7 FSS array whose dimension is shown in Figure 9. The FSS unit is square ring whose outside edge length D1 is 7mm, inside edge length D2 is 6mm, and cycle is 8mm.The dielectric substrate has 56mm in length, 56mm in width, and 0.5mm in thickness with the relative permittivity ε_r=3.0. To use the ODDM, we first divide the computed domain into four inhomogeneous domains, then discretize them into tetrahedrons in dielectric domain and triangles in metal domain, respectively. As a result, 30213 SWG basis functions and 1372 RWG basis functions are generated. The FSS array is illuminated by a TM polarization wave from the vertical direction at 14 GHz. The RCS results computed by the proposed method are plotted in Figure 10. The comparison with the FEKO is given and the good agreement between the two methods is obtained.

The experimental results in Figure 10 have demonstrated the proposed method has the ability to solve electromagnetic scattering problems of complicated structure accurately.

IV. CONCLUSION

In this paper, the ODDM and MLFMA are introduced to the VSIE simultaneity, which could solve the problem of insufficient hardware sources and improve the efficiency. Numerical results of the presented examples demonstrate the accuracy and efficiency of this proposed method. It shows that the VSIE-ODDM-MLFMA can solve complicated electromagnetic problems successfully.

REFERENCES

[1] S. M. Rao, D. R. Wilton and A. W. Glisson, “Electromagnetic scattering by surface of arbitrary shape,” *IEEE Trans. Antennas Propagat.*, vol. AP-30, no. 3, pp. 409-418, 1982.

[2] K. A. Michalski, and D. L. Zheng, “Electromagnetic scattering and radiation by surfaces of arbitrary shape in layered media, part I: theory,” *IEEE Trans. Antennas and Propag.*, vol.38, no.3, pp. 335-344, March 1990.

[3] D. Ding, J. Ge, R. Chen, “Well-Conditioned CFIE for Scattering from Dielectric Coated Conducting Bodies above a Half-Space,” *ACES Journal*, vol. 25, no. 11, pp. 936-946, November 2010.

[4] R. Coifman, V. Rokhlin, and S. M. Wandzura, “The fast multipole method for the wave equation: A pedestrian prescription,” *IEEE Trans. Antennas and Propag.*, vol. 35, no. 3, pp. 7-12, June 1993.

[5] C. C. Lu and W. C. Chew, “A multilevel algorithm for solving boundary integral equations of wave scattering,” *Micro. Opt. Tech. Lett.*, vol. 7, pp. 466-470, July 1994.

[6] J. M. Song, W. C. Chew, “Multilevel fast-multipole algorithm for solving combined field

integral equation of electromagnetic scattering," *Micro. Opt. Tech. Lett.,* vol. 10, pp. 14-19, September 1995.

[7] M. M. Li, H. Chen, C. Li, R. S. Chen, C. Ong, "Hybrid UV/MLFMA Analysis of Scattering by PEC Targets above a Lossy Half-Space," *ACES Journal*, vol. 26, no. 1, pp. 17-25, January 2011.

[8] J. M. Song, C. C. Lu, W. C. Chew, "Multilevel fast multipole algorithm for electromagnetic scattering by large complex objects," *IEEE Trans. Antennas Propagat.*, vol. 45, no. 10, pp. 1488-1493, 1997.

[9] X. C. Nie, N. Yuan, L. W. Li, Y. B. Gan, and T. S. Yeo, "A fast volume-surface integral equation solver for scattering from composite conducting-dielectric objects," *IEEE Trans. Antennas Propag.*, vol. 53, no. 2, pp. 818-824, 2005.

[10] C. C. Lu and W. C. Chew, "A coupled surface-volume integral equation approach for the calculation of electromagnetic scattering from composite metallic and material targets," *IEEE Trans. Antennas Propagat.*, vol. 48, no. 12, pp. 1866-1868, 2000.

[11] T. K. Shark, S. M. Rao, and A. R. Djordievic, "Electromagnetic scattering and radiation from finite microstrip structures," *IEEE Trans. on Microwave Theory and Tech.*, vol. 38, no. 11, pp. 1568-1575, 1990.

[12] D. H. Schaubert, D. R. Wilton, and A. W. Glisson, "A tetrahedral modeling method for electromagnetic scattering by arbitrarily shaped inhomogeneous dielectric bodies," *IEEE Trans. Antennas Propagat.*, vol. AP-32, no. 1, pp. 77-85, 1984.

[13] A. Toselli and O. Widlund, Domain Decomposition Methods-Algorithms and Theory, Springer, Berlin, 2005.

[14] C. Brennan, P. Cullen, and M. Condon, "A novel iterative solution of three dimensional electric field integral equation," *IEEE Trans. Antennas Propagat.*, vol. 52, no. 10, pp. 2781-2784, 2004.

[15] W. D. Li, W. Hong, and H. X. Zhou, "Integral equation-based overlapped domain decomposition method for the analysis of electromagnetic scattering of 3D conducting objects," *Microw. Opt. Tech. Lett.*, vol. 49, no. 2, pp. 265 - 274, February 2007.

[16] H. Zhao, J. Hu, Z. Nie, "Parallelization of MLFMA with Composite Load Partition Criteria and Asynchronous Communication," *ACES Journal*, vol. 25, no. 2, pp. 167-173, February 2010.

[17] K. C. Donepudi, J. M. Jin et al, "A higher order parallelized multilevel fast multipole algorithm for 3-D scattering," *IEEE Trans. Antennas and Propag.*, vol. 49, no. 7, pp. 1069-1078, July. 2001.

[18] R. S. Chen, E. K. N. Yung, C. H. Chan, and D. G. Fang, "Application of SSOR preconditioned conjugate gradient algorithm to edge-FEM for 3-dimensional full wave Electromagnetic boundary value problems," *IEEE Trans. on Microwave Theory and Tech.*, vol. 50, no. 4, pp. 1165-1172, 2002.

[19] N. Engheta, W. D. Murphy, V. Rokhlin, and M. S. Vassiliou, "The fast multipole method (FMM) for electromagnetic scattering problem," *IEEE Trans. Antennas Propagat.*, vol. 40, no. 6, pp. 634-641, 1992.

Jialin Chen was born in Leshan, Sichuan, the People's Republic of China in 1986. He received his B.Sc. degree in radar engineering and M.Sc. degree in electromagnetic field and microwave technique from Department of Electronic and Communication Engineering, Naval Aeronautical Engineering Institute, Yantai, China, in 2007 and 2009, respectively. He is currently working toward the Ph.D. degree in information and communication engineering at Naval Aeronautical Engineering Institute. His current research interests include computational electromagnetics, antennas, electromagnetic scattering and propagation, and radar target recognition.

Shangsheng Li was born in Shandong, P. R. China in 1965. He received his B.Sc. degrees from Southeast University and M.Sc. degree from Nanjing University of Aeronautics and Astronautics, in 1987 and 1996, respectively. Now he is a professor in Naval Aeronautical Engineering Institute. His research interests mainly include microwave/millimeter-wave systems, antenna, and computational electromagnetics.

Yaping Song was born in Hunan, P. R. China in 1987. He received his B.Sc. and M.Sc. degrees from Naval Aeronautical Engineering Institute, Yantai, China, in 2008 and 2010, respectively. His research interests include computational electromagnetics, electromagnetic scattering and radiation.

Parametric Design of Open Ended Waveguide Array Feeder with Reflector Antenna for Switchable Cosecant-Squared Pattern

Okan Mert Yucedag [1,2], Ahmet Serdar Turk [1]

[1] Yildiz Technical University, Electronics and Telecommunication Engineering Department
Esenler, 34220, Istanbul, TURKEY
asturk@yildiz.edu.tr

[2] TUBITAK Center of Research for Advanced Technologies of Informatics and Information Security
P.O. Box 21, Gebze, 41470, Kocaeli, TURKEY
okanmert.yucedag@bte.tubitak.gov.tr

Abstract ─ This paper presents parametric analysis of two-dimensional (2D) open-ended waveguide array feeder and introduces a modified parabolic reflector antenna structure to obtain electronically switchable radiation patterns. The main motivation of the study is to achieve desired radiation characteristics for naval, air and coastal surveillance radars such as, pencil beam, suppressed side lobes and cosecant-squared pattern shapes. The Analytical Regularization Method (ARM) is used as a fast and accurate pre-design tool to compute near and far field radiation characteristics of the feeder and reflector antennas. The numerical procedure is initially verified by the analytical methods and the calculated results are presented for the proposed novel designs.

Index Terms ─ Open-ended waveguide array, Parabolic reflector antenna, Cosecant squared pattern, Analytical regularization method.

I. INTRODUCTION

Typical surveillance radar systems generally have a parabolic reflector, which has cosecant-squared elevation pattern [1]. The feeder configurations must be considered primarily to estimate the radiation characteristics of reflector conveniently. Waveguide or horn antenna arrays are widely used to feed the reflector antennas. Suitable feeder configurations, which can illuminate the reflector efficiently, must be designed to meet requirements of modern radar systems. Geometrical optics (GO), physical optics (PO), aperture integration (AI) and geometric theory of diffraction (GTD), or optimization methods can be used for determining the antenna radiation characteristics [2-6]. Moreover, method of moments (MoM), finite element method (FEM) and finite difference methods can be used for feeder and reflector designs [7-8]. However, large size antenna analyses usually require long computation times [9-10]. Furthermore, the complexity of some cavity or aperture geometries creates hard numerical convergence problems in many cases. The origin of these problems is related to the direct numerical methods, which reduce a diffraction boundary value problem (BVP) to the functional equation of the first kind. First kind equations may typically have a singular kernel that causes unstable numerical process. Thus, while the truncation number of the matrix-vector algebraic equation set increases, computational error degradation cannot be guaranteed [11-13]. Hence, ARM that transforms the ill-conditioned integral equation of the first kind into a well-conditioned one of the second

Submitted On: April 23, 2012
Accepted On: July 22, 2012

kind is preferred to solve the matrix equation numerically by truncation method with fast convergence to reach fast and reliable solutions [14]. The ARM is implemented for solving the 2D problem of E-polarized wave diffraction by arbitrary shaped, smooth and perfectly conductive cylindrical obstacles to obtain fast, accurate and reliable results [15-16]. The ARM solutions for the 2D parabolic reflector and the H-plane horn feeder have already been demonstrated by Turk [10, 18-20].

In this paper, parametric characterization of the 2D open-ended waveguide array feeder and the design of modified reflector antenna are presented to achieve electronically switchable pencil beam and cosecant-squared radiation patterns for naval, air and coastal surveillance radars. Feeder is located on the focus of the reflector. Geometry of the problem is illustrated in Fig. 1.

Section II explains the general theory of ARM. Section III presents the parametric analysis of wave guide array feeder. Section IV describes the reflector design for pencil-beam and cosecant-squared switchable pattern with exhibition of performance results. Section V is the conclusion.

II. ARM FORMULATION

Scalar diffraction problem of an infinitely long, smooth, longitudinally homogeneous and perfectly conducting cylindrical obstacle corresponds to the Dirichlet boundary condition for E-polarized incident wave. The incident and scattered scalar wave functions ($u^i(p)$ and $u^s(p)$) must satisfy the Helmholtz equation given in Eq. (1) and the Dirichlet boundary condition in (2), also with the Sommerfeld radiation condition.

$$\left(\Delta + k^2\right)u^s(p) = 0, \quad p \in R^2 \backslash \mathrm{S} \tag{1}$$

$$u^{s(+)}(p) = u^{s(-)}(p) = -u^i(p), \quad p \in S \tag{2}$$

where, S is smooth XOY cross section contour of the domain D in 2D space $R^2 \in C^2$, $u^{s(+)}(p)$ and $u^{s(-)}(p)$ are limiting values of $u^s(p)$ in the inner and the outer sides of S, respectively. The solution of the BVP is written in (3), using the Green's formula and the boundary condition in (2) [14].

$$-\frac{i}{4}\int_S \left[H_0^{(1)}(k\,|q-p|)Z(p)\right]dl_p = -u^i(q) \tag{3}$$

where, $Z(p) = \dfrac{\partial u^{s(-)}(p)}{\partial n} - \dfrac{\partial u^{s(+)}(p)}{\partial n}, \quad q, p \in S$; n is the unit outward with respect to S normal of the point p. The unknown function $Z(p)$ is constructed by solving (3), and using parameterization of the S contour specified by the function $\eta(\theta)=(x(\theta),y(\theta))$ that smoothly parameterizes the S by $\theta\in[-\pi,\pi]$. The integral equation representation of the first kind in (3) is equivalently arranged as follows:

$$\frac{1}{2\pi}\int_{-\pi}^{\pi}\left[\ln\left|2\sin\frac{\theta-\tau}{2}\right| + K(\theta,\tau)\right]Z_D(\tau)d\tau = g(\theta) \tag{4}$$

with the unknown function $Z_D(\tau)$ and the given function $g(\theta)$, where $\theta\in[-\pi,\pi]$ and

$$Z_D(\theta) = l(\theta)Z(\eta(\theta)), g(\theta) = -u^i(\eta(\theta)) \tag{5}$$

$$l(\theta) = \sqrt{[x'(\theta)]^2 + [y'(\theta)]^2} > 0, \quad x(\theta), y(\theta) \in C^\infty\left(Q^1\right) \tag{6}$$

The logarithmic part in (4) represents the main singularity and $K(\theta,\tau)$ is rather smooth section of the Green's function. The functions in (4) are represented by their Fourier series expansions with $k_{s,m}$, z_m, g_m coefficients. An infinite system of the linear algebraic equations of the second kind can be obtained [15]:

$$\hat{z}_s + \sum_{m=-\infty}^{\infty}\hat{k}_{s,m}\hat{z}_m = \hat{g}_s, \quad s = \pm1, \pm2, .. \tag{7}$$

where

$$\begin{gathered}\hat{k}_{s,m} = -2\tau_s\tau_m\left[k_{s,-m} + \frac{1}{2}\delta_{s,0}\delta_{m,0}\right],\\ \hat{z}_n = \tau_n^{-1}z_n,\ \hat{g} = -2\tau_s g_s\\ \tau_n = \max(1,|n|^{1/2}), \quad n = 0, \pm1, \pm2, ..\end{gathered} \tag{8}$$

and $\delta_{s,0}$ is the Kronecker delta function. Finally, the scattered field $u^s(q)$ for $q\in R^2$ is obtained by the integral equation representation of the (4) with any required accuracy by the truncation method [16].

The ARM procedure has already been verified by the analytical solution of wave scattering from infinitely long circular cylinder [10]. Moreover, it is compared with the analytical Wiener-Hopf solution of scattering from parallel-plate waveguide cavity for the case of E-polarized plane wave incidence from 60°, which is given in Fig. 2 [17].

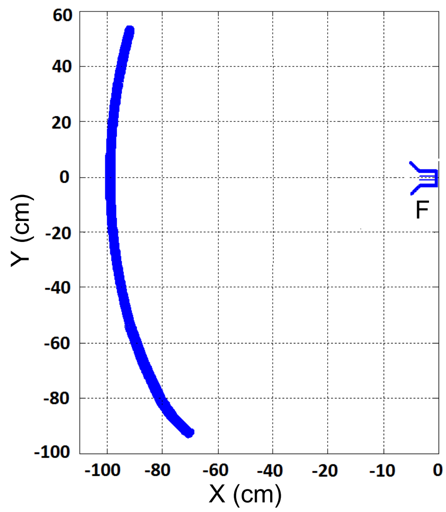

Fig. 1. XOY-plane geometry of reflector antenna.

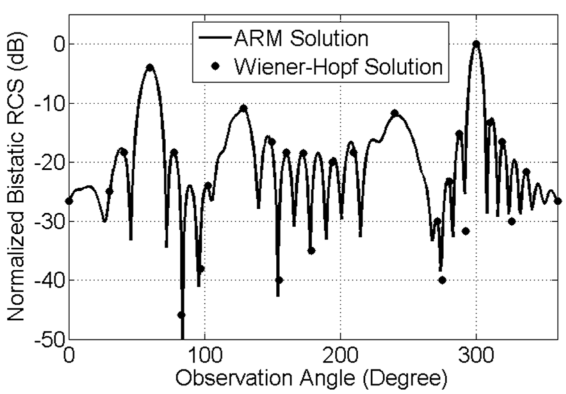

Fig. 2. Comparison of the ARM calculation with analytical result of scattering from open-ended waveguide for 60° plane wave incidence.

III. PARAMETRIC ANALYSIS OF WAVEGUIDE ARRAY FEEDER

The ARM procedure described at Section II is derived for the investigated waveguide array feeder. The geometrical cross-section of the feeder is modeled by ARM, as a closed contour L that goes from point A to point Z and back to A corresponding to $\theta \in [-\pi,\pi]$, as illustrated in Fig. 3. The relation between l and θ is formulated in (9). Distances of sources from inner wall are $\lambda/4$.

$$\left.\begin{array}{l} l=(\theta+\pi)L/2\pi \\ l\in[0,L]\rightarrow(\theta,\tau)\in[-\pi,\pi] \end{array}\right\} \tag{9}$$

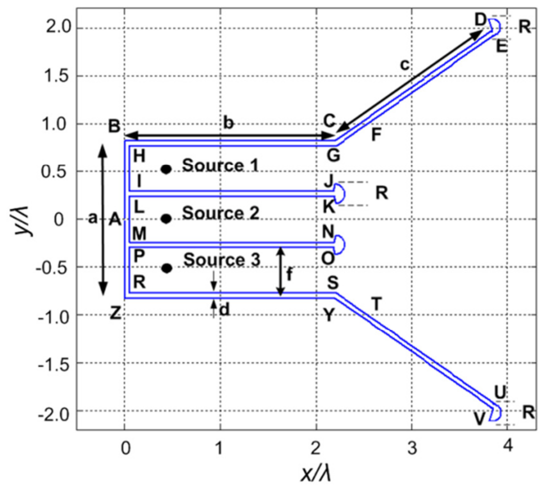

Fig. 3. XOY-plane geometry of 3-elements open-ended and flared waveguide array.

The feeder structure consists of totally 23 contour parts that are defined in Table I. The parameterization of the contour line is implemented separately from point A to Z, and back to A by means of the variable $l \in [0, L]$ as given in Table 1 and Table 2.

Parametric analysis results of the waveguide length, waveguide width, flare angle and edge rolling effects on the H-plane radiation pattern are presented in Figs. 4-7, respectively. The major comments are highlighted briefly that; increasing the waveguide length decreases back lobe levels (see Fig. 4). The waveguide width should be arranged as less than 0.75λ to avoid multi-mode propagation (see Fig. 5). Increasing the flare angle does not yield significant effect for waveguide array (see Fig. 6), although it can suppress back lobe levels up to 15 dB for the single horn [20]. The edge rolling can slightly improve the side and back lobe suppression performance (see Fig. 7).

Since electronically shaping of the reflector radiation pattern mainly depends on the aperture illumination, the most critical design parameter of the feeder is source phases. The electronically beam scanning performance of the waveguide array feeder is demonstrated in Fig. 8. The phase difference of 7° is proposed to obtain the near field illumination in Fig. 11 for the suitable cosecant-squared pattern given in Fig. 12.

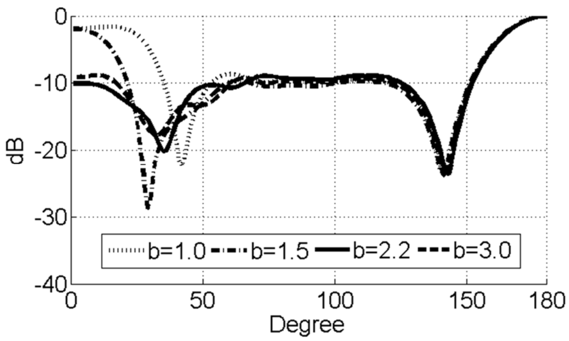

Fig. 4. H-plane radiation pattern of the feeder for *c=2λ, d=0.05λ, f=0.481λ, R=1λ, α =25°.*

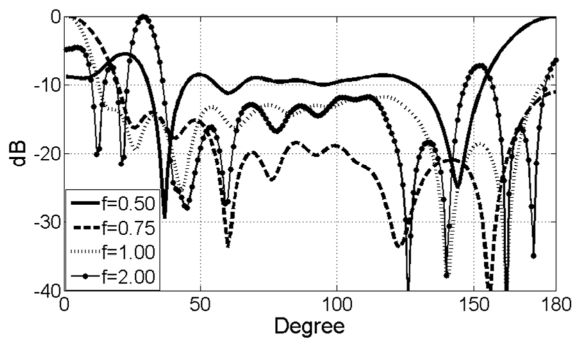

Fig. 5. H-plane radiation pattern of the feeder for *b=2.2λ, c=2.0λ d=0.05λ, R=1λ, α =25°.*

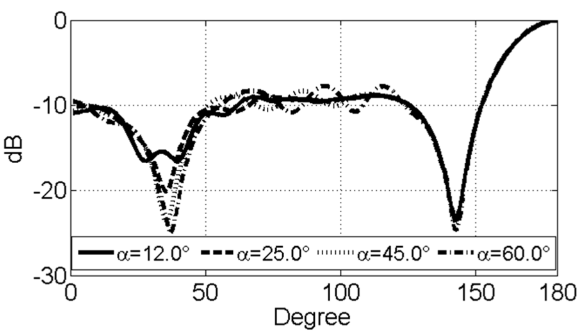

Fig. 6. H-plane radiation pattern of the feeder for *b=2.2λ, c=2λ, d=0.05λ, f=0.481λ, R=1λ.*

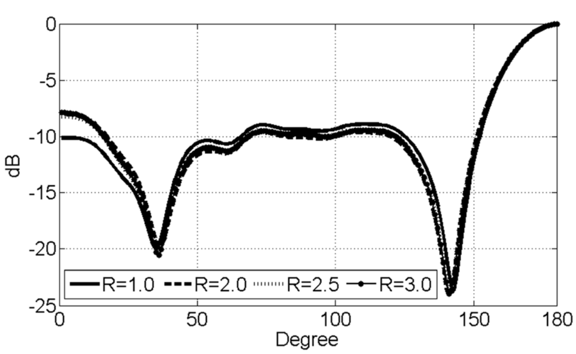

Fig. 7. H-plane radiation pattern of the feeder for *b=2.2λ, c=2.0λ, d=0.05λ, f=0.481λ, α =25°.*

Table 1: Segment lengths of the feeder contour regions

No	Segment Definition	Segment Length
1	$-\pi \le \theta < 2L_1\frac{\pi}{L}-\pi$	$L_1 = a$
2	$2L_1\frac{\pi}{L}-\pi \le \theta < 2L_2\frac{\pi}{L}-\pi$	$L_2 = L_1 + b$
3	$2L_2\frac{\pi}{L}-\pi \le \theta < 2L_3\frac{\pi}{L}-\pi$	$L_3 = L_2 + c$
4	$2L_3\frac{\pi}{L}-\pi \le \theta < 2L_4\frac{\pi}{L}-\pi$	$L_4 = L_3 + 0.5\pi Rd$
5	$2L_4\frac{\pi}{L}-\pi \le \theta < 2L_5\frac{\pi}{L}-\pi$	$L_5 = L_4 + c - d/\tan\alpha_1$
6	$2L_5\frac{\pi}{L}-\pi \le \theta < 2L_6\frac{\pi}{L}-\pi$	$L_6 = L_5 + d/\sin\varphi_1$
7	$2L_6\frac{\pi}{L}-\pi \le \theta < 2L_7\frac{\pi}{L}-\pi$	$L_7 = L_6 + b - db_1 + d$
8	$2L_7\frac{\pi}{L}-\pi \le \theta < 2L_8\frac{\pi}{L}-\pi$	$L_8 = L_7 + f$
9	$2L_8\frac{\pi}{L}-\pi \le \theta < 2L_9\frac{\pi}{L}-\pi$	$L_9 = L_8 + b - d$
10	$2L_9\frac{\pi}{L}-\pi \le \theta < 2L_{10}\frac{\pi}{L}-\pi$	$L_{10} = L_9 + 0.5\pi Rd$
11	$2L_{10}\frac{\pi}{L}-\pi \le \theta < 2L_{11}\frac{\pi}{L}-\pi$	$L_{11} = L_{10} - d + b$
12	$2L_{11}\frac{\pi}{L}-\pi \le \theta < 2L_{12}\frac{\pi}{L}-\pi$	$L_{12} = L_{11} + f$
13	$2L_{12}\frac{\pi}{L}-\pi \le \theta < 2L_{13}\frac{\pi}{L}-\pi$	$L_{13} = L_{12} + b - d$
14	$2L_{13}\frac{\pi}{L}-\pi \le \theta < 2L_{14}\frac{\pi}{L}-\pi$	$L_{14} = L_{13} + 0.5\pi Rd$
15	$2L_{14}\frac{\pi}{L}-\pi \le \theta < 2L_{15}\frac{\pi}{L}-\pi$	$L_{15} = L_{14} - d + b$
16	$2L_{15}\frac{\pi}{L}-\pi \le \theta < 2L_{16}\frac{\pi}{L}-\pi$	$L_{16} = L_{15} + f$
17	$2L_{16}\frac{\pi}{L}-\pi \le \theta < 2L_{17}\frac{\pi}{L}-\pi$	$L_{17} = L_{16} + b - db_2 + d$
18	$2L_{17}\frac{\pi}{L}-\pi \le \theta < 2L_{18}\frac{\pi}{L}-\pi$	$L_{18} = L_{17} + d/\sin\varphi_2$
19	$2L_{18}\frac{\pi}{L}-\pi \le \theta < 2L_{19}\frac{\pi}{L}-\pi$	$L_{19} = L_{18} + c - d/\tan\alpha_2$
20	$2L_{19}\frac{\pi}{L}-\pi \le \theta < 2L_{20}\frac{\pi}{L}-\pi$	$L_{20} = L_{19} + 0.5\pi Rd$
21	$2L_{20}\frac{\pi}{L}-\pi \le \theta < 2L_{21}\frac{\pi}{L}-\pi$	$L_{21} = L_{20} + c$
22	$2L_{21}\frac{\pi}{L}-\pi \le \theta < 2L_{22}\frac{\pi}{L}-\pi$	$L_{22} = L_{21} + b$
23	$2L_{22}\frac{\pi}{L}-\pi \le \theta < 2L_{23}\frac{\pi}{L}-\pi$	$L = L_{22} + a$
$db_1 = d/\tan\varphi_1 - d/\tan\alpha_1 - 0.5d\sin\alpha_1$ $db_2 = d/\tan\varphi_2 - d/\tan\alpha_2 - 0.5d\sin\alpha_2$		

Table 2: Parametric definitions of feeder contour

No	Region	Parameterization
1	*AB*	$x=0$; $y=l-L_1+a$
2	*BC*	$x=l-L_1$; $y=a$
3	*CD*	$x=b+(l-L_2)\cos(\alpha_1)$; $y=a+(l-L_2)\sin(\alpha_1)$
4	*DE*	$x=0.5d\sin(\alpha_1)+b+c\cos(\alpha_1)+0.5Rd\cos(0.5\pi+\alpha_1)$ $-2(l-L_3)/Rd+X_0$; $y=-0.5d\cos(\alpha_1)+a+c\sin(\alpha_1)+0.5Rd\sin(0.5\pi+\alpha_1)$ $-2(l-L_3)/Rd+Y_0$; $X_0=0.5(1-R)d\sin(\alpha_1);Y_0=0.5(R-1)d\cos(\alpha_1)$
5	*EF*	$x=b+d\sin(\alpha_1)+(c-(l-L_4))\cos(\alpha_1)$; $y=a-d\cos(\alpha_1)+(c-(l-L_4))\sin(\alpha_1)$;
6	*FG*	$x=d/\sin(\alpha_1)+b-(l-L_5)\cos(\varphi_1)$; $y=a-(l-L_5)\sin(\varphi_1)$;
7	*GH*	$x=-l+L_6+b-db1$; $y=a-d$;
8	*HI*	$x=d$; $y=-l+L_7+a-d$;
9	*IJ*	$x=l-L_8+d$; $y=a-d-f$;
10	*JK*	$x=b+0.5R_1d\cos(\pi/2-2(l-L_9)/(R_1d))$; $y=a-1.5d-f+0.5R_1d\sin(\pi/2-2(l-L_9)/(R_1d))$;
11	*KL*	$x=L_{10}-l+b$; $y=a-2d-f$;
12	*LM*	$x=d$; $y=L_{11}-l+a-2d-f$;
13	*MN*	$x=l-L_{12}+d$; $y=a-2d-2f$;
14	*NO*	$x=b+0.5R_1d\cos(\pi/2-2(l-L_{13})/(R_1d))$; $y=a-2.5d-2f+0.5R_1d\sin(\pi/2-2(l-L_{13})/(R_1d))$;
15	*OP*	$x=L_{14}-l+b$; $y=a-3d-2f$;
16	*PR*	$x=d$; $y=L_{15}-l+a-3d-2f$;
17	*RS*	$x=l-L_{16}+d$; $y=d-a$;
18	*ST*	$x=b-db2+(l-L_{17})\cos(\varphi_2)$; $y=d-a-(l-L_{17})\sin(\varphi_2)$
19	*TU*	$x=b+d/\tan(\alpha_2)-db2+(l-L_{18})\cos(\alpha_2)$; $y=-a-(l-L_{18})\sin(\alpha_2)$
20	*UV*	$x=0.5d\sin(\alpha_2)+b+c\cos(\alpha_2)+0.5Rd\cos(0.5\pi-\alpha_2)$ $-2(l-L_{19})/Rd+X_0$; $y=-0.5d\cos(\alpha_2)+a+c\sin(\alpha_2)+0.5Rd\sin(0.5\pi-\alpha_2)$ $-2(l-L_{19})/Rd+Y_0$; $X_0=0.5(R-1)d\sin(\alpha_2);Y_0=0.5(R-1)d\cos(\alpha_2)$
21	*VY*	$x=0.5d\sin(\alpha_2)+b+c\cos(\alpha_2)+0.5Rd\cos(0.5\pi-\alpha_2)$ $-2(l-L_{19})/Rd+X_0$; $y=-0.5d\cos(\alpha_2)+a+c\sin(\alpha_2)+0.5Rd\sin(0.5\pi-\alpha_2)$ $-2(l-L_{19})/Rd+Y_0$; $X_0=0.5(R-1)d\sin(\alpha_2);Y_0=0.5(R-1)d\cos(\alpha_2)$
22	*YZ*	$x=b+L_{21}-l$; $y=-a$;
23	*ZA*	$x=0$; $y=-a+l-L_{22}$;

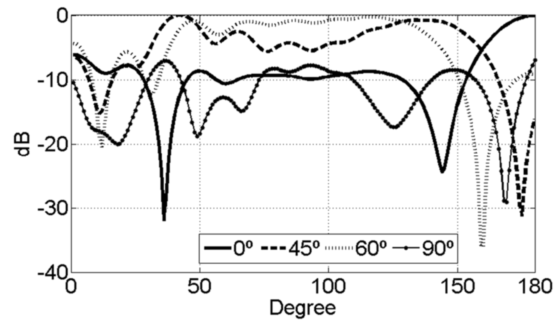

Fig. 8. Electronically scanned H-plane radiation pattern of the feeder for *b=2.2λ, c=2λ, d=0.05λ, f=0.5λ, R=1λ, α =30°.*

IV. REFLECTOR DESIGN WITH ELECTRONICALLY SWITCHABLE PATTERN

The geometrical cross-section of the reflector is modeled by ARM, as a closed contour *L* that starts from point *A* towards point *M* and returns to *A* corresponding to $\theta\in[-\pi,\pi]$, as illustrated in Fig. 9. The relation between *l* and θ is formulated in (9).

The reflector structure consists of totally 12 contour parts. The parameterization of the contour line is implemented separately from point *A* to *M,* and back to *A* by means of the variable $l\in[0,L]$ as given in Table 3 and Table 4.

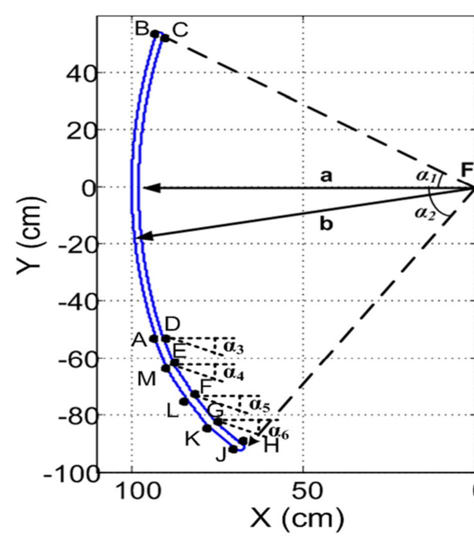

Fig. 9. Geometry of the modified reflector.

The modified reflector geometry is designed asymmetrically by adding special rims with different lengths and bending angles to obtain electronically switchable radiation patterns. Near field radiation of the array feeder is considered as the illuminator of the reflector antenna. The cosecant-squared pattern is arranged by determination of adequate near field distribution of the feeder. For this aim, waveguide feeder sources are excited with suitable phase and amplitude values to obtain the desired near field illumination.

The calculated near field distributions on the reflector for the pencil beam and cosecant-squared patterns are shown in Fig. 10 and Fig. 11. Feeder sources have same phases and amplitudes for pencil-beam. However, 7° phase differences are preferred and amplitude of the third source is increased 1.2 times for cosecant-squared pattern. H-plane normalized directivity gain patterns of the electronically switchable cosecant-squared and pencil-beam radiator are shown in Fig. 12.

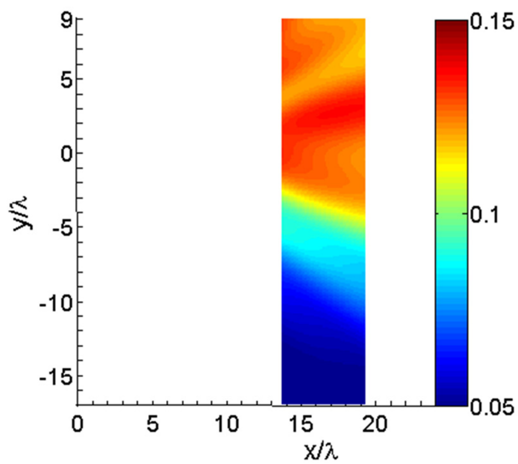

Fig. 10. Calculated near field which illuminates the reflector for pencil-beam radiation pattern.

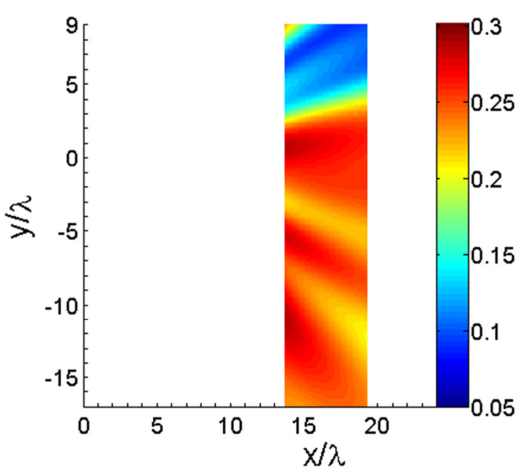

Fig. 11. Calculated near field which illuminates the reflector for cosecant-squared radiation pattern.

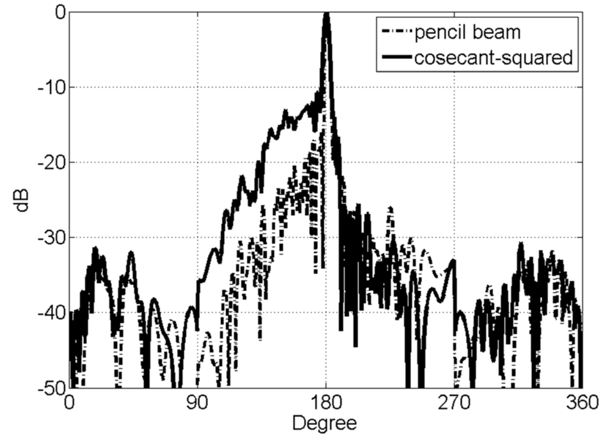

Fig. 12. H-plane normalized directivity gain patterns of the electronically switchable cosecant-squared and pencil-beam radiator.

Table 3: Segment lengths of the reflector contour regions

No	Segment Definition	Segment Length
1	$-\pi \le \theta < 2L_1 \frac{\pi}{L} - \pi$	$L_1 = 2b\tan((\alpha_2 - \alpha_1)/2)$
2	$2L_1 \frac{\pi}{L} - \pi \le \theta < 2L_2 \frac{\pi}{L} - \pi$	$L_2 = L_1 + \pi c_2$
3	$2L_2 \frac{\pi}{L} - \pi \le \theta < 2L_3 \frac{\pi}{L} - \pi$	$L_3 = L_2 + 2a\tan((\alpha_2 - \alpha_1)/2)$
4	$2L_3 \frac{\pi}{L} - \pi \le \theta < 2L_4 \frac{\pi}{L} - \pi$	$L_4 = L_3 + p_4 c_3$
5	$2L_4 \frac{\pi}{L} - \pi \le \theta < 2L_5 \frac{\pi}{L} - \pi$	$L_5 = L_4 + p_3 c_3$
6	$2L_5 \frac{\pi}{L} - \pi \le \theta < 2L_6 \frac{\pi}{L} - \pi$	$L_6 = L_5 + p_2 c_3$
7	$2L_6 \frac{\pi}{L} - \pi \le \theta < 2L_7 \frac{\pi}{L} - \pi$	$L_7 = L_6 + p_1 c_3$
8	$2L_7 \frac{\pi}{L} - \pi \le \theta < 2L_8 \frac{\pi}{L} - \pi$	$L_8 = L_7 + \pi c_2$
9	$2L_8 \frac{\pi}{L} - \pi \le \theta < 2L_9 \frac{\pi}{L} - \pi$	$L_9 = L_8 + + p_1 c_3$
10	$2L_9 \frac{\pi}{L} - \pi \le \theta < 2L_{10} \frac{\pi}{L} - \pi$	$L_{10} = L_9 + p_2 c_3$
11	$2L_{10} \frac{\pi}{L} - \pi \le \theta < 2L_{11} \frac{\pi}{L} - \pi$	$L_{11} = L_{10} + p_3 c_3$
12	$2L_{11} \frac{\pi}{L} - \pi \le \theta < \pi$	$L = L_{11} + p_4 c_3$
$c_1 = (b-a)/(1+\cos(\alpha_3))$ $c_2 = (b-a)/(1+\cos(\alpha_2))$		

Table 4: Parametric definitions of the reflector contour regions

No	Region	Parameterization
1	*AB*	$x=-2b\cos(\psi_1)/(1+\cos(\psi_1))$ $y=2b\sin(\psi_1)/(1+\cos(\psi_1))$
2	*BC*	$x=c_2\cos[(L_1-l)/c_2+\pi-\alpha_2]$ $-(a+b)\cos\alpha_2/(1+\cos\alpha_2)$ $y=c_2\sin[(L_1-l)/c_2+\pi-\alpha_2]$ $+(a+b)\sin\alpha_2/(1+\cos\alpha_2)$
3	*CD*	$x=-2a\cos(\psi_2)/(1+\cos(\psi_2))$ $y=2a\sin(\psi_2)/(1+\cos(\psi_2))$
4	*DE*	$x=-2a\cos(\alpha_1)/(1+\cos(\alpha_1))+(l-L_3)\cos(\alpha_3)$ $y=2a\sin(\alpha_1)/(1+\cos(\alpha_1))-(l-L_3)\sin(\alpha_3)$
5	*EF*	$x=-2a\cos(\alpha_1)/(1+\cos(\alpha_1))$ $+p_4c_3\cos(\alpha_3)+(l-L_4)\cos(\alpha_4)$ $y=2a\sin(\alpha_1)/(1+\cos(\alpha_1))$ $-p_4c_3\sin(\alpha_3)+(l-L_4)\sin(\alpha_4)$
6	*FG*	$x=-2a\cos(\alpha_1)/(1+\cos(\alpha_1))+(l-L_5)\cos(\alpha_5)$ $+c_3[p_4\cos(\alpha_3)+p_3\cos(\alpha_4)]$ $y=2a\sin(\alpha_1)/(1+\cos(\alpha_1))-(l-L_5)\sin(\alpha_5)$ $-c_3[p_4\sin(\alpha_3)+p_3\sin(\alpha_4)]$
7	*GH*	$x=-2a\cos(\alpha_1)/(1+\cos(\alpha_1))+(l-L_6)\cos(\alpha_6)$ $+c_3[p_4\cos(\alpha_3)+p_3\cos(\alpha_4)+p_2\cos(\alpha_5)]$ $y=2a\sin(\alpha_1)/(1+\cos(\alpha_1))-(l-L_6)\sin(\alpha_6)$ $-c_3[p_4\sin(\alpha_3)+p_3\sin(\alpha_4)+p_2\sin(\alpha_5)]$
8	*HI*	$x=c_1\cos[(L_7-l)/c_1-\alpha_1]-(a+b)\cos(\alpha_1)/(1+\cos(\alpha_1))$ $+c_3[p_4\cos(\alpha_3)+p_3\cos(\alpha_4)+p_2\cos(\alpha_5)+p_1\cos(\alpha_6)]$ $y=c_1\sin[(L_7-l)/c_1-\alpha_1]+(a+b)\sin(\alpha_1)/(1+\cos(\alpha_1))$ $-c_3[p_4\sin(\alpha_3)+p_3\sin(\alpha_4)+p_2\sin(\alpha_5)+p_1\sin(\alpha_6)]$
9	*IJ*	$x=c_1\cos(\pi+\alpha_1)-(a+b)\cos(\alpha_1)/(1+\cos(\alpha_1))-(l-L_8)\cos(\alpha_6)$ $+c_3[p_4\cos(\alpha_3)+p_3\cos(\alpha_4)+p_2\cos(\alpha_5)+p_1\cos(\alpha_6)]$ $x=c_1\sin[-\pi-\alpha_1]+(a+b)\sin(\alpha_1)/(1+\cos(\alpha_1))+(l-L_8)\sin(\alpha_6)$ $-c_3[p_4\sin(\alpha_3)+p_3\sin(\alpha_4)+p_2\sin(\alpha_5)+p_1\sin(\alpha_6)]$
10	*JK*	$x=c_1\cos(\pi+\alpha_1)-(a+b)\cos(\alpha_1)/(1+\cos(\alpha_1))-(l-L_9)\cos(\alpha_5)$ $+c_3[p_4\cos(\alpha_3)+p_3\cos(\alpha_4)+p_2\cos(\alpha_5)]$ $y=c_1\sin(-\pi-\alpha_1)+(a+b)\sin(\alpha_1)/(1+\cos(\alpha_1))+(l-L_9)\sin(\alpha_5)$ $-c_3[p_4\sin(\alpha_3)+p_3\sin(\alpha_4)+p_2\sin(\alpha_5)]$
11	*KL*	$x=c_1\cos(\pi+\alpha_1)-(a+b)\cos(\alpha_1)/(1+\cos(\alpha_1))$ $-(l-L_{10})\cos(\alpha_4)+c_3[p_4\cos(\alpha_3)+p_3\cos(\alpha_4)]$ $x=c_1\sin(-\pi-\alpha_1)+(a+b)\sin(\alpha_1)/(1+\cos(\alpha_1))$ $+(l-L_{10})\sin(\alpha_4)-c_3[p_4\sin(\alpha_3)+p_3\sin(\alpha_4)]$
12	*LM*	$x=c_1\cos(\pi+\alpha_1)-(a+b)\cos(\alpha_1)/(1+\cos(\alpha_1))$ $-(l-L_{11})\cos(\alpha_3)+c_3p_4\cos(\alpha_3)$ $x=c_1\sin(-\pi-\alpha_1)+(a+b)\sin(\alpha_1)/(1+\cos(\alpha_1))$ $+(l-L_{11})\sin(\alpha_3)-c_3p_4\sin(\alpha_3)$
$\psi_1=\alpha_1+[(\alpha_2-\alpha_1)/L_1]$, $\psi_2=\alpha_2-[(\alpha_2-\alpha_1)(l-L_2)/(L_3-L_2)]$		

V. CONCLUSION

In this work, the waveguide array fed parabolic reflector antenna is investigated to obtain electronically switchable pencil beam and cosecant-squared patterns. For this aim, the waveguide array structure is parametrically analyzed, and the modified asymmetric reflector geometry is proposed.

The Analytical Regularization Method is used to compute the near field distribution of the waveguide array feeder and the radiation patterns of the designed parabolic reflector antenna.

Simulation results of the feeder analysis and its combination with the modified reflector are presented to demonstrate the suitability of the proposed antenna for microwave and millimeter wave air, naval and coastal surveillance radars.

ACKNOWLEDMENT

This work was supported by grant PIRSES-GA-2010-269157 (AMISS project) of EU 7th Framework Marie Curie Actions research fund.

REFERENCES

[1] C. F. Winter, "Dual Vertical Beam Properties of Doubly Curved Reflectors", *IEEE Trans. Antennas Propagation*, vol. 19, no. 2, 1971.

[2] Y. Rahmat-Samii "A comparison between GO/Aperture field and physical optics methods for offset reflectors", *IEEE Trans. Antennas Propagation*, vol. Ap-32, no. 3, pp. 301-306, 1984.

[3] D. Duan, Y. Rahmat-Samii "A generalized diffraction synthesis technique for high performance reflector antennas", *IEEE Trans. Antennas Prop.*, vol. 43, no. 1, pp. 27-40, 1995.

[4] G. A. Suedan, E. V. Jull, "Beam Diffraction by Planar and Parabolic Reflectors", *IEEE Trans. Antennas Propagation*, vol. 39, pp. 521-527, 1991.

[5] K. Tap, P. H. Pathak, "A fast hybrid asymptotic and numerical physical optics analysis of very large scanning cylindrical reflectors with stacked linear array feeds", *IEEE Trans. Antennas Propagation*, vol. 54, no. 4, pp. 1142-1151, 2006.

[6] S. L. Avila, W. P. Carpes Jr, J. A. Vasconcelos, "Optimization of an offset reflector antenna using genetic algorithms", *IEEE Trans. Magnetics*, vol. 40, no. 2, pp. 1256-1259, 2004.

[7] F. Arndt, J. Brandt, V. Catina, J. Ritter, I. Rullhusen, J. Dauelsberg, U. Hilgefort, W. Wessel, "Fast CAD and optimization of waveguide components and aperture antennas by hybrid MM/FE/MoM/FD methods: State of the art

and recent advances", *IEEE Trans. Mic. Theory Tech.*, vol. 52, no. 1, pp. 292-305, 2004.

[8] W. Ewe, L. Li, Q. Wu, M. Leong, "Analysis of reflector and horn antennas using adaptive integral methods", *IEICE Trans. Comm.*, vol. E88-B, no. 6, pp. 2327-2333, 2005.

[9] M. Djordjevic, B. M. Notaros, "Higher order hybrid method of moments-physical optics modeling technique for radiation and scattering from large perfectly conducting surfaces", *IEEE Trans. Antennas Prop.*, vol. 53, no. 2, pp. 800-813, 2005.

[10] A. S. Turk, "Analysis of aperture illumination and edge rolling effects for parabolic reflector antenna design", *International Journal of Electronics and Comm. (AEUE)*, vol. 60, pp. 257-266, 2006.

[11] K. Umashankar, A. Taflove, *Computational Electromagnetics*, Artech House, 1993.

[12] J. H. Wilkinson, *The Algebraic Eigenvalue Problem*, Clarendon Press, Oxford, 1965.

[13] C. A. J. Fletcher, *Computational Galerkin Method*, Springer- Verlag, Berlin, 1984.

[14] Y. A. Tuchkin, "Wave scattering by an open cylindrical screen of arbitrary profile with Dirichlet boundary value condition", *Soviet Physics Doclady*, vol. 30, pp. 1027-1030, 1985.

[15] Y. A. Tuchkin, E. Karacuha, A. S. Turk, "Analytical regularization method for E-polarized electromagnetic wave diffraction by arbitrary shaped cylindrical obstacles", *7th Int. Conf. Math. Methods Electromagnetic Theory*, pp. 733-735, Kharkov, Sept. 1998.

[16] E. Karacuha, A. S. Turk, "E-polarized scalar wave diffraction by perfectly conductive arbitrary shaped cylindrical obstacles with finite thickness", *Int. J. Infrared & Millimeter Waves*, vol. 22, pp. 1531-1546, 2001.

[17] M. Hashimoto, M. Idemen, O. A. Tretyakov, "*Analytical and Numerical Methods in Electromagnetic Wave Theory*", Science House Co., p. 202, 1992.

[18] A. S. Turk, O. Yurduseven, "Parametric analysis of multi-source feeding flare rolling and corrugating effects for H-plane horn radiator", *Applied Comp. Electromagnetic Society (ACES) Journal*, vol. 25, no. 11, pp. 990-997, 2010.

[19] A. S. Turk, O. Yurduseven, "Parametric design of parabolic reflector antenna with switchable cosecant-squared pattern", *Applied Comp. Electromagnetic Society (ACES) Journal*, Issue 6, vol. 26, pp. 494-501, 2011.

[20] A. S. Turk, O. M. Yucedag, "Parametric analysis of flare edge rolling throat bending and asymmetric flare effects for H-plane horn radiator", *International Journal of Electronics and Communication (AEUE)*, Issue 4, vol. 66, pp. 297-304, 2012.

Okan Mert Yucedag received the B.S. and M.S. degrees in Electronics Engineering from Uludag University, Bursa-Turkey in 2006 and 2009, respectively. He joined the Scientific and Technical Research Council of Turkey (TUBITAK) in 2007. He is currently working as senior researcher at TUBITAK Information Technologies Institute.

His research interests are microwave radar systems, antenna design, RCS estimation and numerical methods in electromagnetic wave scattering, especially method of moments and analytical regularization method.

Ahmet Serdar Turk received the B.S. degree in Electronics-Communication Engineering from Yildiz Technical University, Istanbul, Turkey in 1996. He received M.S. and Ph.D. degrees in Electronics Engineering from Gebze Institute of Technology, in 1998 and 2001, respectively. He joined the Scientific and Technical Research Council of Turkey (TUBITAK) in 1998. He is currently working as professor at Yildiz Technical University Electronics Engineering Department.

His research interests include horn, reflector, array and ultra-wide band antenna designs in RF and microwave bands, numerical methods in electromagnetic wave scattering, high frequency surface wave radar, ground penetrating radar, and microwave and millimeter wave radar systems.

Investigations on a Novel without Balun Modified Archimedean Spiral Antenna with Circularly Polarized Radiation Patterns

Balamurugan Shanmugam, and Satish K. Sharma

Department of Electrical and Computer Engineering
San Diego State University, 5500 Campanile Drive, San Diego, CA, USA, 92182-1309
Email: sbalamurugan9587@gmail.com and ssharma@mail.sdsu.edu

Abstract **—** The proposed novel modified two-layered Archimedean spiral (Mod Arspl) antenna achieves a simple feed without balun and maintains the antenna input impedance close to 50 Ω over extremely wide (10:1) frequency band for antenna design. It shows excellent impedance matching, higher peak gain and acceptable axial ratio over the operating frequencies compared to the conventional Archimedean spiral geometry on two-layers with the same aperture area. The working of this antenna and important design parameters to achieve frequency independent response with respect to matching and CP radiation patterns are discussed. The best case with free-space Mod Arspl has impedance BW (S_{11} < -10 dB) of 3.2-19.2 GHz (6:1 band), AR BW (AR < 3dB) of 3-20 GHz (6.6:1 band), stable broadside gain of 4-5.5 dBic and quasi-axial patterns in the usable 6:1 band. Radiation patterns show some beam squint towards higher frequency end attributed to spacing between the two layers of the spiral arms. The fabricated prototype antenna using microwave substrate shows CP operating BW over 5.21:1 frequency band (2.8 - 14.6 GHz) and peak gain varying between 4 - 8 dBic in this frequency band. Measured results show reasonable agreement with the simulated ones.

Index Terms **—** Archimedean spiral antenna, circular polarization, modified spiral antenna, two-layered spiral, without Balun spiral antenna.

I. INTRODUCTION

Frequency Independent characteristics of a Archimedean spiral (Arspl) antenna invented by J.A. Kaiser in 1960 are well known [1], [2] and explained qualitatively by radiating ring theory. Planar spiral antennas, being a self-complementary structure, have the real impedance of 188 Ω given by Mushiake equation in [3]. This necessitates the use of baluns for balanced-mode operation. Baluns limit the inherent frequency independent operation of spiral antennas and also increases the complexity. In [4] the authors eliminate the balun by employing a single arm spiral with disc/ground plane which has comparable performance with the two-arm spiral fed with balun except for the beam asymmetry and squint. In [5], the authors eliminate balun by reverting to unbalanced mode excitation with one of the spiral arms as a parasitic element. In [6] the authors propose a stripline fed Archimedean spiral by having a broadband impedance matching network conformal to spiral's windings to transform the input impedance of two-layered spiral to the impedance of stripline over 10:1 band. Although, not the focus of this paper, cavity backing for the proposed antenna was also implemented to achieve directional radiation patterns such as in in [7-8]. Similarly, the effect of dielectric loading, as reported in [9-10] was also performed, but not discussed here.

This paper investigates a two layered Archimedean spiral antenna which will be suitable for feeding with a 50 Ω coaxial line considering free space or foam substrate. The two-layered geometry with conventional Archimedean spiral design (referred as Arspl in this paper) is compared with the proposed two-layered geometry with modified Archimedean spiral design (referred as Mod Arspl) with the goal being the frequency independent response in terms of impedance matching, circular polarization (CP) at broadside angle and stable pattern with a balun-free coax

Submitted On: March 22, 2012
Accepted On: July 26, 2012

1054-4887 © 2012 ACES

excitation. Some preliminary investigation results of this antenna were presented in [11], and therefore, are not included here, for the sake of brevity. Since the proposed Arspl does not need a wideband balun or is quite simple to excite by a 50 Ohm SMA connector alone, hence it offers low cost and light weight implementation while still providing acceptable antenna performance. This can be acceptable for several communication applications, even if with some compromise in quality of the CP patterns.

Section I describes the configuration of Mod Arspl and compares its performance with the Arspl of the same diameter. The working of Mod Arspl is also explained. Section II discusses the important design parameters for achieving matching and stable CP radiation patterns. Section III presents the experimental results of Mod Arspl. Important findings are summarized in the conclusions section. The simulations are generated using Ansoft Corporations High Frequency Structure Simulator (HFSS) v12 which is a finite element method based full wave analysis tool.

II. MODIFIED ARSPL COMPARED TO CONVENTIONAL ARSPL

The top view of conventional two layered Arspl is shown in Fig. 1(a) whose configuration parameters are given in Table 1. The top spiral arms is at a height *h* from the bottom spiral as shown in Fig. 1(c) fed-in with a 50 Ω coaxial SMA connector. There is foam substrate (ε_r=1.06, tan δ=0.002) between the two spiral arms which is realizing the free space design. The radial distance from the center to any point on the arm is defined by the Archimedean function $r = a_{sp}\Phi_w$ where a_{sp} is the spiral constant and Φ_w is the winding angle varying between the starting angle Φ_{st} and ending angle Φ_{end}. The diameter of the spiral D is defined by $D = 2r_{max}$ with $r_{max} = a_{sp}\Phi_{end}$. The two layered Mod Arspl has double the arm width that of the Arspl and its top view is shown in Fig. 1(b). This modified geometry will create a short circuit or single conductor sheet if the spiral arms are kept at the same level. Its configuration parameters are given in Table I. The arm widths of Arspl and Mod Arspl are denoted as *W* and *AW*, respectively, with *AW* = 2*W*. The Mod Arspl has twice the growth rate or spiral constant (a_{sp}) and half the number of turns (*N*) as that of Arspl so that the aperture areas of both antennas remain the same.

The spiral arms of both the antennas are tapered at the ends to minimize the reflected current towards the feed. In case of Arspl, there are top and bottom circular stubs of diameter 1.2 mm and 4.8 mm, respectively, connecting the spiral arms to the SMA. Feed portion of Arspl is zoomed to show the top circular stub of 1.2 mm diameter (Fig. 1(c)). In comparison to this, the Mod Arspl has only a bottom stub of diameter 6.4 mm. A top circular stub of diameter 1.2 mm is used when the arm width of Arspl and Mod Arspl is less than or equal to 2 mm. Feed portion of Mod Arspl is zoomed in Fig. 1(d) to show the SMA feed and the circular stub of diameter 6.4 mm attached with the bottom spiral.

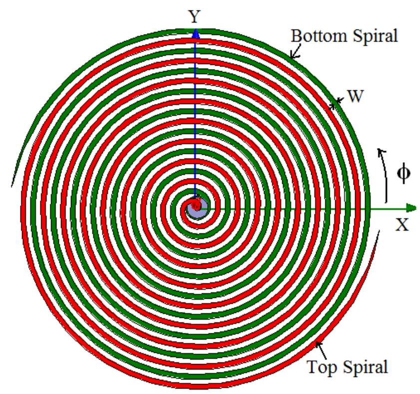

(a)

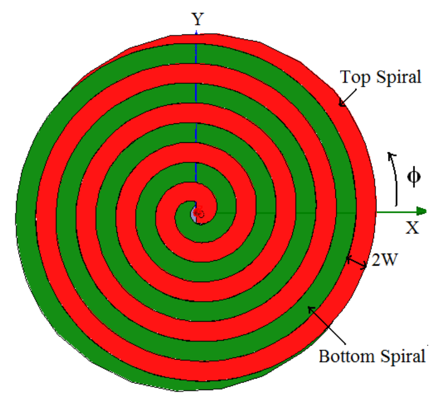

(b)

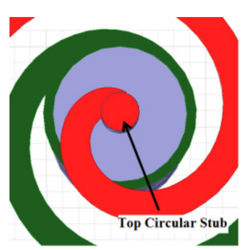

(c)

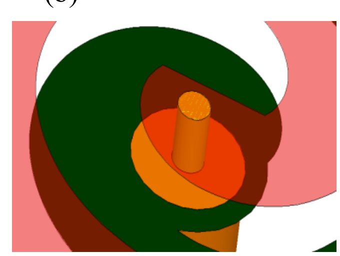

(d)

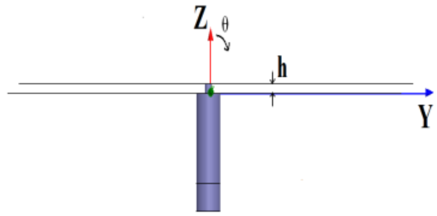

(e)

Fig. 1. Conventional and modified, two layered, Arspls (a) Top view of Arspl, (b) Top view of modified Arspl, (c) Feed portion of Arspl zoomed to show the top circular stub of 1.2 mm diameter, (d) Feed portion of Mod Arspl zoomed to show the SMA feed and the circular stub of diameter 6.4 mm attached with the bottom spiral, and (e) Side view of both Arspl and Mod Arspl.

Table 1: Antenna design parameters of the conventional and modified Archimedean spirals

Symbol	**Arspl**	**Mod Arspl**
Arm width	W = 2 mm	AW = 4 mm
h	1 mm	1 mm
a_{sp}	0.63 mm/rad	0.63 x 2 mm/rad
Φ_{st}	0.5π rad	0.5π rad
Φ_{end}	18.47π rad	18.47π/2 rad
N	9	4.5
D	73.1 mm	73.1 mm

The input impedance of conventional Arspl and Mod Arspl, both two layered, are plotted in Fig. 2. It can be inferred that the resistance (R_{in}) of Arspl varies between 25 - 150 Ω whereas for the Mod Arspl, it varies between 30 - 80 Ω which can be easily matched to a 50 Ω line. Also the input reactance X_{in} of the Mod Arspl is less oscillatory compared to the Arspl. The reason for this trend is explained in the next paragraph.

According to [3], a Self-Complementary Antenna (SCA) is one which leaves the geometry unchanged when the metal and blank spaces in a planar antenna are interchanged except for a rotation equal to one-half of its angular periodicity. Mushiake in [3] describes about both the planar (2D) as well as 3D self-complementary structures and their input impedance properties. Any self-complementary structure (2D or 3D) has a constant input impedance which is independent of frequency [3]. Theoretically, planar SCA have a constant input impedance of $Z_0/2$ (i.e. 188 Ω) and the planar two-arm conventional Archimedean spiral that is well known for the last 50 years is one such antenna. In trying to achieve a simple feed, the two layered design explored in this paper disturbs their planar SCA nature and the problem is now shifted to 3D which means that the Arspl will not have a constant impedance of around 170 Ω (Arspl has 25% of its area covered by metal on both top and bottom layer and its complement will have 75% of top and bottom layers covered by metal which is clearly not a SCA).

Therefore, the proposed Mod Arspl (Fig. 1(b)) is a 3D self complementary antenna with 50% of the area covered by metal on both top and bottom layers which makes its complement have the same 50% area covered by metal on both top and bottom but with a of rotation of 180^0. Here, the top and bottom spirals are 2D self-complementary structures by themselves and the antenna can be considered as two stacked 2D self-complementary structures with the impedance of each point of the structure given by 60π Ω as explained by [3]. Such a parallel arrangement of 2D structures each with 170 Ω impedance brings down the effective input impedance of the antenna to around 80 Ω (This is similar concept of having 2 parallel resistors of R ohms each which makes the total resistance R/2). This explains the input impedance of the Mod Arspl being fairly constant over frequency but at a lower value (average of around 55 Ω) compared to the 188 Ω for planar self-complementary structures. Fig. 3 shows the reflection coefficient magnitude versus frequency for the conventional two layered Arspl and the proposed Mod Arspl which shows a distinct improvement with the modified geometry and its reflection coefficient magnitude is better than -10 dB from 2-20 GHz w.r.t. a 50 Ω coaxial line.

The axial ratio (AR) at broadside angle ($\theta=0^o$) is plotted for both the antennas in Fig. 4 which shows that the axial ratio of the Mod Arspl is worse compared to Arspl at lower end of the band (2-4 GHz) due to the number of turns being halved which reduces coupling between the arms. This effect is seen throughout the band in the form of slightly increased AR and becomes more pronounced at the lower frequency end. The peak gain of both the antennas are plotted in Fig. 5

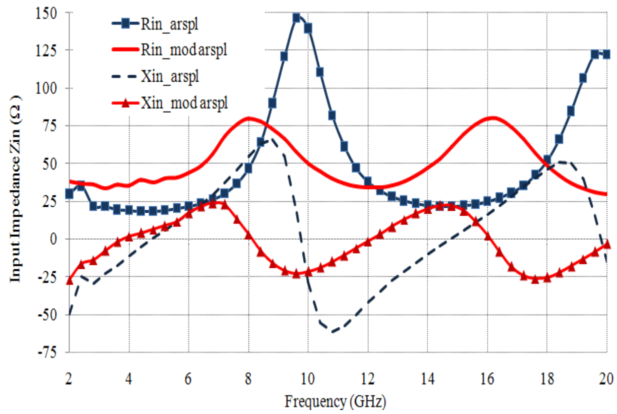

Fig. 2. Input impedance of Arspl and Mod Arspl.

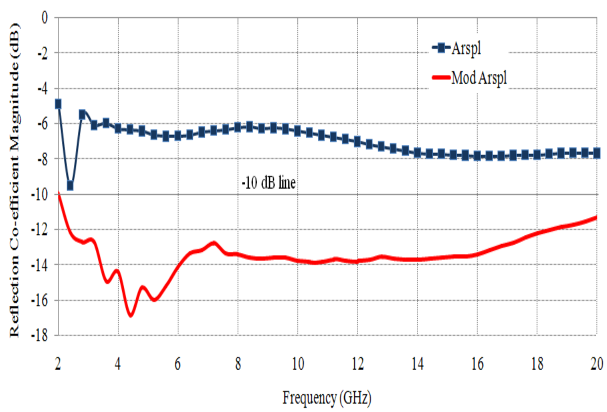

Fig. 3. Reflection coefficient magnitude versus frequency for Arspl and Mod Arspl.

which shows that the Mod Arspl has higher gain throughout the band.This increased gain can be partly attributed to the better impedance matching achieved and partly to the increased usage of metal instead of blank spaces (100% area covered with metal when seen from top instead of 50% in case of Arspl). This is a desired phenomenon since it partially achieves the purpose of cavity backing without increasing the antenna volume. The simulated left hand circular polarization (LHCP) and right hand circular polarization (RHCP) patterns of the Arspl and Mod Arspl are compared at different frequencies across the 2-20 GHz band in [6] and hence it is omitted here for the sake of brevity.

III. ANTENNA DESIGN PARAMETERS

Arm length is the length between the feed point and the arm end. The lower cut-off frequency for operating the spiral antennas as a CP antenna is denoted as f_L and upper cut-off frequency as f_U with the corresponding electrical wavelengths denoted as λ_L and λ_U. λ_g refers to guided wavelength. A spiral antenna radiates efficiently from a ring one wavelength in circumference according to band theory.

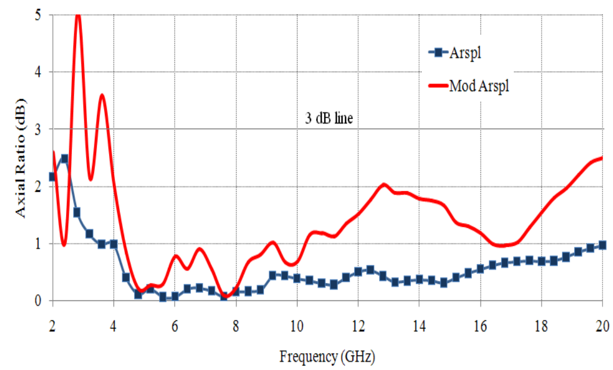

Fig. 4. Broadside axial ratio versus frequency for Arspl and Mod Arspl.

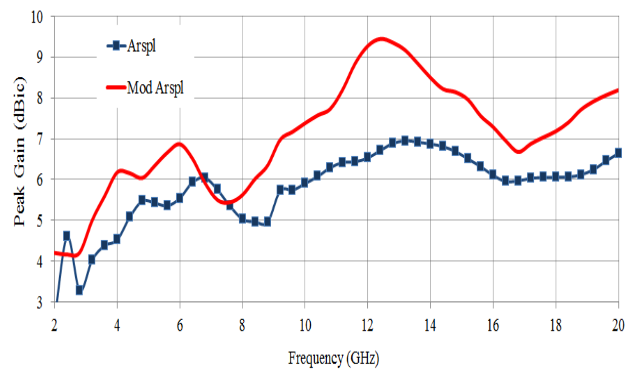

Fig. 5. Peak gain versus frequency for Arspl and Mod Arspl.

The conventional single layered spirals are designed to have a circumference equal to the desired λ_L. Most of the spiral designs reported in literature and also the commercial versions available exhibit better than 3-dB AR if the circumference of the spiral is atleast equal to one guided wavelength at the frequency of interest. These designs mostly have an arm width ranging from 0.5-2 mm which ensures that there are enough turns (and hence enough arm length of at least $4*\lambda_L$) within the same one wavelength circumference to create stronger coupling between the spiral arms thereby radiating most of the input energy as CP wave before it reaches the arm ends. The Mod Arspl constructed by doubling the arm width and halving the number of turns (compared to Arspl) within the same diameter is different in that aspect. Meeting the circumference requirement alone does not guarantee a CP radiation at that frequency and it requires a arm length of atleast (5-6)*λ_g as the current distribution is different from that of Arspl. Arm length depends on the number of turns N which inturn depends on the arm width *AW*. Arm length is the most important parameter that sets the lower cut-off frequency for the operation of Mod Arspl as a CP antenna.

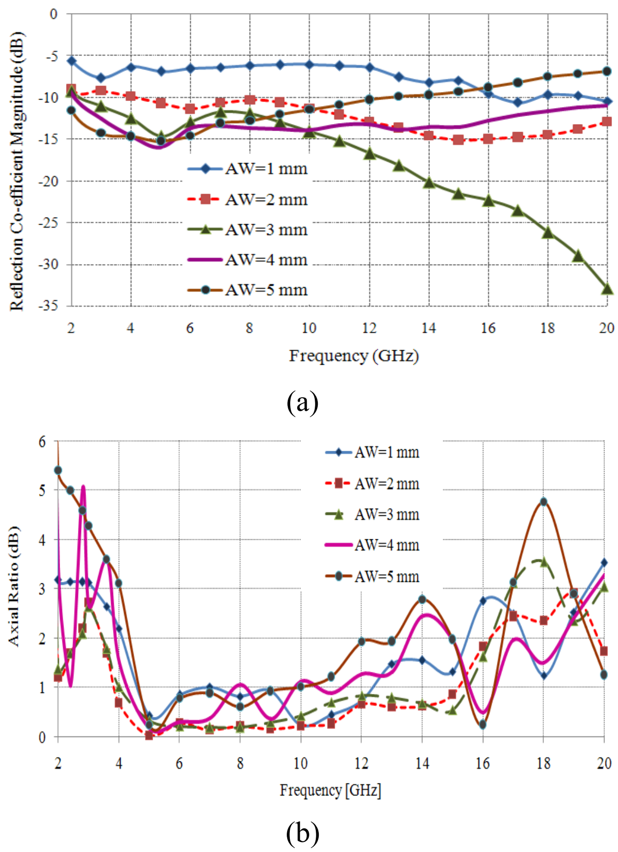

Fig. 6. Parametric studies showing the effect of *AW* on (a) reflection coefficient magnitude, and (b) broadside axial ratio.

Figure 6(a-b) shows the trend in impedance matching and axial ratio at broadside angle for varying the *AW* with h = 1 mm and D = 73.1 mm, respectively. Arm width equal or greater than 2 mm is recommended for these Mod Arspl designs as the smaller trace widths increase the antenna input impedance making it harder to match with SMA feed as it can be seen in the case of 1 mm *AW* in Fig. 6(a) showing poor impedance matching and a AR of greater than 3-dB at 3.5 GHz even with a arm length of 1920 mm. The impedance matching improves at low band (2-6 GHz) when the *AW* is increased from 1 to 5 mm but the higher frequenices (>12 GHz) are affected for *AW*>4 mm as seen in the 5 mm *AW* case. From Fig. 6(b), it can be inferred that the AR deteriorates at the low band till 4 GHz as the AW increases from 1 to 5 mm due to the decrease in arm length from 1920 mm to 340 mm. The AR BW starts from around 4 GHz for 4 and 5 mm AW as the arm length is 480 and 340 mm, respectively which is (5-6)*λg at 4 GHz. It can also be seen that 2 and 3 mm AW has an arm length of 960 (6.4*λg) and 720 mm (4.8*λg), respectively at 2 GHz which explains the AR BW starting before 2 GHz for these cases. For frequency independent antennas, only the lower cut-off frequency for AR BW is discussed because of the finite antenna geometry and the upper cut-off frequency depends on the accuracy of feed fabrication. In case of Mod Arspl, all the cases shown in Fig. 6(b) have an AR BW varying between 4:1 frequency band (*AW*=5 mm) and 10:1 frequency band (*AW*=2 mm). Ideally, a balun fed single layered spiral will have the impedance and AR BW starting from 1.4 GHz for a diameter of 73 mm. Based on the above discussion, the optimum arm width to operate the Mod Arspl will be from 2-3 mm which ensures that there is enough arm length to achieve CP at low band (2-4 GHz) and also maintain the impedance matching at these frequencies.

Though *AW* of 2-3 mm is the optimum, the level of impedance matching achieved throughout the 2-20 GHz band with 4 mm *AW* case compelled the authors to study the effect of height h with *AW*=4 mm which has AR BW from 4-20 GHz. A discussion of important parameter (h - separation of spiral arms) that affects the pattern quality is discussed in the coming paragraphs and Fig. 8. The impedance matching, axial ratio at broadside angle and CP gain at broadside angle for different cases varying the height h from 0.8-3.2 mm with *AW*=4 mm and D=73.1 mm are shown in Fig. 7(a-c), respectively. The AR BW remains fairly constant for all the cases (Fig. 7(b)) but the impedance BW reduces from 10:1 to 5:1 frequency band as the height is increased from 0.8-3.2 mm (Fig. 7(a)). This is due to the added inductance of the probe with increasing height of the center pin between the two spirals that lowers the matching level and therefore a maximum height of 3.2 mm is recommended.

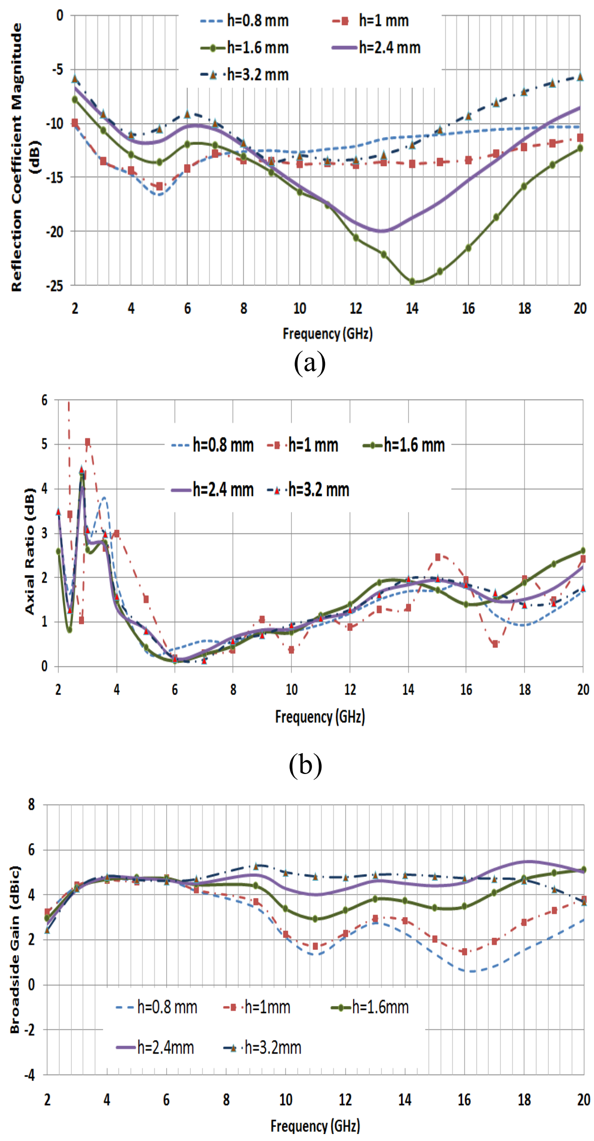

Fig. 7. Parametric studies showing the effect of *h* when *AW*=4mm and *D*=73.1mm on (a) reflection coefficient magnitude, (b) axial ratio at broadside angle, and (c) CP gain at broadside angle.

The most notable effect of increasing the separation between the spiral arms can be found in Fig. 7(c) which shows that the CP gain at broadside angle stays constant around 4-5 dBic from 3-18 GHz with increased spacing (*h*=2.4 and 3.2 mm) whereas for smaller spacing (*h*=0.8, 1, 1.6 mm cases) the broadside gain drops with increasing frequency.

The above perfromance can be explained from the radiation patterns plotted at different frequencies across the 3-18 GHz band in Fig. 8 for *h*=0.8 mm and 2.4 mm cases which show that the magnitude of back radiation is reduced throughout the band with *h*=2.4 mm case and the beam is pushed to the front, thereby, increasing the broadside gain at all frequencies. The bottom spiral and its stub acts as a partial reflector pushing the beam towards broadside angle if the spacing between the spirals is greater than 0.02λ. The broadside gain is therefore held constant even though the beam peak is not exactly at broadside angle. Note that the patterns of *h*=2.4 mm case are usable from 3-18 GHz as shown in Fig. 8. A spacing of 1.6-3.2 mm is recommended to achieve a frequency independent response with respect to impedance matching and gain at broadside angle for Mod Arspl. The pattern asymmetry and squint is solely due to the spiral arms being kept at different levels. Based on the above discussion, it can be concluded that the arm width and spiral diameter determines the AR BW whereas the impedance BW and pattern/gain stability depends on the spacing between the spiral arms. The best case with *AW*=4 mm, *h*=2.4 mm and *D*=73.1 mm has an impedance BW of 3.2-19.2 GHz (6:1 band), AR BW of 3-20 GHz (6.6:1 band), stable gain of 4-5.5 dBic at broadside angle with usable quasi-axial patterns throughout the 6:1 band.

IV. MOD ARSPL - EXPERIMENTAL VERIFICATION

The simulation results presented in the previous sections are based on using the foam substrate, which require hand fabrication. This method is prone to fabrication errors because it involves curved configuration. Considering this and to provide further practical significance to the spiral design, the Mod Arspl was redesigned on a low loss Rogers 5880 (ε_r = 2.2) substrate material and consequently, fabricated using a LPKF CAD milling machine which ensures fabrication accuracy.

Freq	***h*=0.8mm**	***h*=2.4 mm**
3 GHz Gain LHCP Phi=0 Gain LHCP Phi=90 Gain RHCP Phi=0 Gain RHCP Phi=90	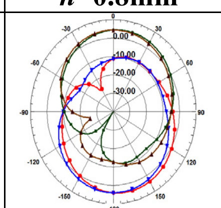	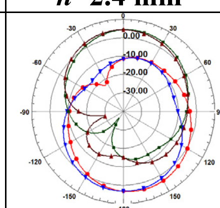

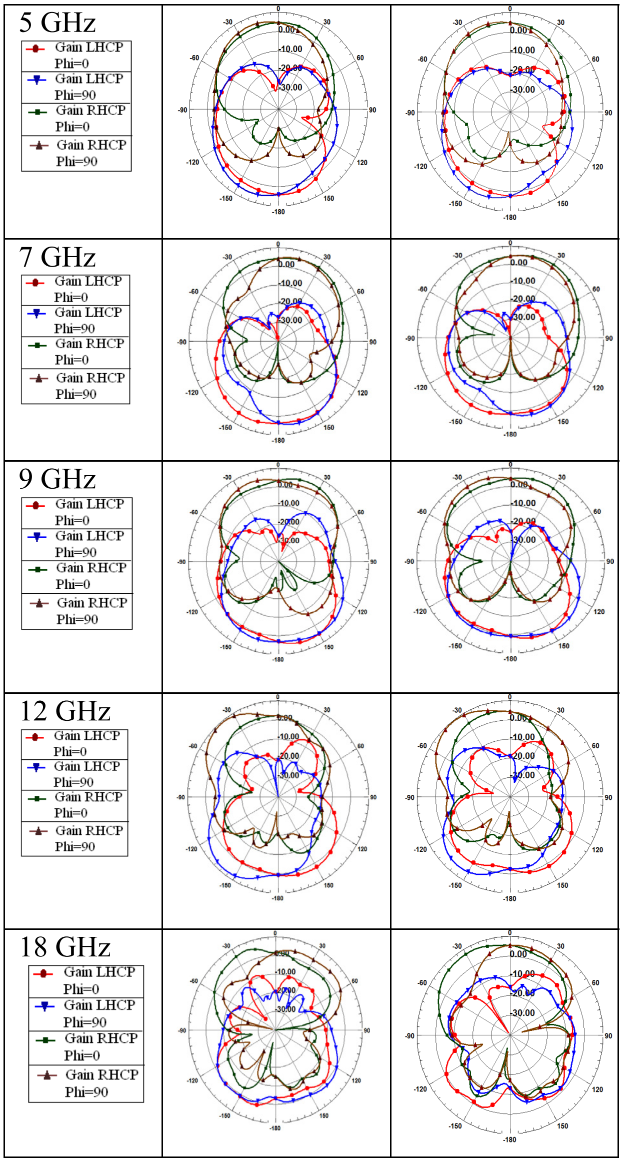

Fig. 8. Comparison of radiation patterns for cases *h*=0.8 and 2.4 mm to show the effect of reduced back radiation as the arm separation increases.

The parameters of the fabricated spiral are $AW = 4$ mm, $h = 1.6$ mm, $D = 73.1$ mm. The substrate is square shaped instead of circular shape used in the previous sections as shown in the photograph of fabricated prototype antenna in Fig. 9 which has the total dimensions 77 x 77 x 1.6 mm^3. The antenna is experimentally verified in the Antenna and Microwave Lab (AML) at SDSU which are also compared with the corresponding simulated data. The VSWR and broadside axial ratio are plotted versus frequency for the simulated and measured data in Fig. 10(a-b), respectively.

(a)

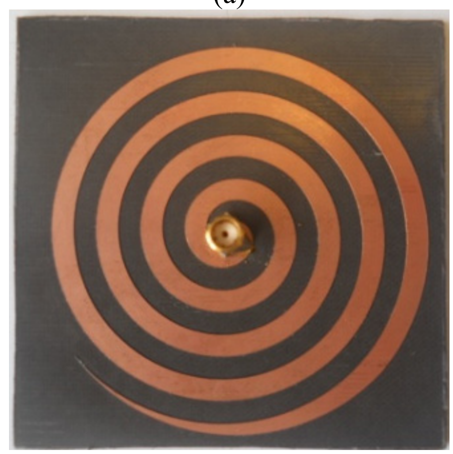

(b)

Fig. 9. Photograph of the fabricated prototype of Mod Arspl using the microwave substrate (a) top view, and (b) antenna as seen from bottom showing SMA feed.

The measured and simulated impedance BWs are from 1.6 to almost 15 GHz (frequency ratio = 9.375:1) as shown in Fig. 10(a). The measured AR, gain and patterns are obtained from analysis software purchased from Orbit/FR which computes the AR and radiation patterns from the measured linear patterns. The measured and simulated AR BWs are from 2.8 to 14.6 GHz (frequency ratio = 5.21:1) as shown in Fig. 10(b). The usable BW is defined as the common frequency range between the impedance and AR BWs which is also from 2.8 to 14.6 GHz (frequency ratio = 5.21:1 band). The simulated and measured LHCP and RHCP radiation patterns at different frequencies over the band are shown in Fig. 11 for $\phi = 0^o$, and 90^o cut planes. It can be observed that as frequency approaches the higher end, the patterns show some beam scan.

The measured and simulated CP peak gain varies from around 4 - 8 dBic in the usable band.

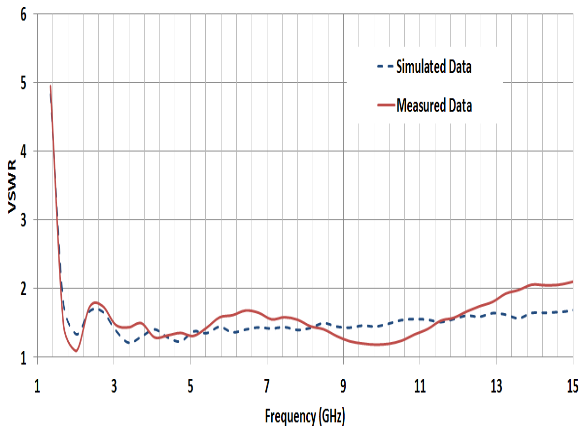

(a)

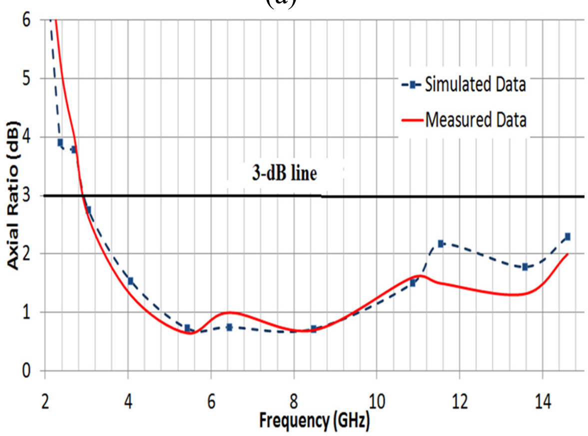

(b)

Fig. 10. Simulated and measured frequency response of a) VSWR, b) Axial ratio at broadside angle for the Mod Arspl on the microwave substrate.

It should be noted that the free-space based design discussed in the previous section offers over 6:1 usable band but the fabricated design on Rogers 5880 substrate with the same design parameters (only exception being the usage of 1.6 mm substrate thickness instead of 2.4 mm thickness) does not show same superior performance because the design parameters are not re-optimized on Rogers 5880.

V. CONCLUSIONS

This paper presented a novel antenna geometry called the modified two-layered Archimedean spiral antenna (Mod Arspl) with simple SMA feed without balun which shows improved performance in impedance matching and peak gain with a slight compromise in axial ratio BW compared to the two-layered design of the conventional Archimedean spiral (Arspl) geometry with the same aperture area. The best case with free-space or foam based Mod Arspl has impedance BW of 3.2-19.2 GHz (6:1 band), AR BW of 3-20 GHz (6.6:1 band), and broadside gain of 4-5.5 dBic in the usable 6:1 band. Radiation patterns show some beam squint as higher frequency end is approached which is attributed to the spacing *h*. The fabricated prototype on a microwave substrate has CP usable band from 2.8 - 14.6 GHz (5.21:1 band) with peak gain varying between 4-8 dBic. Measured results show reasonable agreement with the simulated ones.

Freq (GHz)	Phi=0 deg Simulated RHCP Measured RHCP Simulated LHCP Measured LHCP	Phi=90 deg Simulated RHCP Measured RHCP Simulated LHCP Measured LHCP
3.04 GHz	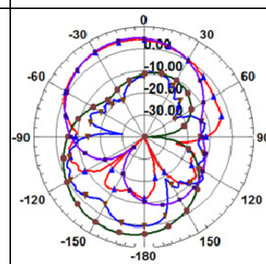	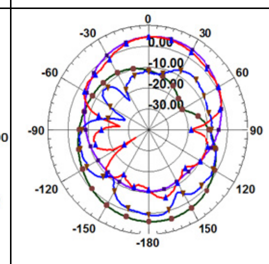
5.08 GHz	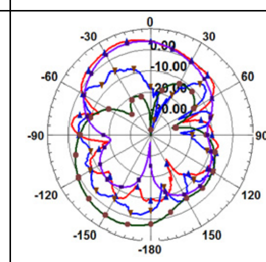	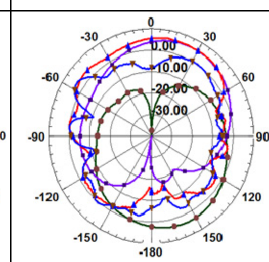
7.46 GHz	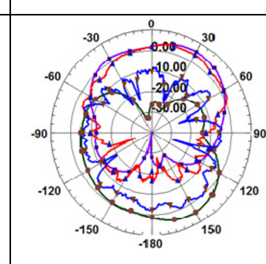	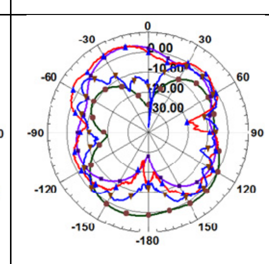

9.16 GHz	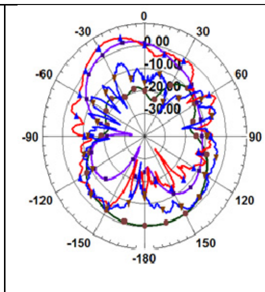	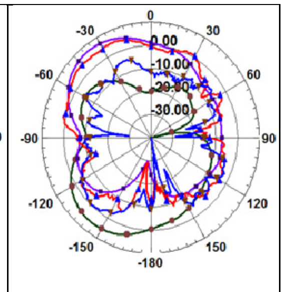
11.54 GHz	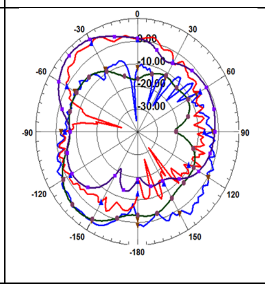	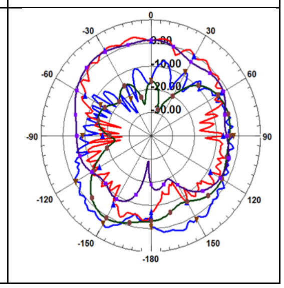

Fig. 11. Simulated and measured LHCP and RHCP radiation patterns for the Mod Arspl fabricated on the microwave substrate at different frequencies.

ACKNOWLEDGMENT

This work was carried out under the National Science Foundation (NSF)'s CAREER grant # ECCS-0845822.

REFERENCES

[1] J. A. Kaiser, "The Archimedean two-wire spiral antenna", *IRE Trans. Antennas Propag.*, vol. AP-8, no. 3, pp. 312-323, May 1960.

[2] J. Volakis, "Antenna Engineering Handbook", San Francisco, CA: Mc-Graw Hill, 2007.

[3] Y. Mushiake, "Self-Complementary Antennas," *IEEE Antennas and Propagation Magazine*, vol. 34, no. 6, Dec. 1992, pp. 23-29.

[4] H. Nakano, and R. Satake, "Extremely low-profile, single-arm wideband spiral antenna radiating a circularly polarized wave", *IEEE Trans. Antennas Propag.*, vol. 58, no. 5, May 2010.

[5] H. Nakano, T. Igarashi, H. Oyanagi, Y. Iitsuka, and J. Yamauchi, "Un-balanced mode spiral antenna backed by an extremely shallow cavity", *IEEE Trans. Antennas Propag.*, vol. 57, no. 6, pp. 1625-1633, Jun 2009.

[6] Teng-Kai Chen and G.H. Huff, "Stripline-Fed Archimedean Spiral Antenna," *IEEE Antennas and Wireless Propagation Letters,* vol. 10, pp. 346-349, 2011.

[7] N. Rahman, A. Sharma, M. Asfar, S. Palreddy, and R. Cheung, "Dielectric Characterization and Optimization of Wide-band, Cavity-Backed Spiral Antennas," *Applied Computational Electromagnetics Society (ACES) Journal,* vol. 26, no. 2, pp. 123-130, February 2011.

[8] S. Palreddy, A. I. Zaghoul, and R. Cheung, "Study of the Effects of the Back Cavity on a Broadband Sinuous Antenna and an Optimized Loaded Back Cavity," *Applied Computational Electromagnetics Society (ACES) Journal*, vol. 26, no. 8, pp. 660-666, August 2011.

[9] S. K. Khamas, G. G. Cook, "Optimized Design of a Printed Elliptical Spiral Antenna with a Dielectric Superstrate," *Applied Computational Electromagnetics Society (ACES) Journal*, vol. 23, no. 4, pp. 345-351, December 2008.

[10] C. Fumeaux, D. Baumann, R. Vahldieck, "FVTD Characterization of Substrate Effects for Archimedean Spiral Antennas in Planar and Conformal Configurations," *Applied Computational Electromagnetics Society (ACES) Journal,* vol. 20, no. 3, pp. 186-197, November 2005.

[11] B. Shanmugam, and S. K. Sharma, "Investigations on a novel modified Archimedean spiral antenna," IEEE *Antennas and Propagation International Symposium*, pp. 1225-1228, 3-8 July 2011.

Satish Kumar Sharma received his Ph. D. degree from the Institute of Technology, Banaras Hindu University, in 1997 in Electronics Engineering. From December 1993 to February 1999, he was a Research Scholar in the Department of Electronics Engineering, Institute of Technology, Banaras Hindu University. From March 1999 to April 2001, he was a Postdoctoral Fellow in the Department of Electrical and Computer Engineering, University of Manitoba. He was a Senior Antenna Engineer with InfoMagnetics Technologies Corporation in Winnipeg, Canada, from May 2001 to August 2006. Simultaneously, he was also a Research Associate at the University of Manitoba from June 2001 to August 2006. In August 2006, he joined San Diego State University (SDSU) as an Assistant Professor in the Department of Electrical and Computer Engineering. Since August 2010, he is an Associate Professor at SDSU. Dr. Sharma received the National Science Foundation's prestigious faculty early development (CAREER) award in 2009. Currently, he serves as an Associate Editor of the IEEE Transaction on Antennas and Propagation journal. He is a full member of the USNC/URSI, Commission B, Senior Member of the IEEE (Antennas and Propagation Society) and a Member of ACES since year 2010.

Enhanced Bandwidth of Small Square Monopole Antenna by using Inverted U-shaped Slot and Conductor-Backed Plane

N. Ojaroudi [1], M. Ojaroudi [2], and Sh. Amiri [3]

[1] Faculty of Electrical & Computer Engineering
Shahid Rajaee Teacher Training University, Tehran, Iran
n_ojaroudi@srttu.edu

[2] Young Research Group
Ardabil Branch, Islamic Azad University, Ardabil, Iran
m.ojaroudi@iauardabil.ac.ir

[3] Scientific Member of Electrical Engineering, Department of Iranian Research Organization for Science and Technology (IROST), Tehran, Iran
amiri@irost.org

Abstract **─**This paper, presents a novel multi-resonance monopole antenna for ultra wideband applications. The proposed antenna consists of a square radiating patch with an inverted U-shaped slot and a ground plane with an inverted U-shaped conductor-backed plane, which leads to a wide usable fractional bandwidth of more than 135% (2.9-15.1 GHz). By cutting a modified inverted U-shaped slot with variable dimensions on the radiating patch and also by inserting an inverted U-shaped conductor-backed plane, additional resonances are excited and hence much wider impedance bandwidth can be produced, especially at the higher band. The designed antenna has a small size of 12×18 mm^2, or about $0.15\lambda \times 0.25\lambda$ at 4.2 GHz (the first resonance frequency). Simulated and experimental results obtained for this antenna show that it exhibits good radiation behavior within the UWB frequency range.

Index Terms- Square Monopole Antenna, Inverted U-Shaped Structure, Ultra Wide-Band Systems.

I. INTRODUCTION

Commercial UWB systems require small low-cost antennas with omnidirectional radiation patterns and large bandwidth [1]. It is a well-known fact that planar monopole antennas present really appealing physical features, such as simple structure, small size and low cost. Due to all these interesting characteristics, planar monopoles are extremely attractive to be used in emerging UWB applications, and growing research activity is being focused on them.

In UWB communication systems, one of key issues is the design of a compact antenna while providing wideband characteristic over the whole operating band. Consequently, several planar monopoles with different geometries have been experimentally characterized [2]-[3] and automatic design methods have been developed to achieve the optimum planar shape [4]-[5]. Moreover, other strategies to improve the impedance bandwidth have been investigated [6]-[8].

This paper focuses on a square monopole antenna for UWB applications, which combines the square-patch approach with an inverted U-shaped slot, and the ground plane with an inverted U-shaped conductor backed plane that achieves a fractional bandwidth of more than 135%. Three new small wideband printed monopole antennas were proposed in [6-8], in

Submitted On: Mar. 8, 2012
Accepted On: July 22, 2012

which in order to achieve the maximum impedance bandwidth, inverted T-shaped, rectangular, and trapezoid notches were etched on the upper edge of the ground plane, respectively, where as in this letter to achieve the same goal, for the first time, an inverted U-shaped conductor backed plane is inserted in the feed gap distance and there is no notch on the ground plane (this structure has an ordinary rectangular ground plane configuration). Moreover, by cutting a modified inverted U-shaped slot with variable dimensions on the radiating patch, additional resonances (third and fourth resonances) are excited, which results in an increase in the usable upper frequency of the monopole and extends it from 10.3 GHz to 15.1 GHz. The designed antenna has a small size of 12×18 mm^2, and the impedance bandwidth of the designed antenna is higher than the UWB antennas reported recently [2-8].

II. ANTENNA DESIGN

The square monopole antenna fed by a microstrip line is shown in Fig. 1, which is printed on a FR4 substrate of thickness 1.6 mm, permittivity 4.4, and loss tangent 0.018. The width W_f of the microstrip feedline is fixed at 2 mm. The basic antenna structure consists of a square patch, a feedline, and a ground plane. The square patch has a width of W. The patch is connected to a feed line with the width of W_f and the length of L_f. On the other side of the substrate, a conducting ground plane is placed. The proposed antenna is connected to a 50-Ω SMA connector for signal transmission.

To design a novel antenna, an inverted U-shaped slot and an inverted U-shaped conductor-backed plane are embedded on the basic antenna structure, mentioned above. Based on the current distribution analysis, in UWB frequency band, it is observed that the currents on the bottom edge of the monopole's radiating patch, are distributed vertically at lower frequencies, while at higher frequencies this currents are distributed horizontally [9]. By cutting the inverted U-shaped notch of suitable dimensions (W_C, L_C, W_{C1} and L_{C1}) on the square radiating patch, it is found that much enhanced impedance bandwidth can be achieved for the proposed antenna.

In addition, the conductor-backed plane is playing an important role in the broadband characteristics of this antenna, because it can adjust the electromagnetic coupling effects between the patch and the ground plane, and improves its impedance bandwidth without any cost of size or expense [10]-[11]. This phenomenon occurs because, with the use of a conductor-backed plane structure in air gap distance, additional coupling is introduced between the bottom edge of the square patch and the ground plane [5].

In this work, we start by choosing the dimensions of the designed antenna. These parameters, including the substrate, is $L_{Sub}\times W_{Sub} = 12mm\times18mm$, or about $0.15\lambda \times 0.25\lambda$ at 4.2 GHz (the first resonance frequency). We have a lot of flexibility in choosing the width of the radiating patch. This parameter mostly affects the antenna bandwidth. As W decreases, so does the antenna bandwidth, and vice versa. Next step, we have to determine the The length of the radiating patch L. This parameter is approximately $\frac{\lambda_{lower}}{4}$, where λ_{lower} is the lower bandwidth frequency wavelength. λ_S depends on a number of parameters such as the slot width as well as the thickness and dielectric constant of the substrate on which the slot is fabricated. The last and final step in the design is to choose the length of the resonator (slot and conductor backed plane). L_r is set to resonate at $0.25\lambda_g$, where $L_r = W_C + 2L_C$ for slot, and $L_r = W_C + 2L_C$ for conductor backed plane, λ_g corresponds to resonance frequency wavelength.

The final dimensions of the designed antenna are as follows: $W_{sub} = 12mm$, $L_{sub} = 18mm$, $h_{sub} = 1.6mm$, $W = 10mm$, $L = 10mm$, $W_f = 2mm$, $L_f = 7mm$, $W_C = 4mm$, $L_C = 3mm$, $W_{C1} = 1mm$, $L_{C1} = 2mm$, $W_P = 9mm$, $L_P = 3.75mm$, $W_{P1} = 2.5mm$, $L_{P1} = 2.5mm$,

$L_{d1} = 0.75mm$, $W_{d1} = 1.5mm$, $d_{PS} = 2.75mm$ and $L_{gnd} = 3.5mm$.

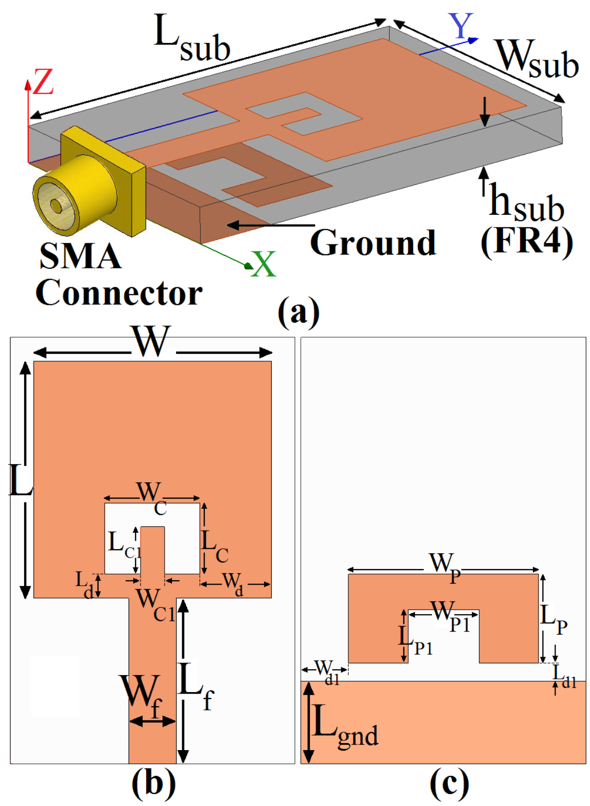

Fig. 1. Geometry of proposed antenna with inverted U-shaped slot and conductor-backed plane, (a) side view, (b) square radiating patch, and (c) ground plane structure.

III. RESULTS AND DISCUSSIONS

In this Section, the planar monopole antenna with various design parameters were constructed, and the numerical and experimental results of the input impedance and radiation characteristics are presented and discussed. The parameters of this proposed antenna are studied by changing one parameter at a time, while others are fixed. The simulated results are obtained using the Ansoft simulation software high-frequency structure simulator (HFSS) [12].

Figure 2 shows the structure of various antennas used for simulation studies. Return loss characteristics for ordinary square patch antennas (Fig. 2(a)), with an inverted U-shaped slot (Fig. 2(b)), and with inverted U-shaped slot and conductor-backed plane (Fig. 2(c)) are compared in Fig 3. As shown in Figure 3, it is observed that by using these modified elements including an inverted U-shaped slot etched on the radiating patch and inserting an inverted U-shaped conductor-backed plane on the other side of substrate, additional third and fourth resonances are excited respectively, and hence the bandwidth is increased.

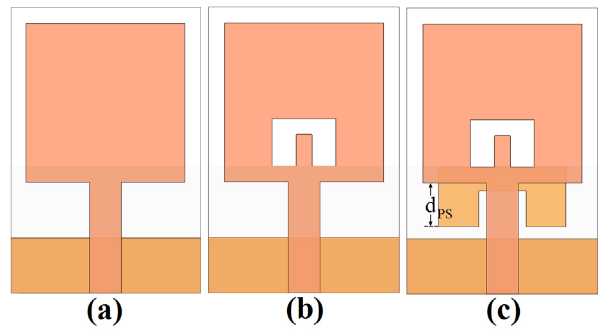

Fig. 2. (a) The ordinary square antenna, (b) the square antenna with inverted U-shaped slot (c) the square antenna with inverted U-shaped slot and parasitic structures.

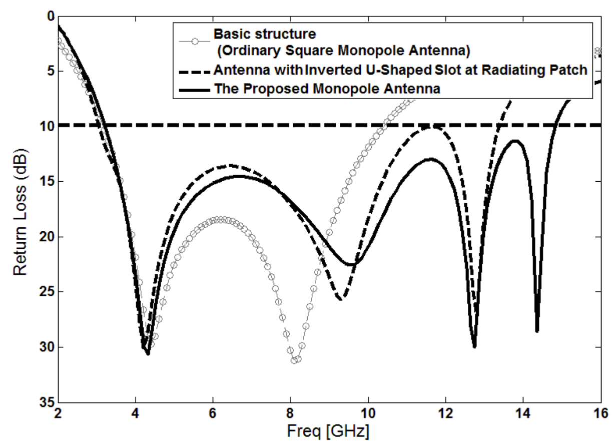

Fig. 3. Simulated return loss characteristics for the antennas shown in Fig. 2.

As shown in Fig. 3, in the proposed antenna configuration, the ordinary square monopole can provide the fundamental and next higher resonant radiation band at 4 and 8 GHz, respectively, in the absence of the inverted U-shaped slot and conductor-backed plane. Also Smith Chart demonstration of the input impedance of various monopole antenna structures, which were studied as Fig. 3, is shown in Fig. 4.

The upper frequency bandwidth is significantly affected by the use of the inverted U-shaped slot on the radiating patch. This behavior is mainly due to the change of surface

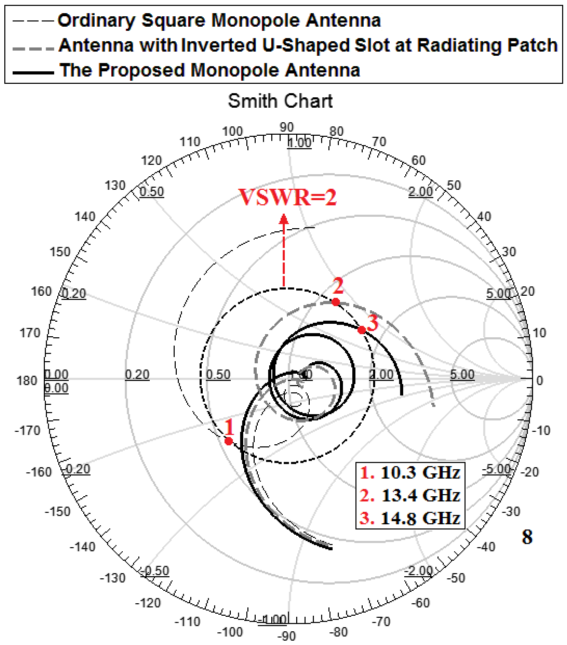

Fig. 4. Smith chart demonstration of the simulated input impedance of various monopole antenna structures, shown in Fig. 2.

current path which depends on the dimensions of inverted U-shaped slot as shown in Fig. 5 (a). In addition, by inserting the inverted U-shaped conductor-backed plane on the other side of substrate, the impedance bandwidth is effectively improved at the upper frequency [6]. The inverted U-shaped conductor backed plane can be regarded as a parasitic resonator that is electrically coupled to the square monopole.

As shown in Fig. 5(b), at fourth resonance frequency (14.3 GHz), the current is mainly concentrated on the interior and exterior edges of the inverted U-shaped conductor-backed plane. This figure shows that the electrical current for the fourth resonance frequency (Fig. 5 (b)) does change direction along the bottom edge of the square radiating patch and changes the antenna impedance at this frequency, as leads to an increase in the radiating power and bandwidth. Also there will be an increase in radiation efficiency. However, the resonant resistance is decreased [9].

By properly tuning the dimensions and spacing d_{PS} to semi-ground plane for the inverted U-shaped conductor backed plane, the antenna can create the fourth resonant frequency in individual resonant radiation band based on an over-coupling condition. Figure 6 shows the effects of the feed gap distance d_{PS} (as shown Fig. 2, $d_{PS} = L_f - L_{gnd} - L_{d1}$) of the square patch and dimension of the inverted U-shaped conductor-backed plane on the impedance. As illustrated in Fig. 6, the feed gap distance d_{PS} is an important parameter in determining the sensitivity of impedance matching. By adjusting d_{PS}, the electromagnetic coupling between the bottom edge of the square patch and the ground plane can be properly controlled [6].

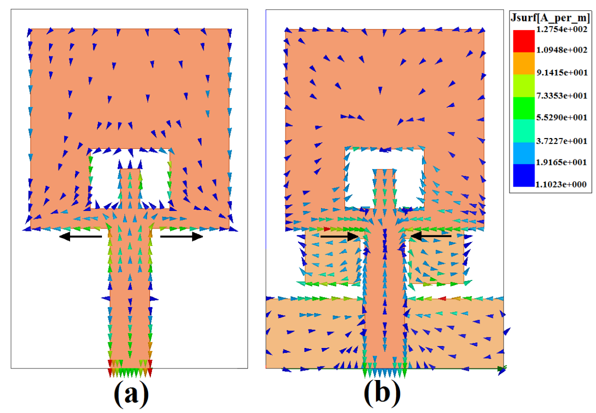

Fig. 5. Simulated surface current distributions on the radiating patch and ground plane for (a) the square antenna with inverted U-shaped slot at third resonance frequency (12.5 GHz), (b) the square antenna with inverted U-shaped slot and parasitic structure at fourth resonance frequency (14.3 GHz).

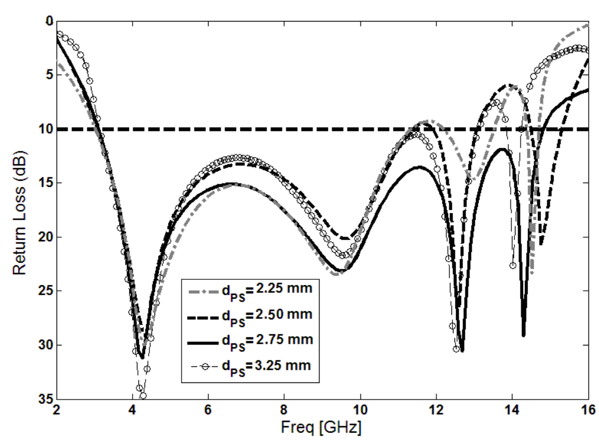

Fig. 6. Simulated return loss characteristics for various values of d_{PS}.

Figure 7 shows the measured and simulated return loss characteristics of the proposed antenna. The fabricated antenna satisfies the 10-dB return loss requirement from 2.91 to 15.1 GHz. As shown in Fig. 7, there exists a discrepancy between measured data and the simulated results this could be due to the effect of the SMA port. In order to confirm the accurate return loss characteristics for the designed antenna, it is recommended that the manufacturing and measurement processes need to be performed carefully.

Figure 8 shows the measured radiation patterns at resonances frequencies including the co-polarization and cross-polarization in the *H*-plane (*x-z* plane) and *E*-plane (*y-z* plane). The main purpose of the radiation patterns is to demonstrate that the antenna actually radiates over a wide frequency band. It can be seen that the radiation patterns in *x-z* plane are nearly omnidirectional for all the four frequencies.

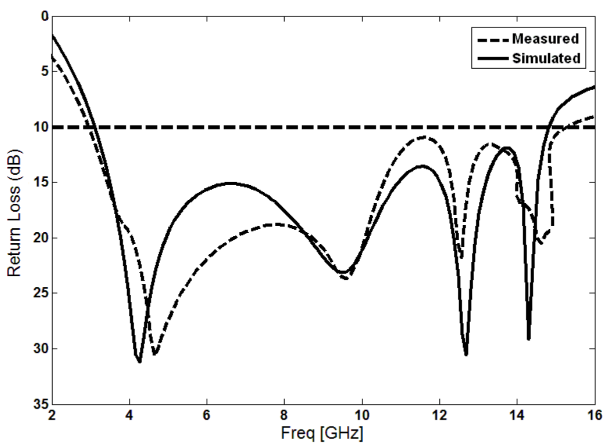

Fig. 7. Measured and simulated return loss characteristics for the proposed antenna.

V. CONCLUSION

In this letter, a novel compact Printed Monopole Antenna (PMA) has been proposed for UWB applications. The fabricated antenna satisfies the 10-dB return loss requirement from 2.9 to 15.1 GHz. By cutting a modified inverted U-shaped slot with variable dimensions on the radiating patch and also by inserting an inverted U-shaped conductor-backed plane, additional resonances are excited and hence much wider impedance

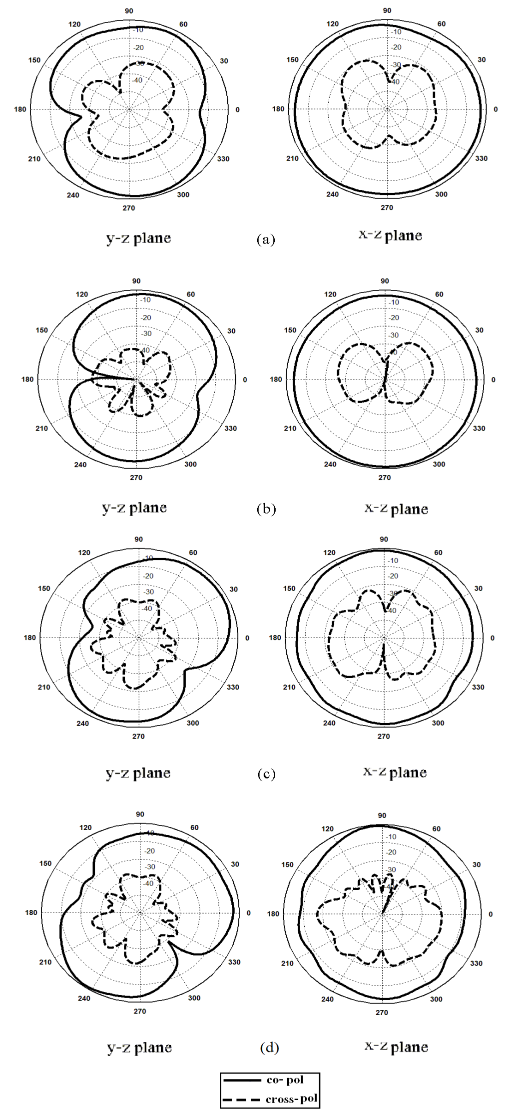

Fig. 8. Measured radiation patterns of the proposed antenna, (a) 4GHz, (b) 8GHz, (c) 12.7 GHz, and (c) 14.5 GHz.

bandwidth can be produced, especially at the higher band. The proposed antenna has a simple configuration and is easy to fabricate. Experimental results show that the proposed antenna could be a good candidate for UWB application.

ACKNOWLEDGMENT

The authors are thankful to Microwave Technology (MWT) Company staff for their beneficial and professional help (www.microwave-technology.com).

REFERENCES

[1] Schantz H., The Art and Science of Ultra wideband antennas, Artech House 2005.

[2] Ammann M. J., Impedance bandwidth of the square planar monopole, *Microwave and Optical Tech. Letters*, vol. 24, no. 3, February 2000.

[3] R. Azim, M. T. Islam, N. Misran, "Design of a Planar UWB Antenna with New Band Enhancement Technique," *Applied Computational Electromagnetic Society (ACES) Journal*, vol. 26, no. 10, pp. 856-862, October 2011.

[4] D. S. Javan, O. H. Ghouchani, "Cross Slot Antenna with U-Shaped Tuning Stub for Ultra Wideband Applications," *Applied Computational Electromagnetic Society (ACES) Journal*, vol. 24, no. 4, pp. 427-432, August 2009.

[5] Suh S. Y., Stutzman W. L., Davis W. A., A new ultrawideband printed monopole antenna: the planar inverted cone antenna (PICA), *IEEE Trans. Antennas Propagat.*, vol. 52, no. 5, pp. 1361-1364, May 2004.

[6] Kerkhoff A. J., Rogers R. L., Ling H., Design and Analysis of Planar Monopole Antennas Using a Genetic Algorithm Approach, *IEEE Trans. Antennas Propagat.,* vol. 2, pp. 1768-1771, June 2004.

[7] M. Ojaroudi, G. Kohneshahri, and Ja. Noory, "small modified monopole antenna for UWB application," *IET Microw, Antennas Propag*, vol. 3, no. 5, pp. 863-869, August. 2009.

[8] M. Ojaroudi, Ch. Ghobadi, and J. Nourinia, "Small Square Monopole Antenna With Inverted T-Shaped Notch in the Ground Plane for UWB Application," *IEEE* Antennas and Wireless Propagation *Letters*, vol. 8, no. 1, pp. 728-731, 2009.

[9] M. Ojaroudi, Gh. Ghanbari, N. Ojaroudi, and Ch. Ghobadi, "Small Square Monopole Antenna for UWB Applications with Variable Frequency Band-Notch Function," *IEEE* Antennas and Wireless Propagation *Letters*, vol. 8, pp. 1061-1064, 2009.

[10] J. William, R. Nakkeeran, "A New UWB Slot Antenna with Rejection of WiMax and WLAN Bands," *Applied Computational Electromagnetic Society (ACES) Journal*, vol. 25, no. 9, pp. 787-793, September 2010.

[11] M. Naghshvarian-Jahromi, N. Komjani-Barchloui, "Analysis of the Behavior of Sierpinski Carpet Monopole Antenna," *Applied Computational Electromagnetic Society (ACES) Journal,* vol. 24, no. 1, pp. 32-36, February 2009.

[12] Ansoft High Frequency Structure Simulation (HFSS), Ver. 13, Ansoft Corporation, 2010.

Nasser Ojaroudi was born on 1986 in Germi, Iran. He received his B.Sc. degree in Electrical Engineering from Azad University, Ardabil Branch. From 2011, he is working toward the M.Sc. degree in Telecommunication Engineering at Shahid Rajaee Teacher Training University. Since March 2008, he has been a Research Fellow in the Microwave Technology Company (MWT), Tehran, Iran. His research interests include monopole antenna, slot antennas, microstrip antennas for radar systems, ultra-wideband (UWB) and small antennas for wireless communications, microwave passive devices and circuits, and microwave/millimeter systems.

Mohammad Ojaroudi was born on 1984 in Germi, Iran. He received his B.Sc. degree in Electrical Engineering from Azad University, Ardabil Branch and M.Sc. degree in Telecommunication Engineering from Urmia University. From 2010, he is working toward the Ph.D. degree at Shahid Beheshti University. From 2007 until now, he is a Teaching Assistant with the Department of Electrical Engineering, Islamic Azad University, Ardabil Branch, Iran. Since March 2008, he has been a Research Fellow (Chief Executive Officer) in the Microwave Technology Company (MWT), Tehran, Iran. His research interests include analysis and design of microstrip antennas, design and modeling of microwave structures, radar systems, and electromagnetic theory. He is author and coauthor of more than 60 journal and international conference papers.

Shervin Amiri was born in Tehran, Iran, in 1966. He received his B.Sc., M.Sc. and Ph.D. from Iran University of Science & Technology (IUST) in communication systems. Now he is a Scientific Member of Electrical Engineering Department in Iranian Research Organization for Science and Technology (IROST). His research interest fields are Antenna and RF subsystems in Microwave and mm-wave Bands and Radar systems. He is supervisor of many Ph.D. and M.Sc. students in the fields of communication system and subsystems.

Compact CPW-Fed Planar Monopole Antenna with Triple-Band Operation for WLAN/WiMAX Applications

Ping Wang[1,2], Guang-Jun Wen[1], and Yongjun Huang[1]

[1] Centre for RFIC and System Technology
School of Communication and Information Engineering
University of Electronic Science and Technology of China, Chengdu 611731, China
wangpingcqz@163.com, wgj@uestc.edu.cn, yongjunh@uestc.edu.cn

[2] College of Electronic and Information Engineering
Chongqing Three Gorges University, Chongqing 404000, China

Abstract **─** In this paper, we propose a compact coplanar waveguide (CPW) feed planar printed monopole antenna for WLAN/WiMAX applications. By employing two different types of structures-L-shaped slot and I-shaped notched slots, three distinct frequency bands with -10dB reflection coefficient, which correspond to 2.4GHz-2.6GHz, 3.4GHz-3.85GHz and the other at 4.9GHz-5.89GHz, can be achieved to covering 2.4/5.2/5.8 GHz WLAN and 2.5/3.4/5.5 WiMAX. Also, the antenna has a small size of 30mm×23mm, and can provide excellent property, including low profile, moderate gain, approximate omnidirectioal radiation pattern, which prove that the antenna is a good candidate for WLAN/WiMAX applications.

Index Terms **─** Triple-band antenna, L-shaped slot, I-shaped slot, WLAN/WiMAX.

I. INTRODUCTION

Due to the rapid development of modern wireless communication systems technique, the research activity of the multiple or broad bands operation and miniaturized size for current antenna has become one of a highly competitive topic and is growing stupendously. In [1] and [2], the planer monopole antennas can achieve broad bandwidth, but have a large size, especially a large ground plane (250mm×250mm), whose configuration do not meet the miniaturization requirements of radio-frequency (RF) units[3]. However, planar printed microstrip antenna may be a better candidate due to their attractive features, such as ease of fabrication, low profile, small size, ease of integrating with active devices and nearly omnidirectional radiation characteristics, and so on. In order to satisfy the wireless local area network (WLAN) standards of 2.4–2.484 GHz (IEEE 802.11b/g)/5.15–5.825 GHz (IEEE 802.11a) and the worldwide interoperability for microwave access (WiMAX) standards of 2.5–2.69 GHz/3.4–3.69 GHz/5.25–5.85 GHz [4] simultaneously, many microstrip printed antennas have been widely studied [5-9]. In [5], a pair of parasitic strips is introduced to reach an operating bandwidth of 4290 MHz (～108.7%), and the antenna has a dimension of $61\times51.5\text{mm}^2$. A trapezoidal ground [6] and a parasitic U-shaped open stub [7] are also used to the design of the antenna for the WLAN/WiMAX applications. Only by varying the slot's construction, width, and length, the feed point's position and the CPW-fed gap, another compact dual-/multiband antenna have been shown in [8]. A CPW-fed dual-wideband antenna formed by a triangular monopole and a U-shaped monopole is obtained, which occupies a small size and obtain good dipole-like radiation characteristics [9]. However, most of them have large dimensions and do not pay attention on the interference suppression, because there are many other existing narrowband services such as C-band satellite communications that have occupied some licensed frequency bands, which may result in lower performance of interference suppression. To avoid the problem, several novel antennas with three separated resonate frequency are reported in literatures [4, 10-15], which have good impendence bandwidth and radiation pattern, but these antennas have also

Submitted On: Mar. 31, 2012
Accepted On: July 22, 2012

either large size or insufficient frequency restriction.

In this letter, a distinct triple-band resonate antenna for WLAN/WiMAX applications is proposed. By inserting three I-shaped notched slots and an L-shaped slit on radiation patch, along with introducing symmetrical L-shaped couple slot on ground plane which had been proven to be useful to produce resonant mode [16], three separated resonant frequency bands can be easily obtained. Compared to those designs shown in the open literature, the antenna has not only better performance of interference suppression, but also smaller size. Details of the antenna design are described, and prototypes of the proposed antenna have been constructed and tested. The simulated and measured results about impedance bandwidth, radiation pattern, and gain are discussed in detail in the next sections.

II. ANTENNA CONFIGURATION

Geometrical configuration of the proposed antenna for WLAN/WiMAX applications is shown in Fig. 1(a). The antenna is printed on FR-4 substrate of thickness 1mm, with the dielectric constant of 4.4 and a loss tangent of 0.02, and fed by a 50Ω CPW transmission line. In this design, two equal L-shaped ground planes, each comprising two different sections which are $32mm^2$ and $94.15mm^2$, are situated symmetrically on each side of the CPW line. In order to produce resonate at 5.65GHz, a pair of L-shaped slots is etched into ground plane, which broaden the higher frequency range. On the other hand, three I-shaped notched slots are also inserted into radiation patch, which controls the lower operating band (2.4/2.5GHz) and medium frequency band (3.4GHz). Furthermore, a horizontal L-shaped slit of width t and length p+m1 is inserted into radiation patch to improve impendence bandwidth. This arrangement was found to be effective in obtaining an appropriate impedance bandwidth of the antenna, and the performance results are demonstrated in the following section.

In the proposed antenna configuration, the use of two horizontal I-shaped slots and a vertical I-shaped slot on radiation patch produce three different surface current paths, and by properly tuning two different horizontal spacing of s1 and s3 from the patch to the side ground planes, a dual-resonance mode can be excited on lower frequency, a resonate mode produced in medium frequency and other resonate mode happened on higher frequency, respectively. Note that the ground-plane dimensions can also affect the resonant frequencies and operating bandwidths of the two operating bands. Thus, the ground-plane dimensions should also be taken into account in determining the proper parameters for the proposed design to achieve the desired triple-band operation.

Table 1: Parameter values of the fabricated antenna. (Dimensions in mm)

Parameter	*w*	*w1*	*w2*	*w3*	*w4*	*w5*	*L*
Value	30	4	13.7	17	8.95	5.15	23
Parameter	L1	L2	L3	L4	L5	L6	L7
Value	5	3.3	3	3.5	2	2.7	9.7
Parameter	L8	Lf	n	n1	n2	n3	g
Value	8	7	3.7	0.5	3	11.5	0.8
Parameter	g1	wf	s	s1	s2	s3	s4
Value	0.3	2.5	0.3	0.8	0.8	1.3	1.9
Parameter	m	m1	p	t	y		
Value	0.2	0.5	11.5	0.5	0.7		

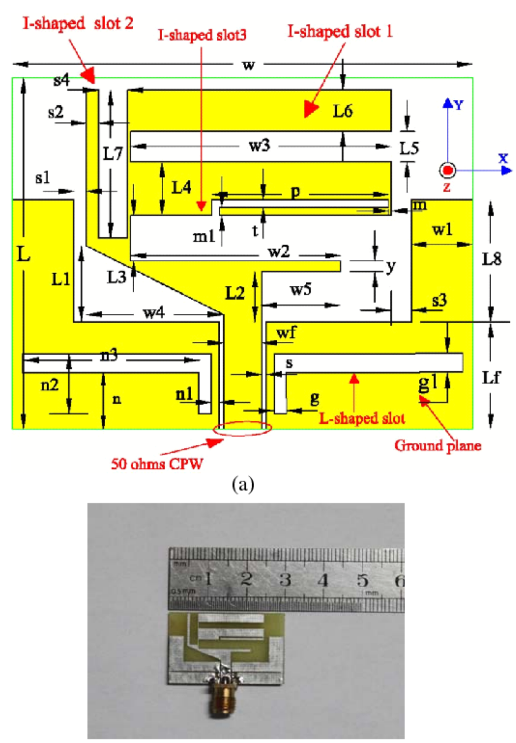

Fig. 1. (a) Geometry of the proposed antenna, (b) Photograph of the proposed antenna.

The proper parameters can be obtained with the aid of the commercially available software Ansoft

HFSS version 13 (high-frequency structure simulator), and a 50Ω-SMA connector is connected to the end of the CPW-feed mechanism serves as antenna port. Parameter values of the proposed antenna are summarized in Table 1. Moreover, a photograph of the fabricated antenna with triple-band characteristic is shown in Fig. 1.

III. EXPERIMENTAL RESULTS AND DISCUSSION

The proposed antenna is implemented and tested using an Agilent N5230A series vector network analyzer. Fig. 2 describes the simulated and experimental reflection coefficient against the frequency, which shows good agreement. The simulated and the experimental below 10-dB bandwidths range from 2.4–2.62 GHz/2.4–2.6 GHz(8.76%/8%), from3.37-3.74GHz/3.4-3.85GHz (10.4%/12.4%)and from 5.04–5.75GHz/4.9–5.89GHz (13.2%/18.4％), which shows a minor frequency shift owing to the error of substrate parameters of the FR-4 substrate and tolerance in manufacturing. It is also observed that best resonant frequencies happened in 2.46GHz, 2.56GHz, 3.56GHz, 5.25GHz and 5.65GHz. The Smith chart and the simulated input impedance of the proposed antenna shown in Fig. 3 and Fig. 4 further illustrate the excellent impedance matching of the proposed triple-band antenna, respectively.

To further insight into the physical behavior of the antenna, the simulated current distributions of the proposed antenna at different resonate frequencies are presented in Fig. 5. We can see that

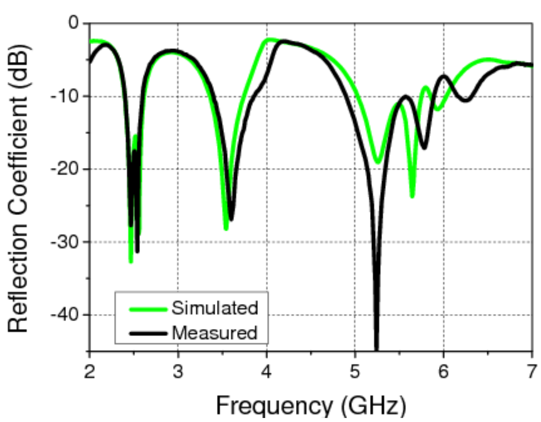

Fig. 2. Simulated and measured reflection coefficient of the proposed antenna.

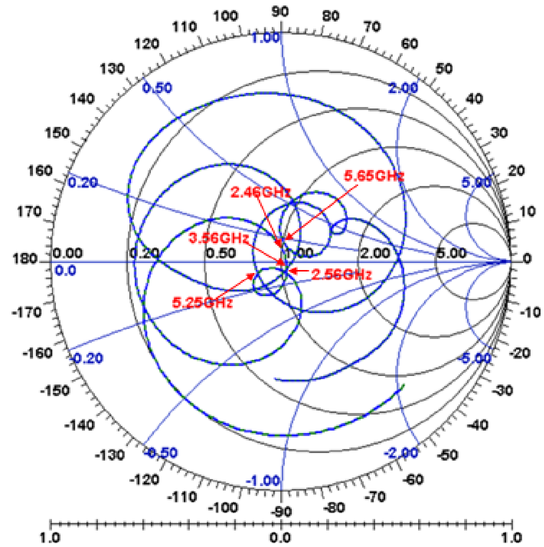

Fig. 3. Simulated input impedance on Smith chart for the proposed antenna.

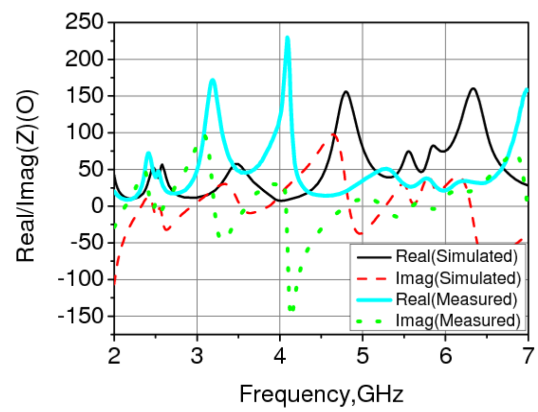

Fig. 4. Simulated and measured impedance of the antenna.

notched slot 1 provide a low resonate frequency (2.56GHz) shown in Fig. 5 (b), moreover, notched slot 2 and CPW control the flow direction of current in 2.46GHz and 3.56GHz. Meanwhile, in the high frequency (5.25GHz) the unfolded arm provide a resonate mode, and a pair of loaded L-shaped slots with length of about $\lambda/2$ provide the another resonate mode(5.65GHz), which broaden the higher frequency bandwidth.

Figure 6 presents the frequency response of reflection coefficient for the proposed antenna without different slots embedment. In the case without notched slot 1, second resonate mode is not effectively excited at lower resonance frequency range, and other frequency ranges have no effects. Similarly, when removing a pair of L-shaped slots on the ground plane, a worse frequency response was achieved in higher frequency range, but in other two frequency bands it was invariable. It is also observed that existence of the notched slot 2 not only can largely affect impedance matching to the lower band and the medium band, but also seriously change the excitation of the upper-band resonant modes. It clearly indicates that these results are similar with that achieved from simulated current distributions in Fig. 5.

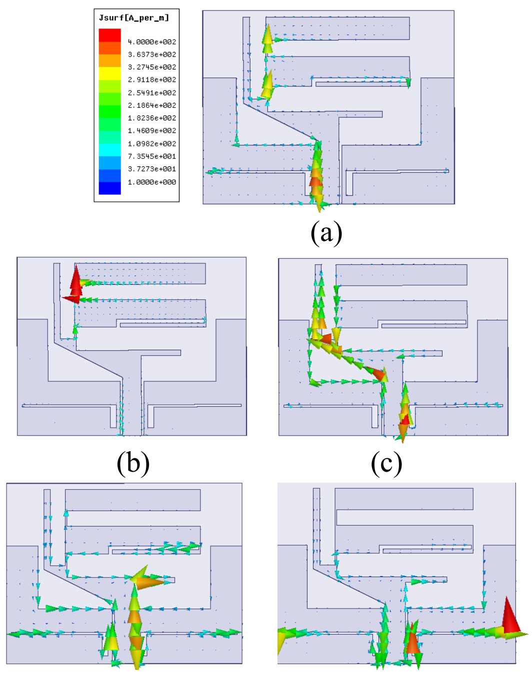

(a) (b) (c) (d) (e)

Fig. 5. Simulation surface current in (a) 2.46GHz, (b) 2.56GHz, (c) 3.56GHz, (d) 5.25GHz, (e) 5.65GHz.

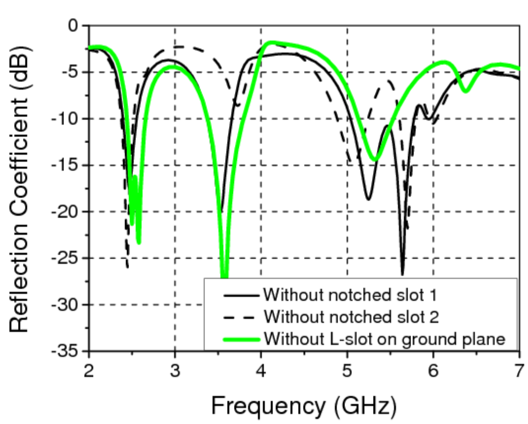

Fig. 6. The effect of notched slots to the proposed antenna's resonant modes.

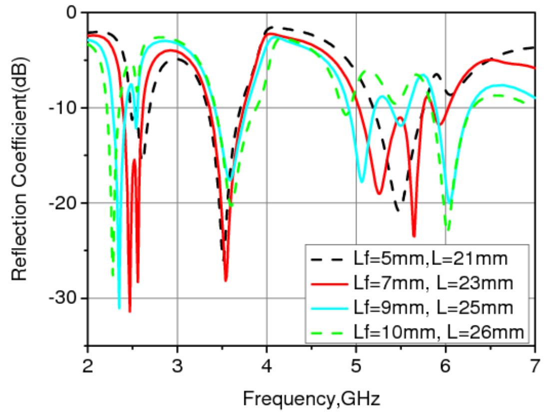

(a)

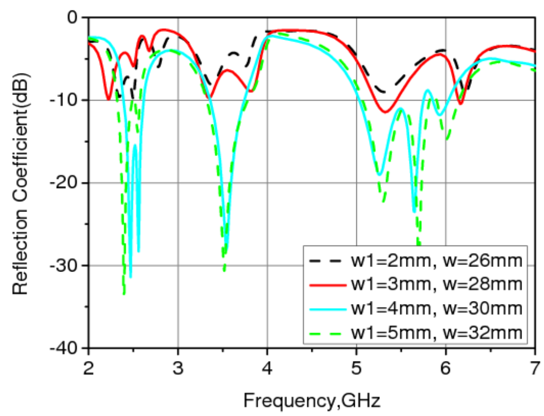

(b)

Fig. 7. The effect of the ground plane size on the antenna performance.

The simulated reflection coefficient curves with different ground plane widths (w) and lengths (Lf) are exhibited in Fig. 7. It is clearly seen that when w and Lf are changed, they can significantly increase or decrease the impedance bandwidth of the antenna. It is also noticed that the length of the ground plane affects the impedance matching more significantly at lower frequencies than at higher frequencies as shown in Fig. 7(a), and in Fig. 7(b) the reflection coefficient curves vary significantly and exhibit various shapes for the four different ground plane widths. To have a wider impedance bandwidth, the length and width of ground plane need to be well optimized and the extracted optimum parameter values are w=30mm and Lf=7mm.

Radiation characteristics are also considered. The simulated and measured radiation patterns of the proposed antenna in xz-plane and yz-plane for both E_Φ and E_θ at 2.46GHz, 3.56GHz and

5.25GHz (resonate frequencies) are shown in Fig. 8, respectively. From the results, the radiation patterns in the xz- and yz-planes, as expected, are all very dipole-like radiation. The electric field E_θ keeps always eight-shaped radiation pattern and the electric field E_Φ holds nearly omnidirectional radiation pattern in xz-plane and yz-plane. It is also observed that the antenna has more vertical current (y-axis) shown in Fig. 5 (d) at higher frequency, so the radiation pattern is similar with dipole-like radiation along y-axis. Fig. 9 shows the peak gains and radiation efficiency across the three operating frequency bands. It should be observed that for the operating band of 2.4–2.7 GHz, the peak gain of the antenna varies from 1dB to 2.05dB, and the radiation efficiency obtains the lowest value of 70% in centre frequency. For the medium band, the antenna has relatively small gain and radiation efficiency variation, the peak gain is 2.14dB, and the radiation efficiency varies around 83%.

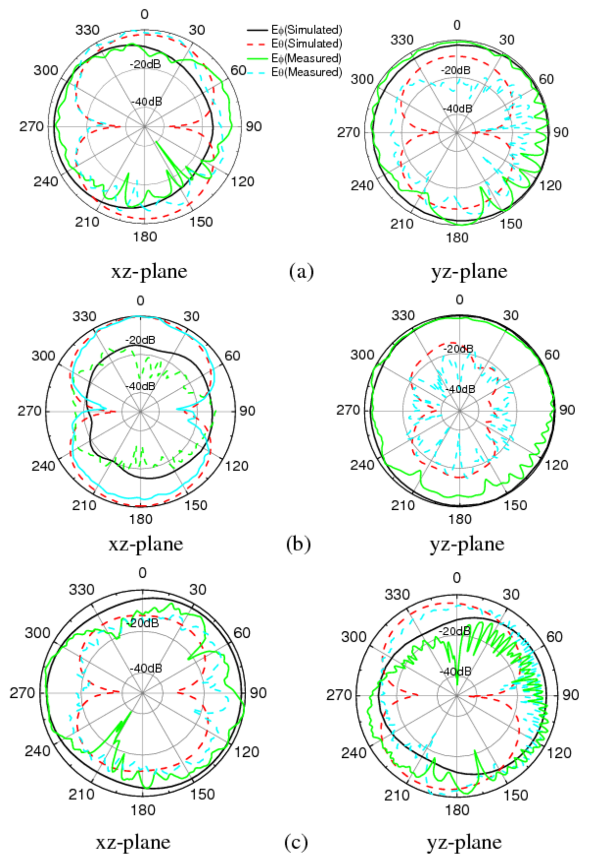

Fig. 8. Simulated and measured radiation patterns for the proposed antenna at (a) 2.46GHz, (b) 3.56GHz and (c) 5.25GHz in xz-plane and yz-plane, respectively.

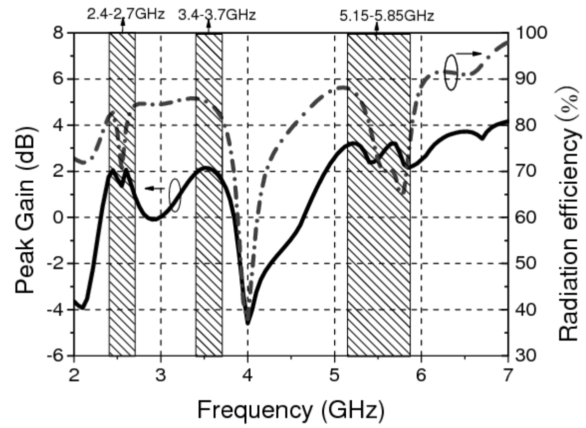

Fig. 9. Peak gain and radiation efficiency of the proposed antenna.

The peak gain in the higher operating band of 5.15–5.85 GHz is also stable, which varies from 2.15dB to 3.2dB, however, the radiation efficiency drop to 65% in 5.75GHz. The low radiation efficiency may be high loss in FR-4 substrate (a loss tangent of 0.02), which results in a decrease in gain and radiation efficiency as shown in Fig. 9. But then the gain of the proposed antenna within the operating bands satisfies the requirement of some wireless communication terminals.

IV. CONCLUSION

In this paper, a novel CPW-fed monopole antenna is proposed for WLAN/WiMAX applications. The proposed antenna has good performance of interference suppression, excellent radiation patterns, excellent resonance character and small size. The measured results illustrate that the obtained impedance bandwidths are about 8％ (2.4GHz-2.6GHz), 12.4％ (3.4GHz-3.85GHz) and 18.4 ％ (4.9GHz-5.89GHz), good enough for WLAN and WiMAX applications. This indicates that the proposed antenna is well suited for WLAN/WiMAX portable units and mobile handsets.

ACKNOWLEDGMENT

This work is supported by Research Fund for the Doctoral Program of Higher Education of China (No.20110185110014).

REFERENCES

[1] J. Anguera, J. P. Daniel, C. Borja, J. Mumbrú, C. Puente, T. Leduc, K. Sayegrih, and P. Van Roy, “Metallized Foams for Antenna Design:

Application to Fractal-Shaped Sierpinski-Carpet Monopole", *Progress In Electromagnetics Research, PIER,* vol. 104, pp. 239-251, 2010.
[2] M. J. Ammann and Z. N. Chen, "Wideband Monopole Antennas for Multi-Band Wireless Systems", *IEEE Antennas and Propagation Magazine*, vol. 45, no. 2, pp. 146-150, April 2003.
[3] K. L.Wong, Compact and broadband Microstrip Antennas. New York: Wiley, 2002.
[4] P. Jing, A.-G. Wang, S. Gao and L. Wen, "Miniaturized triple-band antenna with a defected ground plane for WLAN/WiMAX applications," *IEEE Antenna Wireless Propag. Lett.*, vol. 10, pp. 298-301, 2011.
[5] J.-Y. Jan and L.-C. Wang, "Printed wideband rhombus slot antenna with a pair of parasitic strips for multiband applications," *IEEE Trans. Antennas Propag.,* vol. 57, no. 4, pp. 1267-1270, 2009.
[6] C.-Y. Pan, T.-S. Horng, W.-S. Chen and C.-H. Huang, "Dual wideband printed monopole antenna for WLAN/WiMAX applications," *IEEE Antenna Wireless Propag. Lett.*, vol. 6, pp. 149-151, 2007.
[7] J. N. Lee, J.H. Kim, J. K. Park and J. S. Kim, "Design of dual-band antenna with U-shaped open stub for WLAN/UWB applications," *Micow.Opt. Technol. Lett.*, vol. 51, no. 2, pp. 284-289, 2009.
[8] C. Yoon, W.-J. Lee, S.-P. Kang, "A planar CPW-fed slot antenna on thin substrate for dual-band operation of WLAN applications," *Micow. Opt. Technol. Lett.,* vol. 51, no. 12, pp. 2799-2802, 2009.
[9] Q.-X. Chun and L.-H. Ye, "Design of compact dual-wideband antenna with assembled monopoles," *IEEE Trans. Antennas Propag.,* vol. 58, no. 12, pp. 4063-4066, 2010.
[10] H.-W. Liu, C.-H. Ku and C-F. Yang, "Novel CPW-Fed Planar Monopole antenna for WiMAX/WLAN applications," *IEEE Antenna Wireless Propag. Lett.*, vol. 9, pp. 240-243, 2010.
[11] S. Chaimool and K. L. Chung, "CPW-fed mirrored-L monopole antenna with distinct triple bands for WiFi and WiMAX applications," *Electron. Lett.,* vol. 45, no. 18, pp. 928-929, 2009.
[12] W.-S. Chen and K.-Y. Ku, "Band-rejected design of the printed open slot antenna for WLAN/WiMAX operation," *IEEE Trans. Antennas Propag.*, vol. 56, no. 4, pp. 1163-1169, 2008.
[13] L. Dang, Z. Y. Lei, Y. J. Xie, G. L. Ning and J. Fan, "A compact microstrip slot triple-band antenna for WLAN/WiMAX applications," *IEEE Antenna Wireless Propag. Lett.*, vol. 9, pp. 1178-1181, 2010.
[14] W. Hu, Y.-Z. Yin, P. Fei and X. Yang, "Compact tri-band square slot antenna with symmetrical L-strips for WLAN/WiMAX applications," *IEEE Antenna Wireless Propag. Lett.*, vol. 10, pp. 462-465, 2011.
[15] G. Zhang, J. S. Hong, B. Z. Wang, G. Song, "Switched Band-Notched UWB/ WLAN Monopole Antenna," *Applied Computational Electromagnetics Society (ACES) Journal*, vol. 27, no. 3, pp. 256-260, March 2012.
[16] S. S. Garcia and J.-J. Laurin, "Study of a CPW Inductively Coupled Slot Antenna," *IEEE Trans Antennas Propag.,* vol. 47, pp. 58-64, 1999.

Ping Wang was born in Chongqing, China, in 1981. He received his B.S. in physics from Western Chongqing University of China in 2005 and the M.S degree in theoretical physics from Chongqing University, Chongqing, in 2008. Currently, he is working toward the Ph.D. degree in University of Electronic Science and Technology of China (UESTC). His current research interests include patch antennas, wideband antennas, and arrays.

Guangjun Wen was born in Sichuan, China, in 1964. He received his M.S. and Ph.D from Chongqing University of China in 1995 and from University of Electronic Science and Technology of China in 1998, respectively. He is currently a professor and doctor supervisor at University of Electronic Science and Technology of China. His research and industrial experience covers a broad spectrum of electromagnetics, including RF, Microwave, Millimeter wave Integrated Circuits and Systems design for Wireless Communication, Navigation, Identification, Mobile TV applications, RFIC/MMIC/MMMIC device modeling, System on Chip (SoC) and System in Package (SiC) Design, RF/Microwave/Millimeter wave Power source Design, "The Internet of things" devices and system, RFID system and networks, antennas, as well as, model of electromagnetic metamaterial and its application in microwave engineering area.

Yongjun Huang was born in Sichuan, China, in 1985. He received his B.S. in Mathematics from NeiJiang Normal University of China in 2007 and M. S. in Communication Engineering from University of Electronic Science and Technology of China in 2010. His dissertation work and research activities are electromagnetic metamaterial and its application in microwave engineering area, FDTD analysis for the model and RCS characteristic of metamaterials.

2012 INSTITUTIONAL MEMBERS

DTIC-OCP LIBRARY
8725 John J. Kingman Rd, Ste 0944
Fort Belvoir, VA 22060-6218

AUSTRALIAN DEFENCE LIBRARY
Northcott Drive
Canberra, A.C.T. 2600 Australia

BEIJING BOOK CO, INC
701 E Linden Avenue
Linden, NJ 07036-2495

DARTMOUTH COLLEGE
6025 Baker/Berry Library
Hanover, NH 03755-3560

DSTO EDINBURGH
AU/33851-AP, PO Box 830470
Birmingham, AL 35283

SIMEON J. EARL – BAE SYSTEMS
W432A, Warton Aerodome
Preston, Lancs., UK PR4 1AX

ENGINEERING INFORMATION, INC
PO Box 543
Amsterdam, Netherlands 1000 Am

ETSE TELECOMUNICACION
Biblioteca, Campus Lagoas
Vigo, 36200 Spain

GA INSTITUTE OF TECHNOLOGY
EBS-Lib Mail code 0900
74 Cherry Street
Atlanta, GA 30332

TIMOTHY HOLZHEIMER
Raytheon
PO Box 1044
Rockwall, TX 75087

HRL LABS, RESEARCH LIBRARY
3011 Malibu Canyon
Malibu, CA 90265

IEE INSPEC
Michael Faraday House
6 Hills Way
Stevenage, Herts UK SG1 2AY

INSTITUTE FOR SCIENTIFIC INFO.
Publication Processing Dept.
3501 Market St.
Philadelphia, PA 19104-3302

LIBRARY – DRDC OTTAWA
3701 Carling Avenue
Ottawa, Ontario, Canada K1A OZ4

LIBRARY of CONGRESS
Reg. Of Copyrights
Attn: 407 Deposits
Washington DC, 20559

LINDA HALL LIBRARY
5109 Cherry Street
Kansas City, MO 64110-2498

MISSOURI S&T
400 W 14th Street
Rolla, MO 56409

MIT LINCOLN LABORATORY
Periodicals Library
244 Wood Street
Lexington, MA 02420

NATIONAL CHI NAN UNIVERSITY
Lily Journal & Book Co, Ltd
20920 Glenbrook Drive
Walnut, CA 91789-3809

JOHN NORGARD
UCCS
20340 Pine Shadow Drive
Colorado Springs, CO 80908

OSAMA MOHAMMED
Florida International University
10555 W Flagler Street
Miami, FL 33174

NAVAL POSTGRADUATE SCHOOL
Attn:J. Rozdal/411 Dyer Rd./ Rm 111
Monterey, CA 93943-5101

NDL KAGAKU
C/0 KWE-ACCESS
PO Box 300613 (JFK A/P)
Jamaica, NY 11430-0613

OVIEDO LIBRARY
PO BOX 830679
Birmingham, AL 35283

DAVID PAULSEN
E3Compliance
1523 North Joe Wilson Road
Cedr Hill, TX 75104-1437

PENN STATE UNIVERSITY
126 Paterno Library
University Park, PA 16802-1808

DAVID J. PINION
1122 E Pike Street #1217
SEATTLE, WA 98122

KATHERINE SIAKAVARA
Gymnasiou 8
Thessaloniki, Greece 55236

SWETS INFORMATION SERVICES
160 Ninth Avenue, Suite A
Runnemede, NJ 08078

YUTAKA TANGE
Maizuru Natl College of Technology
234 Shiroya
Maizuru, Kyoto, Japan 625-8511

TIB & UNIV. BIB. HANNOVER
DE/5100/G1/0001
Welfengarten 1B
Hannover, Germany 30167

UEKAE
PO Box 830470
Birmingham, AL 35283

UNIV OF CENTRAL FLORIDA
4000 Central Florida Boulevard
Orlando, FL 32816-8005

UNIVERSITY OF COLORADO
1720 Pleasant Street, 184 UCB
Boulder, CO 80309-0184

UNIVERSITY OF KANSAS – WATSON
1425 Jayhawk Blvd 210S
Lawrence, KS 66045-7594

UNIVERSITY OF MISSISSIPPI
JD Williams Library
University, MS 38677-1848

UNIVERSITY LIBRARY/HKUST
Clear Water Bay Road
Kowloon, Honk Kong

CHUAN CHENG WANG
8F, No. 31, Lane 546
MingCheng 2nd Road, Zuoying Dist
Kaoshiung City, Taiwan 813

THOMAS WEILAND
TU Darmstadt
Schlossgartenstrasse 8
Darmstadt, Hessen, Germany 64289

STEVEN WEISS
US Army Research Lab
2800 Powder Mill Road
Adelphi, MD 20783

YOSHIHIDE YAMADA
NATIONAL DEFENSE ACADEMY
1-10-20 Hashirimizu
Yokosuka, Kanagawa,
Japan 239-8686

APPLIED COMPUTATIONAL ELECTROMAGNETICS SOCIETY JOURNAL
http://aces.ee.olemiss.edu

INFORMATION FOR AUTHORS

PUBLICATION CRITERIA

Each paper is required to manifest some relation to applied computational electromagnetics. **Papers may address general issues in applied computational electromagnetics, or they may focus on specific applications, techniques, codes, or computational issues.** While the following list is not exhaustive, each paper will generally relate to at least one of these areas:

1. **Code validation.** This is done using internal checks or experimental, analytical or other computational data. Measured data of potential utility to code validation efforts will also be considered for publication.

2. **Code performance analysis.** This usually involves identification of numerical accuracy or other limitations, solution convergence, numerical and physical modeling error, and parameter tradeoffs. However, it is also permissible to address issues such as ease-of-use, set-up time, run time, special outputs, or other special features.

3. **Computational studies of basic physics.** This involves using a code, algorithm, or computational technique to simulate reality in such a way that better, or new physical insight or understanding, is achieved.

4. **New computational techniques** or new applications for existing computational techniques or codes.

5. **"Tricks of the trade"** in selecting and applying codes and techniques.

6. **New codes, algorithms, code enhancement, and code fixes.** This category is self-explanatory, but includes significant changes to existing codes, such as applicability extensions, algorithm optimization, problem correction, limitation removal, or other performance improvement. **Note: Code (or algorithm) capability descriptions are not acceptable, unless they contain sufficient technical material to justify consideration.**

7. **Code input/output issues.** This normally involves innovations in input (such as input geometry standardization, automatic mesh generation, or computer-aided design) or in output (whether it be tabular, graphical, statistical, Fourier-transformed, or otherwise signal-processed). Material dealing with input/output database management, output interpretation, or other input/output issues will also be considered for publication.

8. **Computer hardware issues.** This is the category for analysis of hardware capabilities and limitations of various types of electromagnetics computational requirements. Vector and parallel computational techniques and implementation are of particular interest.

Applications of interest include, but are not limited to, antennas (and their electromagnetic environments), networks, static fields, radar cross section, inverse scattering, shielding, radiation hazards, biological effects, biomedical applications, electromagnetic pulse (EMP), electromagnetic interference (EMI), electromagnetic compatibility (EMC), power transmission, charge transport, dielectric, magnetic and nonlinear materials, microwave components, MEMS, RFID, and MMIC technologies, remote sensing and geometrical and physical optics, radar and communications systems, sensors, fiber optics, plasmas, particle accelerators, generators and motors, electromagnetic wave propagation, non-destructive evaluation, eddy currents, and inverse scattering.

Techniques of interest include but not limited to frequency-domain and time-domain techniques, integral equation and differential equation techniques, diffraction theories, physical and geometrical optics, method of moments, finite differences and finite element techniques, transmission line method, modal expansions, perturbation methods, and hybrid methods.

Where possible and appropriate, authors are required to provide statements of quantitative accuracy for measured and/or computed data. This issue is discussed in "Accuracy & Publication: Requiring, quantitative accuracy statements to accompany data," by E. K. Miller, *ACES Newsletter,* Vol. 9, No. 3, pp. 23-29, 1994, ISBN 1056-9170.

SUBMITTAL PROCEDURE

All submissions should be uploaded to ACES server through ACES web site (http://aces.ee.olemiss.edu) by using the upload button, journal section. Only pdf files are accepted for submission. The file size should not be larger than 5MB, otherwise permission from the Editor-in-Chief should be obtained first. Automated acknowledgment of the electronic submission, after the upload process is successfully completed, will be sent to the corresponding author only. It is the responsibility of the corresponding author to keep the remaining authors, if applicable, informed. Email submission is not accepted and will not be processed.

EDITORIAL REVIEW

In order to ensure an appropriate level of quality control, papers are peer reviewed. They are reviewed both for technical correctness and for adherence to the listed guidelines regarding information content and format.

PAPER FORMAT

Only camera-ready electronic files are accepted for publication. The term **"camera-ready" means that the material is neat, legible, reproducible, and in accordance with the final version format listed below.**

The following requirements are in effect for the final version of an ACES Journal paper:

1. The paper title should not be placed on a separate page.

The title, author(s), abstract, and (space permitting) beginning of the paper itself should all be on the first page. The title, author(s), and author affiliations should be centered (center-justified) on the first page. The title should be of font size 16 and bolded, the author names should be of font size 12 and bolded, and the author affiliation should be of font size 12 (regular font, neither italic nor bolded).

2. An abstract is required. The abstract should be a brief summary of the work described in the paper. It should state the computer codes, computational techniques, and applications discussed in the paper (as applicable) and should otherwise be usable by technical abstracting and indexing services. The word "Abstract" has to be placed at the left margin of the paper, and should be bolded and italic. It also should be followed by a hyphen (—) with the main text of the abstract starting on the same line.

3. All section titles have to be centered and all the title letters should be written in caps. The section titles need to be numbered using roman numbering (I. II. ….)

4. Either British English or American English spellings may be used, provided that each word is spelled consistently throughout the paper.

5. Internal consistency of references format should be maintained. As a guideline for authors, we recommend that references be given using numerical numbering in the body of the paper (with numerical listing of all references at the end of the paper). The first letter of the authors' first name should be listed followed by a period, which in turn, followed by the authors' complete last name. Use a coma (,) to separate between the authors' names. Titles of papers or articles should be in quotation marks (" "), followed by the title of journal, which should be in italic font. The journal volume (vol.), issue number (no.), page numbering (pp.), month and year of publication should come after the journal title in the sequence listed here.

6. Internal consistency shall also be maintained for other elements of style, such as equation numbering. Equation numbers should be placed in parentheses at the right column margin. All symbols in any equation have to be defined before the equation appears or right immediately following the equation.

7. The use of SI units is strongly encouraged. English units may be used as secondary units (in parentheses).

8. Figures and tables should be formatted appropriately (centered within the column, side-by-side, etc.) on the page such that the presented data appears close to and after it is being referenced in the text. When including figures and tables, all care should be taken so that they will appear appropriately when printed in black and white. For better visibility of paper on computer screen, it is good to make color figures with different line styles for figures with multiple curves. Colors should also be tested to insure their ability to be distinguished after black and white printing. Avoid the use of large symbols with curves in a figure. It is always better to use different line styles such as solid, dotted, dashed, etc.

9. A figure caption should be located directly beneath the corresponding figure, and should be fully justified.

10. The intent and meaning of all text must be clear. For authors who are not masters of the English language, the ACES Editorial Staff will provide assistance with grammar (subject to clarity of intent and meaning). However, this may delay the scheduled publication date.

11. Unused space should be minimized. Sections and subsections should not normally begin on a new page.

ACES reserves the right to edit any uploaded material, however, this is not generally done. It is the author(s) responsibility to provide acceptable camera-ready files in pdf and MSWord formats. Incompatible or incomplete files will not be processed for publication, and authors will be requested to re-upload a revised acceptable version.

COPYRIGHTS AND RELEASES

Each primary author must execute the online copyright form and obtain a release from his/her organization vesting the copyright with ACES. Both the author(s) and affiliated organization(s) are allowed to use the copyrighted material freely for their own private purposes.

Permission is granted to quote short passages and reproduce figures and tables from and ACES Journal issue provided the source is cited. Copies of ACES Journal articles may be made in accordance with usage permitted by Sections 107 or 108 of the U.S. Copyright Law. This consent does not extend to other kinds of copying, such as for general distribution, for advertising or promotional purposes, for creating new collective works, or for resale. The reproduction of multiple copies and the use of articles or extracts for commercial purposes require the consent of the author and specific permission from ACES. Institutional members are allowed to copy any ACES Journal issue for their internal distribution only.

PUBLICATION CHARGES

All authors are allowed for 8 printed pages per paper without charge. Mandatory page charges of $75 a page apply to all pages in excess of 8 printed pages. Authors are entitled to one, free of charge, copy of the printed journal issue in which their paper was published. Additional reprints are available for $ 50. Requests for additional re-prints should be submitted to the managing editor or ACES Secretary.

Corresponding author is required to complete the online form for the over page charge payment right after the initial acceptance of the paper is conveyed to the corresponding author by email.

ACES Journal is abstracted in INSPEC, in Engineering Index, DTIC, Science Citation Index Expanded, the Research Alert, and to Current Contents/Engineering, Computing & Technology.